THE STRUCTURE OF ^{23}AL AND ASTROPHYSICAL CONSEQUENCES

A Dissertation

by

YONGJUN ZHAI

Submitted to the Office of Graduate Studies of
Texas A&M University
in partial fulfillment of the requirements for the degree of

DOCTOR OF PHILOSOPHY

December 2007

Major Subject: Physics

THE STRUCTURE OF ^{23}AL AND ASTROPHYSICAL CONSEQUENCES

A Dissertation

by

YONGJUN ZHAI

Submitted to the Office of Graduate Studies of
Texas A&M University
in partial fulfillment of the requirements for the degree of

DOCTOR OF PHILOSOPHY

Approved by:

Chair of Committee,	Robert E. Tribble
Committee Members,	John C. Hardy
	Carl A. Gagliardi
	Sherry J. Yennello
Head of Department,	Edward S. Fry

December 2007

Major Subject: Physics

ABSTRACT

The Structure of ^{23}Al and Astrophysical Consequences.

(December 2007)

Yongjun Zhai, B.S., Peking University;

M.S., Peking University;

M.S., Louisiana State University

Chair of Advisory Committee: Dr. Robert E. Tribble

Motivated by existing nuclear astrophysics problems, the β-decay of the proton rich nucleus ^{23}Al was studied for the first time with pure samples which were obtained by using the ^{1}H(^{24}Mg,^{23}Al)2n reaction and the MARS recoil separator at Texas A&M University. β and β-γ coincidence measurements were made with a fast tape-transport system, scintillator, BGO and HPGe γ detectors. The experiment allowed us to measure absolute β branching ratios and to determine logft values for transitions to final states in ^{23}Mg, including the isobaric analog state (IAS), and, therefore, to determine unambiguously the spin and parity of the ^{23}Al ground state to be $J^{\pi} = 5/2^{+}$. This work excludes the large increases in the radiative proton capture cross section for the reaction ^{22}Mg$(p,\gamma)^{23}$Al at astrophysical energies, which were implied by claims that the spin and parity of the ^{23}Al ground state were $J^{\pi} = 1/2^{+}$. More precise half life and mass determinations of ^{23}Al were obtained from the experimental data. The logft for the Fermi transition to its isobaric analog state in ^{23}Mg was also determined for the first time. This IAS and a state 16 keV below it were observed, well separated in the same experiment for the first time. The β-decay scheme of the proton rich nucleus ^{23}Al was established. We can now solve a number of inconsistencies in the literature, exclude strong isospin mixing claimed before, and

obtain a new determination of the resonance strength. The IAS and the state 16 keV below it are resonances in the $^{22}\mathrm{Na}(p,\gamma)^{23}$ Mg reaction at energies that are important in novae. This second state turns out to be the resonance that gives the most important contribution in the depletion of ^{22}Na from novae. Both of the reactions of $^{22}\mathrm{Mg}(p,\gamma)^{23}\mathrm{Al}$ and $^{22}\mathrm{Na}(p,\gamma)^{23}\mathrm{Mg}$ have been suggested as possible candidates for diverting some of the flux in oxygen-neon novae explosions from the A=22 into the A=23 mass chain.

To **my wife, my parents and my two brothers**

ACKNOWLEDGMENTS

First and foremost, I would like to express my sincere gratitude to Dr. Robert E. Tribble and Dr. Livius Trache. As wise and gracious supervisors, they have provided me with knowledge of their deep understanding of nuclear physics, invaluable encouragement, and great help in last five years. Their creative way of thinking and solving challenging problems has inspired me through this long journey. They encouraged me to attend conferences, workshops, summer schools and collaborated experiments (France) to communicate with many great physicists around the world and build the network that could open the door to improve my career in the future. I also appreciate their time in reviewing the dissertation to improve the clarity. It is my pleasure to work under their guidance.

My thanks go to Dr. Victor E. Iacob for his advice and help. My gratitude goes to Distinguished Prof. John C. Hardy, Dr. Carl A. Gagliardi and Dr. Sherry J. Yennello for their advice as dissertation committee members and their input to this work.

I appreciate the help in preparation of the dissertation experiments and sharing with me the long and difficult beam-time shifts given by my collaborators who are Dr. Ninel Nica, Dr. Gabriel Tabacaru, Dr. Changbo Fu, Dr. Tariq Al-Abdullah, Dr. Victor V. Golovko, Dr. Adriana Banu, Matthew McCleskey, Ellen Simmons and Hyo-In Park.

I want to express my special thanks to Distinguished Prof. Joseph B. Natowitz and Prof. Xiting Lu for their advice and encouragement. My gratitude goes to Dr. Gabriel Tabacaru, Dr. Ninel Nica and Dr. Vladilen Goldberg for their advice and help, and also to Dr. Y. -W. Lui and Dr. Robert Burch for their support on

computer hardware and software.

I deeply and greatly appreciate my parents and two brothers for their continuous and unconditional support, endless love and invaluable encouragement during my school years as well as the rest of my life.

A special note of appreciation goes to my friends for their encouragement and friendship. They are Dr. Qian Wang, Ling Zhou, Dr. Xiaodong Tang, Kejiao Ding, Dr. Changbo Fu, Xinfeng Chen, Dr. Wei Liu, Lijun Qin, Dr. Yong Peng, Dr. Wanpeng Tan, Dr. Hui Hua, Shi Yan, Dr. Tao Zheng, Dr. Baonian Guo, Jia Ke, Jianjun Wang, Dr. Jian Zuo, Fei Zheng, Dr. Lin Shao, Dr. Yufei Xiao, Dr. Zhiqiang Chen, Yun Li and Mitaire Ojaruega.

I also want to acknowledge the hard and competent work of the technical staff of the K500 superconducting cyclotron at the Cyclotron Institute of Texas A&M University. My special thanks go to Dr. George Kim and Dr. Don May for providing high quality beams.

This work was supported by the U.S. Department of Energy under Grant No. DE-FG03-93ER40773 and by the Robert A. Welch Foundation under Grant No.A-1397.

TABLE OF CONTENTS

CHAPTER Page

LIST OF TABLES

LIST OF FIGURES

FIGURE Page

FIGURE Page

FIGURE Page

FIGURE Page

CHAPTER I

INTRODUCTION

Looking up at the night sky, stars and galaxies are shining and amazing. Driven by curiosity, people have been exploring the mysteries of the birth, growth and death of stars for a long time. Nuclear Astrophysics, an interdisciplinary subject, has developed as a consequence of us trying to understand the origin of the universe and its destination. It focuses on questions at the interface between nuclear physics and astrophysics, such as stellar evolution and stellar explosions. With the advances in experimental nuclear astrophysics, physicists can now investigate many stellar processes in the laboratory.

A. Research Background

Today there is growing interest in understanding nucleosynthesis in novae, especially the synthesis of γ-ray emitters, because of the ability to detect γ rays from astrophysical sources with space-based telescopes. Scientists detected γ rays from the decay of long-lived isotopes like ^{26}Al ($t_{1/2}$=7.2x10^5 years), ^{44}Ti ($t_{1/2}$=60.0 years) and ^{56}Ni($t_{1/2}$=6.1 days). Among the expected γ-rays, however, the 1.275 MeV γ-ray from ^{22}Na ($t_{1/2}$ = 2.602 years) has not been detected. ^{22}Na is thought to be produced in the thermonuclear runaway and in the high-temperature phase of so-called ONe novae (oxygen-neon novae) through the reaction chain named the Neon Sodium (NeNa) cycle [1, 2, 3, 4]. There is only an upper limit set on ^{22}Na production, which is below the theoretical predictions [5, 6]. The NeNa cycle reaction chain was initially proposed as following:

The journal model is Physical Review C.

^{20}Ne$(p,\gamma)^{21}$Na$(\beta^+,\nu)^{21}$Ne$(p,\gamma)^{22}$Na$(\beta^+,\nu)^{22}$Ne$(p,\gamma)^{23}$Na$(p,\alpha)^{20}$Ne.

However, this reaction chain can not be considered a cycle since the ^{22}Na$(\beta^+,\nu)^{22}$Ne decay is very slow ($t_{1/2} = 2.602$ years) while a nova explosion usually lasts around 200 seconds [2]. Thus the proton capture reaction has to wait for the β^+–decay before the reaction chain can continue. A new reaction cycle was proposed to overcome this difficulty that is shown below:

^{20}Ne$(p,\gamma)^{21}$Na$(\beta^+,\nu)^{21}$Ne$(p,\gamma)^{22}$Na$(p,\gamma)^{23}$Mg$(\beta^+,\nu)^{23}$Na$(p,\alpha)^{20}$Ne.

The lack of observing ^{22}Na from its γ-ray raised some questions. Poor knowledge of the reaction cross sections employed in the network calculations for the rp-process may cause this discrepancy. Some proposed that ^{22}Na itself or its precursor ^{22}Mg could be depleted by the radiative proton capture reactions ^{22}Na(p,γ)^{23}Mg [7, 8] and ^{22}Mg(p,γ)^{23}Al [9]. Both of these reactions could lead to a serious reduction of the residual ^{22}Na abundance with ^{22}Na$(p,\gamma)^{23}$Mg possibly a major contributor to this depletion. Depletion of ^{22}Mg may happen in the explosive phase of novae which is so fast and short that equilibrium with photodissociation is not reached. The ^{22}Mg(p,γ)^{23}Al reaction is dominated by direct proton capture to the ground state and by resonant capture through the first excited state in ^{23}Al. Until now, no one has measured the cross section directly at stellar energies. ^{22}Mg is too short-lived ($t_{1/2}$=3.86 seconds) to make it a target, and, besides, it is hard to get an intense ^{22}Mg beam for measurements in inverse kinematics. Based on systematic studies, one can assume that the spins and parities in the ^{23}Al ground state are the same as in its mirror nucleus ^{23}Ne, i.e. $5/2^+$. Combining this assumption with the resonance energy determined experimentally, the reaction rate for ^{22}Mg(p,γ)^{23}Al was estimated [10]. This spin and parity assignment, however, was challenged recently, as will be explained in the next subsection. This lead us to the dedicated measurement to determine the J^π for the ^{23}Al ground state.

Samples of pure ^{23}Al radioactive nuclei had not been separated prior to this work. β delayed proton decay branches were reported in three papers [11, 12, 13] where the ground state spin of ^{23}Al could not be determined directly. Gough et. al [11] could determine the ^{23}Al lifetime using these p-branches. Perajarvi et. al [13] reported two γ rays originated from the decay of the isobaric analog state in ^{23}Mg with mass-separated ^{23}Al. In order to determine the ground state spin and parity of ^{23}Al, we need experimental data for β-decay branching ratios to different final excited states of ^{23}Mg. In this dissertation, I will present a study of the β-decay of ^{23}Al. With more than 99% pure samples of ^{23}Al separated by MARS, we use β detection and $\beta - \gamma$ coincidence techniques to determine the branching ratios and logft values for transitions to individual states in the daughter nucleus ^{23}Mg. This makes the unambiguous determination of the spin and parity of the ^{23}Al ground state possible.

The proton capture reaction ^{22}Na(p,γ)^{23}Mg is an important candidate for depleting ^{22}Na out of NeNa cycle. Although a few direct measurements [14, 15] and many spectroscopic studies [12, 13, 16, 17, 18] have been done, this reaction rate in stellar environments is still uncertain. It seems that resonance capture plays an overwhelming role. The corresponding resonances are excited states in ^{23}Mg. The reaction ^{22}Na(p,γ)^{23}Mg is difficult to study because it involves a ^{22}Na radioactive target and there is a large density of states that can not be easily separated and identified at this excitation energy. Some of these states, including the isobaric analog state of ^{23}Al, are populated in the β-decay of ^{23}Al. The IAS of ^{23}Al could be identified by its preferential population and by the determination of its logft. Our experiment successfully separated two important states at high excitation energy and identified the IAS.

B. Astrophysical Motivation

There is special interest in the structure of ^{23}Al due to its nuclear astrophysics significance, namely its role in the depletion of ^{22}Na from the NeNa cycle by the ^{22}Mg(p,γ)^{23}Al reaction. The nucleus ^{23}Al is a weakly bound proton-rich nucleus. Its last proton separation energy is only 0.123(19) MeV [19], and it is close to the drip line. Prior to this work, the ground state spin and parity of ^{23}Al was uncertain, with assignments that included $1/2^+$, $3/2^+$ and $5/2^+$. Before February 2007, the National Nuclear Data Center (NNDC) at Brookhaven National Lab (BNL) gave $3/2^+$ for the ^{23}Al ground state [20]. The mirror nucleus ^{23}Ne has $J^\pi=5/2^+$ for its ground state. Recently it was claimed from experimental evidence and accompanying theoretical calculations [21] that the proton-rich ^{23}Al is a halo nucleus. This can be explained only if the last proton is in the $2s_{1/2}$ and not the $1d_{5/2}$ orbital (The level inversion cartoon is shown in Fig. 1), i.e. $J^\pi=1/2^+$ for the ^{23}Al ground state. Several microscopic nuclear structure calculations (nonlinear relativistic mean field and Skyrme-Hartree-Fock) also found $J^\pi = 1/2^+$ for the ^{23}Al ground state [22, 23, 24]. These calculations support level inversion. The existing experimental data, such as the systematics of the energies of the first two states in odd-mass Al isotopes, seem to support level inversion as well. The isobaric multiplet mass equation (IMME) and mirror symmetry, however, do not support it.

The ground state spin and parity for ^{23}Al can make a significant difference to the amount of ^{22}Na that is left following explosive nucleosynthesis [25]. As an example, using $1/2^+$ instead of $5/2^+$, we calculate the astrophysical S-factor [1, 2] and stellar reaction rate for ^{22}Mg(p,γ)^{23}Al reaction and find an increase of 30-50 times for the temperature range of ONe novae T_9=0.1-0.5 (temperature in the units of 10^9 K), as shown in Fig. 2, over the current estimate, which assumes $5/2^+$. This is due to

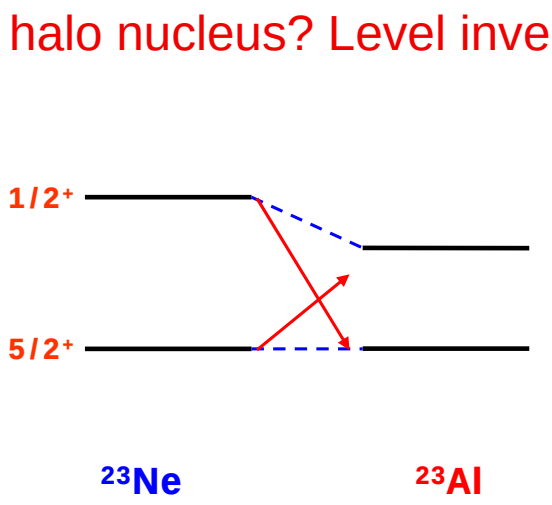

Fig. 1. Level inversion in ^{23}Al suggested by Cai et al. [21] and Zhang et al. [24]

the absence of a centrifugal barrier for the last proton in ^{23}Al, which allows the wave function of the barely bound proton in the final state to extend far beyond the nuclear interior, and thus increases its overlap with the wave function of the incoming proton. In an explosive process this increase results in a significant depletion of ^{22}Mg before it β decays into ^{22}Na, and, if confirmed, could explain the non-observation of the 1.275 MeV γ-ray from ^{22}Na, which is the last step of the reaction chain that is named the hot NeNa cycle. Determining the ground state structure of ^{23}Al is required if we are to better understand the ^{22}Na yield in ONe novae. It is important both for nuclear structure physics and for its consequences on nuclear astrophysics.

In the ^{23}Mg energy level scheme, those excited states with energy more than the proton separation energy (S_p=7580.3(13) keV) are resonances in the reaction ^{22}Na$(p,\gamma)^{23}$Mg. They could play certain roles in the reaction rate of ^{22}Na$(p,\gamma)^{23}$Mg at astrophysical energies. This issue has received much attention related to the anomalous Ne isotopic ratio in some meteorites (Ne-E anomaly) [7, 8, 26] and the breakout from the NeNa cycle. Some of the excited states populated in the β-decay of ^{23}Al,

such as those having proton decay branches, contribute to the proton capture reaction rate in novae. Their precise position and strengths remain unknown. This leads to uncertainties of a few orders of magnitude in the reaction rate [18, 27]. Therefore, further investigation is necessary.

C. Dissertation Outline

Totally, there are six chapters in this dissertation. Chapter I introduces the motivation and background of this research project. Then Chapter II describes the theories of hydrogen burning and of β decay. The experimental setup and procedures, including detectors and the data acquisition system, will be given in Chapter III. Chapter IV presents a detailed discussion of the data analysis and results. Chapter V discusses the astrophysical consequences of the ^{23}Al structure to two important reactions, $^{22}\mathrm{Na}(p,\gamma)^{23}\mathrm{Mg}$ [7, 8] and $^{22}\mathrm{Mg}(p,\gamma)^{23}\mathrm{Al}$. A summary and outlook are given in the last chapter, Chapter VI.

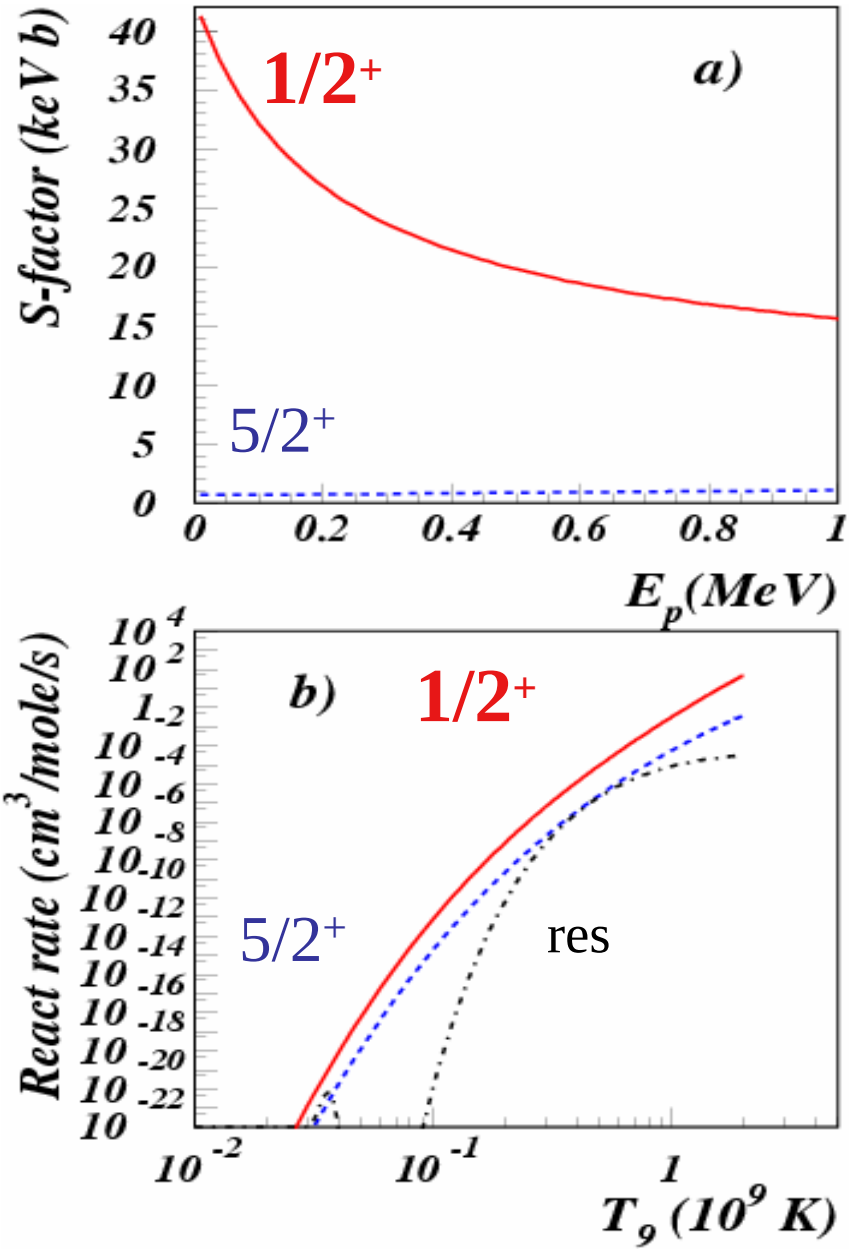

Fig. 2. Astrophysical S factor and stellar reaction rate for for the ^{22}Mg(p,γ)^{23}Al reaction, calculated assuming J$^{\pi}$=5/2^{+} (blue dashed line), or J$^{\pi}$=1/2^{+} (orbital inversion, red full line) for the ground state of ^{23}Al. Resonance contribution is represented by the black dashed line. T$_9$ is the temperature in units 10^9 K [25].

CHAPTER II

THEORETICAL BACKGROUND

Nuclear reactions play a crucial role in the evolution of the Universe as well as in various stellar phenomena such as stellar nucleosynthesis in novae and supernovae [28, 29]. The origin of the chemical elements is a big interesting quest and also an important clue for understanding the Universe. Extremely unstable nuclei can be found synthesized under extreme conditions, for example, in environments with high temperature and high neutron or proton densities. Novae, supernovae, γ–ray bursts, X–ray bursts, or other dynamic astrophysical sites provide such environments. Explosive hydrogen burning occurs at such high temperature and high density conditions in hydrogen-rich environments. These unstable nuclei will evolve into stable nuclei via β–decay, α–decay, proton decay, neutron emission, etc. This Chapter presents the theories of hydrogen burning and of β–decay as theoretical background for our experiments.

A. Hydrogen Burning

Hydrogen is the most abundant (75%) element in stars. It can undergo thermonuclear reactions at T$\geq$7x10^{6}K. The basic concept of the hydrogen burning process is represented as follows, where Q=26.73 MeV [1],

$$4p \rightarrow {}^4He + 2\beta^+ + 2\nu_e + 26.73MeV. \tag{2.1}$$

Two sets of reactions, the proton-proton (pp) chain and the CNO cycle, can convert hydrogen into helium, thereby providing the energy needed for a star's luminosity. This fusion of hydrogen into helium fuels the prodigious luminosity of stars for the greater part of their lives.

1. Proton-Proton Chain (*pp* chain)

There is only hydrogen, with small amounts of He, available in the first-generation stars where energy is produced predominantly by *pp* chain reactions. Due to its high nuclear binding energy for the reaction Eqn. 2.1, the chain reaction has to go through a series of steps to produce helium. Bethe and Critchfield [30] demonstrated that the weak reaction Eqn. 2.2 could give rise to a process resulting in stable deuterium,

$$p + p \rightarrow {}^{2}H + \beta^{+} + \nu_{e}, \tag{2.2}$$

where K=Q-2m$_e c^2$=0.42 MeV is the kinetic energy shared by the positron and the neutrino. Q is the total energy released in the process, including the annihilation energy of the emitted positron. This weak reaction cross section is about 20 orders of magnitude smaller than cross sections associated with purely nuclear reactions. This cross section is so small that only theoretical estimates exist. The Sudbury Neutrino Observatory (SNO) scientists, however, measured the charged-current breakup reaction on the deuteron, the inverse of the proton proton (pp) reaction, which has been used to place some direct constraints on the size of the pp rate [31]. The hydrogen burning rate is thus limited by the weak force which is used to synthesize the stable isotope deuterium. Consequently, stars, such as our Sun, consume their nuclear hydrogen fuel slowly and still exist today.

Deuterium burning can occur via the reaction given in Eqn. 2.3 which produces ${}^{3}He$,

$$d + p \rightarrow {}^{3}He + \gamma. \tag{2.3}$$

The burning of ${}^{3}He$ is more complicated than the hydrogen and deuterium burning. Depending on the temperature of stars (T_6, in units of 10^6 K), ${}^{3}He$ burning goes through three different paths to convert into ${}^{4}He$. Most ${}^{3}He$ (86%) converts into

^4He via the reaction given by

$$^3He + {}^3He \rightarrow {}^4He + 2p. \tag{2.4}$$

This reaction chain branch, including Eqn. 2.2, 2.3 and 2.4, is named the *pp* chain I (PPI). The rest of ^3He (14%) coverts into ^4He via other reaction chain branches, the so called PPII and PPIII. The entire energy released from the three p-p chains is the same, 26.73 MeV. But the escaping neutrinos carry away diiferent amounts of energy from the three different p-p chains. These energy losses for PPI, PPII and PPIII are 0.53 MeV, 1.07 MeV and 7.56 MeV, respectively. The details for these three reaction chains are shown in Fig. 3.

In summary, the rate of the p-p chain depends entirely on the rate of the p + p reaction given in Eqn. 2.2. The p-p chains provide an important mechanism by which ^4He is synthesized from hydrogen alone without heavier nuclei acting as a catalyst. This is a good starting point for presenting a general theory for stellar nucleosynthesis of all heavy elements.

2. The Carbon-Nitrogen-Oxygen (CNO) Cycle

Most of the present stars are second or third generation stars (Population I). They consist of hydrogen and other heavier elements such as carbon, nitrogen and oxygen that are synthesized in massive first generation stars. Bethe and Weizsacker proposed the CNO cycle [32, 33, 34]. The CNO cycle, shown in Fig. 4, is a series of nuclear reactions where carbon, nitrogen and oxygen are used as catalysts to transform hydrogen into helium. It consists of the following sequence of reactions:

$$^{12}\mathrm{C}(p,\gamma)^{13}N(e^+,\nu)^{13}C(p,\gamma)^{14}N(p,\gamma)^{15}O(e^+,\nu)^{15}N(p,\alpha)^{12}C. \tag{2.5}$$

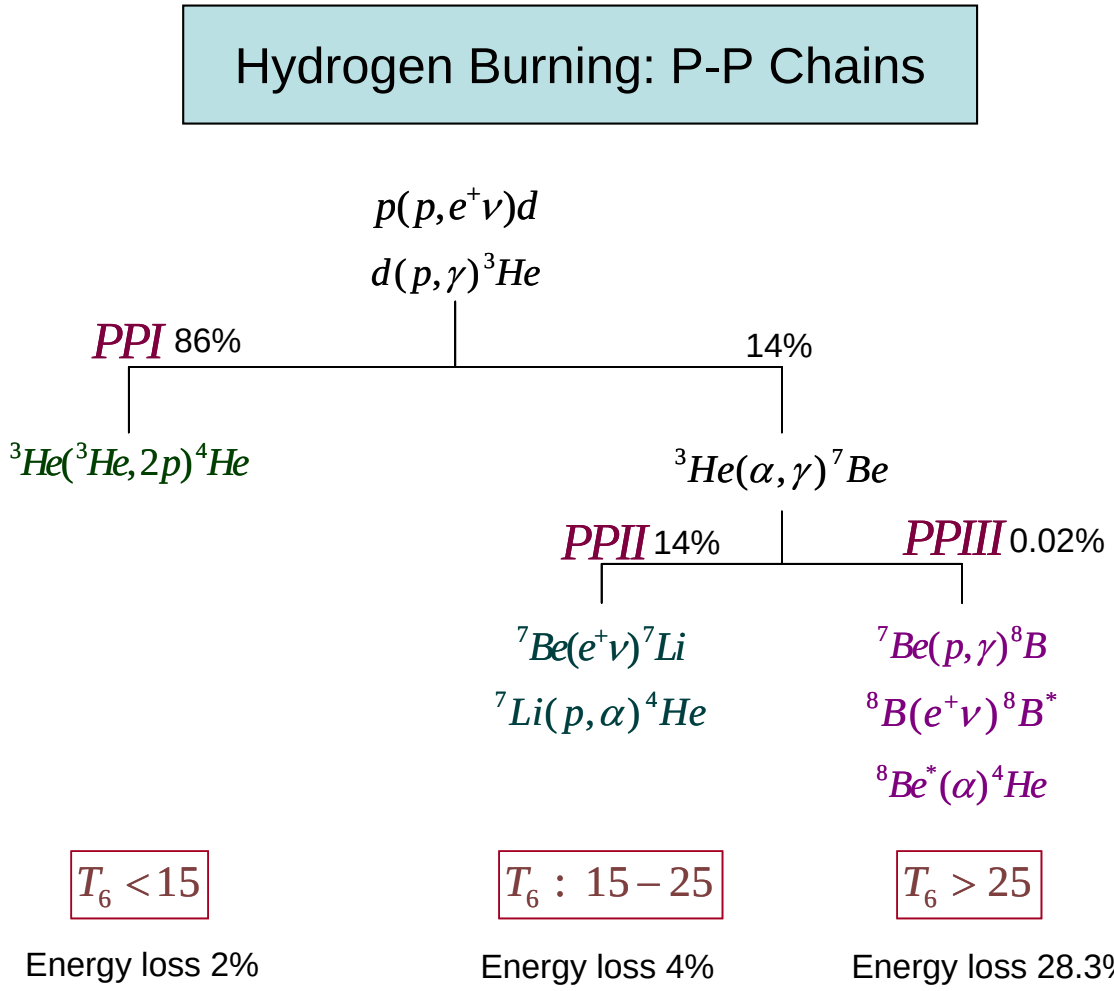

Fig. 3. Shown here is the scheme of Hydrogen burning in the Sun. The relative fractions of the PPI, PPII and PPIII chain reactions depend on the stellar mass and temperature. The net result is to create alpha particles from the fusion of four hydrogen particles. α–particles act as a catalyst in chains of PPII and PPIII due to the interaction of one α-particle leading eventually to the production of two alphas. T_6 is the temperature in the units of 10^6 K.

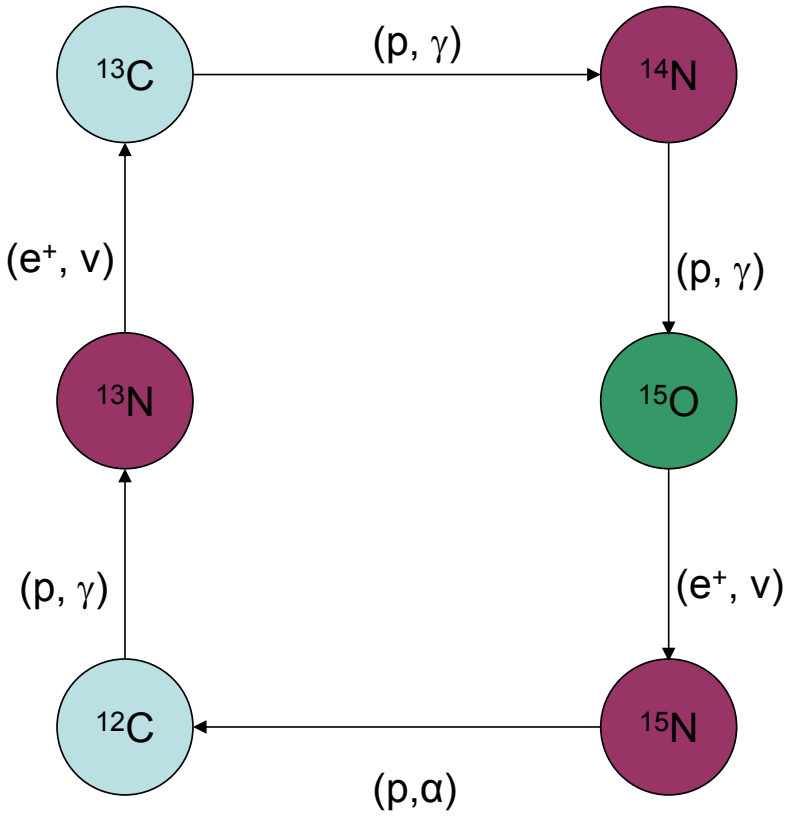

Fig. 4. CNO Cycle: carbon, nitrogen and oxygen are used as catalysts to transform hydrogen into helium.

This CNO cycle can take place only if the indispensible C and N nuclei are present and temperature is sufficient. It is far more temperature-dependent than the proton-proton chain hydrogen burning. The cycle yields 26.73 MeV of energy and is another way that a star converts hydrogen into helium.

During the CNO cycle, carbon, nitrogen, and oxygen catalyze the nuclear reactions, so the total number of carbon, nitrogen, and oxygen nuclei remains the same. However, carbon and oxygen gradually get converted into nitrogen. The loss of catalytic materials to the CNO cycle process occurs via the ^{15}N(p,γ)^{16}O escape reaction. This reaction leads to a subsequent set of reactions:

$$^{15}N(p,\gamma)^{16}O(p,\gamma)^{17}F(e^{+},\nu)^{17}O(p,\alpha)^{14}N. \tag{2.6}$$

This reaction chain restores catalytic material to the CNO cycle. Thus the second cycle exists, and the two cycles are named as the CNO bi-cycle 5. The importance of the second cycle relative to the CNO cycle is governed by the ratio of the S(0) factors for two reactions ^{15}N(p,α)^{12}C and ^{15}N(p,γ)^{16}O. This ratio is around 1000:1, i.e. the second cycle contributes very little to the total rate of energy production. But it is very important for the nucleosynthesis of the ^{16}O and ^{17}O isotopes.

With an increase of temperature in the hydrogen burning process, we should consider more synthesized nuclei, such as ^{18}F, ^{18}O and ^{19}F. The ^{17}O$(p,\gamma)^{18}$F reaction begins to play a role in the subsequent hydrogen burning of ^{17}O relative to ^{17}O$(p,\alpha)^{14}$N. This leads to a CNO tri-cycle:

$$^{17}O(p,\gamma)^{18}F(e^{+},\nu)^{18}O(p,\alpha)^{15}N(p,\gamma)^{16}O(p,\gamma)^{17}F(e^{+},\nu)^{17}O. \tag{2.7}$$

Similarly, the ^{18}O(p,γ)^{19}F reaction also can not be neglected in the hydrogen burning

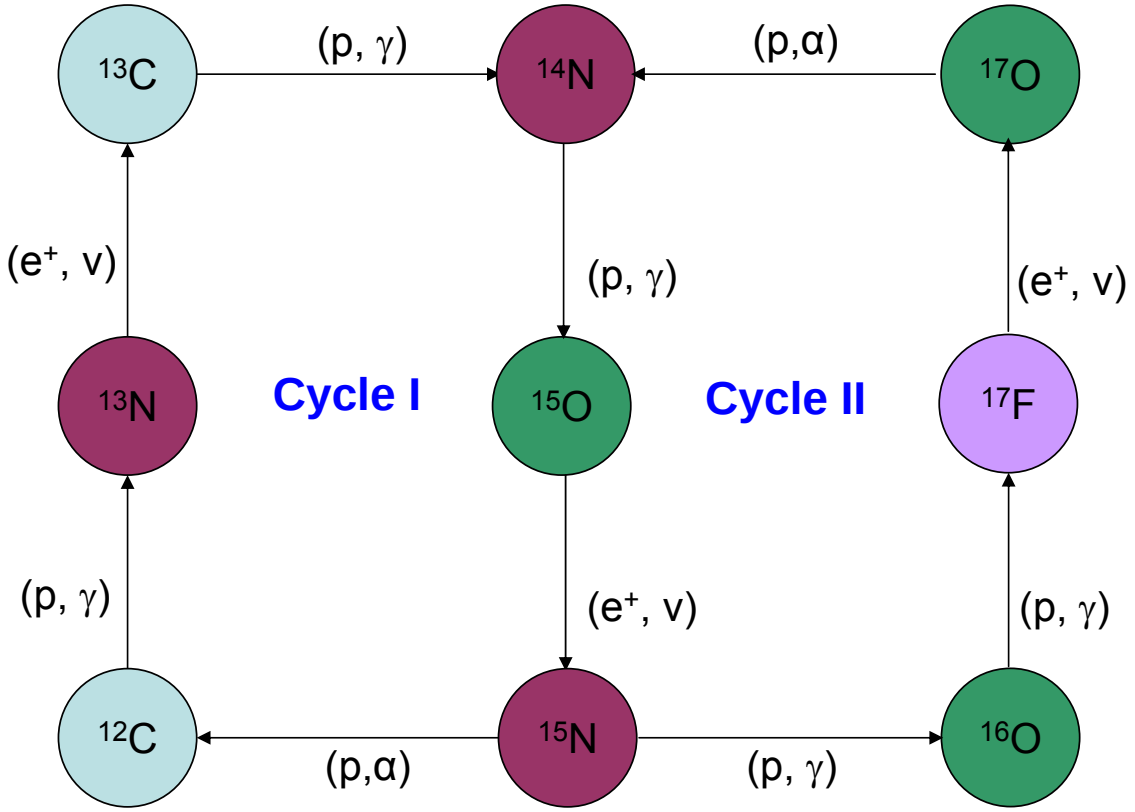

Fig. 5. The scheme shows the CNO bi-cycle, the interlocking sequence of reactions involved in hydrogen burning via the CNO bi-cycle.

of ^{18}O. This leads to a CNO quad-cycle:

$$^{18}O(p,\gamma)^{19}F(p,\alpha)^{16}O(p,\gamma)^{17}F(e^+,\nu)^{17}O(p,\gamma)^{18}F(e^+,\nu)^{18}O. \tag{2.8}$$

These reaction chains (4 CNO cycles) can be found in Fig. 6, which shows the hot-CNO (HCNO) cycle. The HCNO cycles include proton-induced reactions on the unstable nuclei ^{13}N, ^{17}F and ^{18}F. Catalytic material could be lost from the cycles via the ^{19}F(p,γ)^{20}Ne reaction, which could link to the NeNa cycle at a higher temperature. When T_9 >0.3-0.4, the CNO cycle breakout leads to the rapid proton (rp) process via the routes ^{15}O$(\alpha,\gamma)^{19}$Ne and ^{18}Ne$(\alpha,p)^{21}$Na [35]. This is shown in Fig. 7.

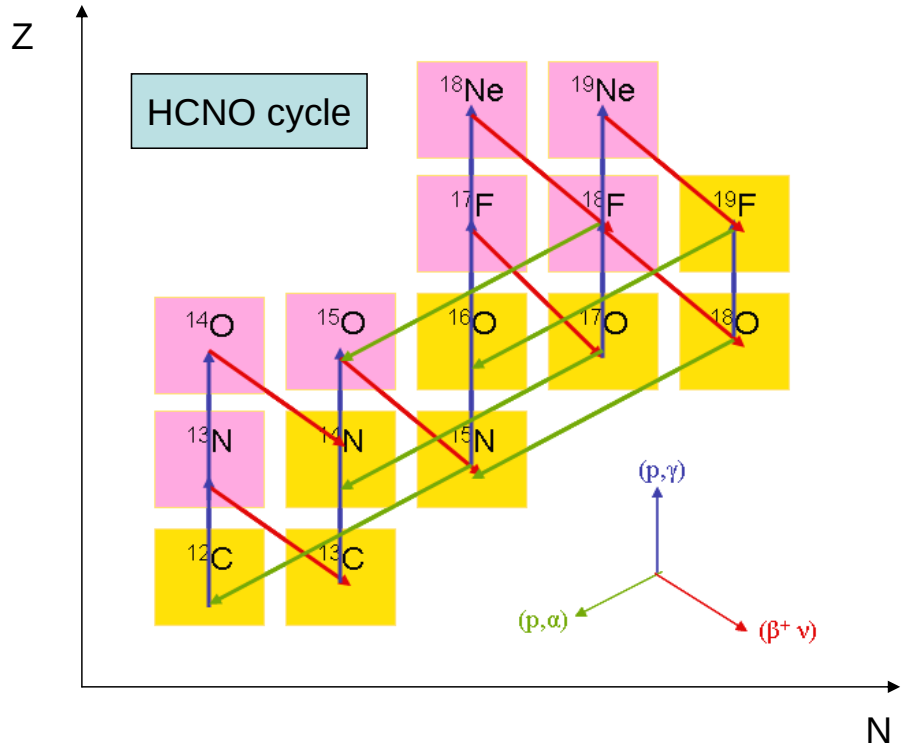

Fig. 6. The scheme shows the HCNO Cycle. It illustrates four CNO cycles involved in the conversion of hydrogen into helium. The HCNO cycles include proton-induced reactions on the unstable nuclei ^{13}N, ^{17}F and ^{18}F

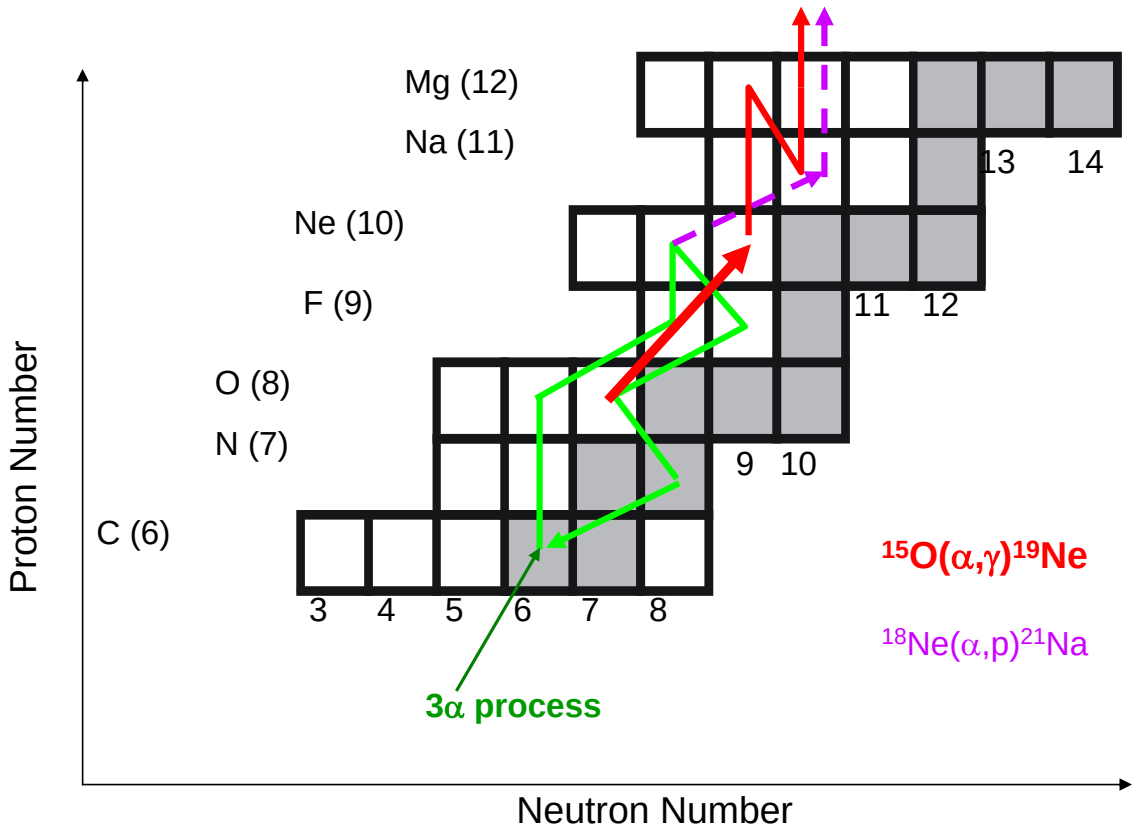

Fig. 7. Shown here is the breakout from the Hot CNO cycle. When T_9 >0.3-0.4, the CNO cycle breakout leads to the rapid proton (rp) process via the routes $^{15}\mathrm{O}(\alpha,\gamma)^{19}\mathrm{Ne}$ and $^{18}\mathrm{Ne}(\alpha,p)^{21}\mathrm{Na}$.

3. Oxygen Neon (ONe) Novae and Neon Sodium (NeNa) Cycle

a. Oxygen Neon (ONe) Novae

White Dwarfs (WD) are the most common stars in the universe [36]. There are possibly more white dwarfs than all the other stars combined, because low-mass stars are born more frequently, and low-mass stars create white dwarfs. Most of the white dwarfs occur in binary systems. It is important to study white dwarfs because the ages of white dwarfs reveal the history of the galaxy.

Novae are common events in the galaxy. Novae might eventually turn into supernovae (SN), and involve thermonuclear explosions. Two beautiful pictures give a basic idea how it looks [37, 38]. Figure 8 is the most famous supernova 1987A. Figure 9 shows the dust being created and thrown out in supernova explosions.

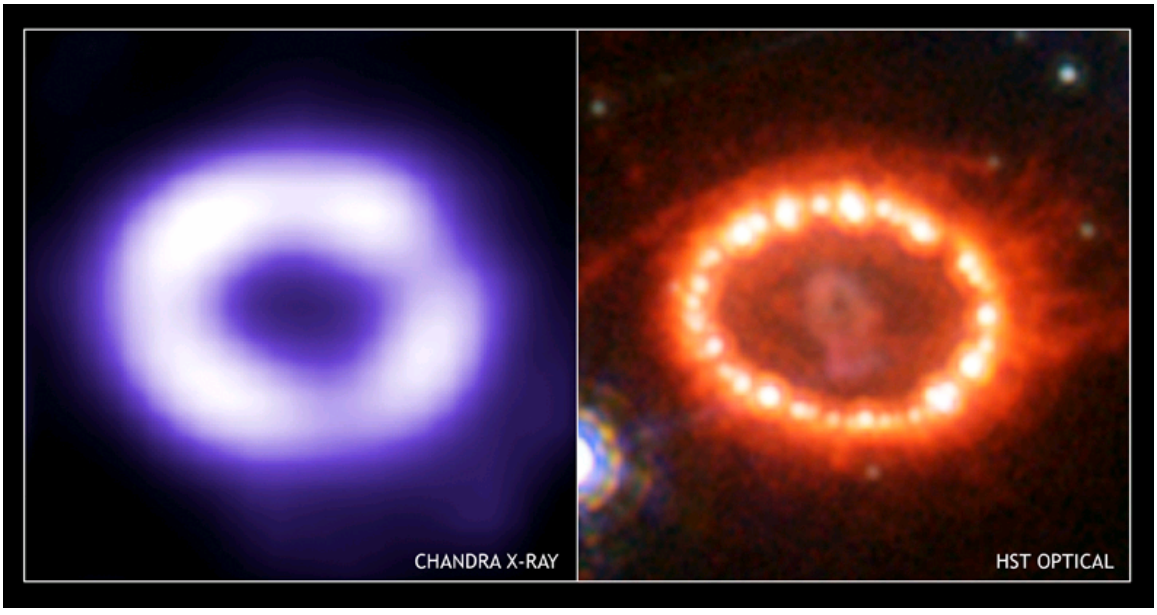

Fig. 8. Supernova 1987A

Dwarf novae are the most gentle of the cataclysmic events. Although novae are not the major source for the production of heavy nuclei, they do account for

Fig. 9. Dust being created and thrown out in supernova explosions. Picture is obtained from http://cognitivedistortion.com/

the considerable production of light and intermediate mass nuclei. According to the widely accepted nova outburst scenario, classical novae are produced by thermonuclear runaways (TNRs) which take place in the white dwarf component of a close binary system. From the nucleosynthesis viewpoint, two different nova outbursts occur in two different types of white dwarfs, Carbon-Oxygen (CO) white dwarfs and Oxygen-Neon (ONe) white dwarfs. The latter has provided a framework for the origin of the high concentrations of Ne and more massive isotopes found in the spectra of some well-observed novae [2]. We are specially interested in one long lived radioactive specie, ^{22}Na, which can be ejected in this explosive environment.

b. Neon Sodium (NeNa) Cycle

^{22}Na is thought to be produced in the thermonuclear runaway and in the high-temperature phase of ONe novae through the reaction chain shown in Fig. 10 and written as

$$^{20}Ne(p,\gamma)^{21}Na(\beta^{+},\nu)^{21}Ne(p,\gamma)^{22}Na. \tag{2.9}$$

In the NeNa cycle, reactions such as ^{20}Ne$(p,\gamma)^{21}$Na, ^{21}Ne$(p,\gamma)^{22}$Na and ^{22}Ne$(p,\gamma)^{23}$Na were well studied in a wide range of beam energies [39, 40, 41, 42, 43, 44]. For the ^{20}Ne$(p,\gamma)^{21}$Na reaction, the results indicated that the stellar rates are dominated by the direct capture (DC) into bound states rather than the tails of the resonances at high energies. However, the third excited state at E_x=2425 keV, 7 keV below the proton threshold, could contribute significantly to the overall stellar rate. For ^{21}Ne$(p,\gamma)^{22}$Na and ^{22}Ne$(p,\gamma)^{23}$Na reactions, numerous resonances as well as direct captures were found to contribute to the capture mechanisms. The total reaction rate depends almost entirely on the contribution of the resonances, particularly those at low energy. From available theoretical and experimental information, we can see

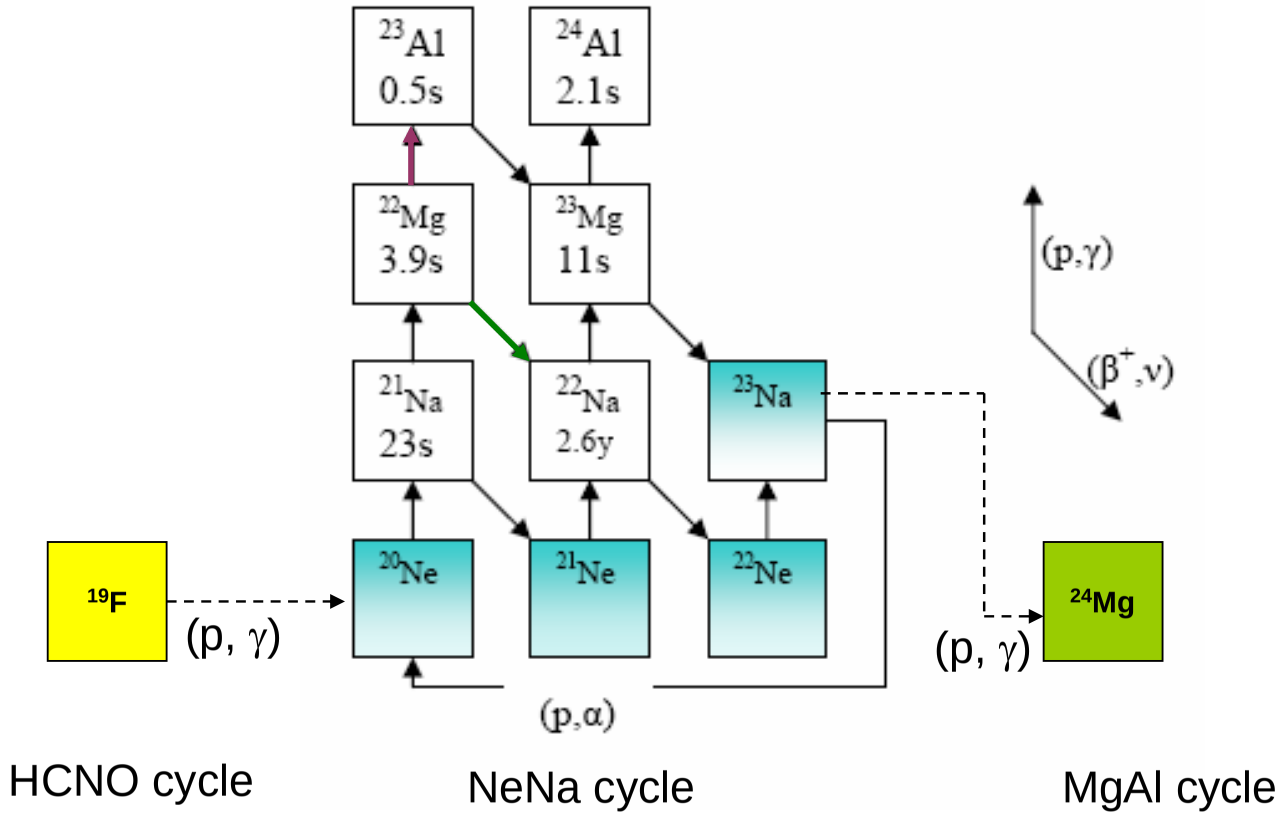

Fig. 10. The scheme shows the reaction network in the NeNa Cycle. $^{19}\mathrm{F}(p,\gamma)^{20}\mathrm{Ne}$ links to the HCNO cycle. $^{23}\mathrm{Na}(p,\gamma)^{24}\mathrm{Mg}$ leads to another high temperature MgAl cycle of hydrogen burning.

that the stellar rate for the ^{23}Na$(p,\alpha)^{20}$Ne reaction is large enough compared with the competing reaction ^{23}Na$(p,\gamma)^{24}$Mg to guarantee NeNa cycling [45].

Clayton and Hoyle first suggested ^{22}Na plays an important role for the diagnosis of nova outbursts [46]. The hydrogen burning sequence of reactions via the NeNa cycle could produce substantial ^{22}Na in ONe novae. ^{22}Na, which has a life time 2.602 years, decays to an excited state of ^{22}Ne, which de-excites to its ground state by emitting a γ-ray of 1.275 MeV. A detectable γ-ray flux at this energy in nearby ONe novae, within a few kiloparsecs of the Sun, could be observed by space-based γ-ray telescopes, such as the International Gamma-Ray Astrophysical Laboratory (INTEGRAL). Unfortunately, all observations have failed to detect these γ-rays from ^{22}Na. An upper limit (3.7x10$^{-8}M_{\odot}$) on the ejected ^{22}Na mass by a nova in the Galactic disk has been derived from observational data. This limit is well below the theoretical model estimations for ^{22}Na ejected from novae.

This discrepancy could be due to a poor knowledge of the reaction cross sections employed in the network calculations for the rp-process nucleosynthesis. ^{22}Na itself could be depleted by the radiative proton capture reaction ^{22}Na$(p,\gamma)^{23}$Mg, which is considered as a main depletion candidate [7, 8]. Depending on the temperature of the burning region, there are two paths, cold and hot NeNa cycles, for ^{22}Na to be produced in ONe novae [47]. In Fig. 10, if ^{21}Na β^+ decays into ^{21}Ne, then proton captures to ^{22}Na; this is called the cold NeNa cycle. The reaction chain for this process is

$$^{20}Ne(p,\gamma)^{21}Na(\beta^+,\nu)^{21}Ne(p,\gamma)^{22}Na(p,\gamma)^{23}Mg(\beta^+,\nu)^{23}Na(p,\alpha)^{20}Ne. \qquad (2.10)$$

If ^{21}Na captures a proton to form ^{22}Mg, then goes to ^{22}Na by β decays; this is

called the hot NeNa cycle. The reaction chain is

$$^{20}Ne(p,\gamma)^{21}Na(p,\gamma)^{22}Mg(\beta^+,\nu)^{22}Na(p,\gamma)^{23}Mg(\beta^+,\nu)^{23}Na(p,\alpha)^{20}Ne. \quad (2.11)$$

In the hot NeNa cycle, the explosive phase of novae, the ^{22}Mg$(p,\gamma)^{23}$Al reaction could play a major role leading to a serious reduction of the residual ^{22}Na abundance. The explosive phase of novae is so fast and short that the equilibrium with photodissociation may not be reached. The ^{22}Mg$(p,\gamma)^{23}$Al reaction is dominated by direct proton capture to the ground state and by resonant capture through the first excited state in ^{23}Al.

In order to get the reaction rate of ^{22}Mg$(p,\gamma)^{23}$Al, we need to know the structure of ^{23}Al. The ground state spin and parity of ^{23}Al can make a significant difference to the amount of ^{22}Na that is left following explosive nucleosynthesis [25], as was discussed in Chapter I.

B. The β–decay Theory

Nuclear β–decay plays a major role in stellar nucleosynthesis. Historically, the study of β–decay provided the first physical evidence of the neutrino. In 1934 Fermi published a very successful β–decay theory where neutrinos were produced. In 1957, the non-conservation of parity in β–decay was proposed by Lee and Yang [48] and was verified by Wu [49] via ^{60}Co β-decay. The superallowed $0^+ \rightarrow 0^+$ β– decay has been used to probe the weak interaction to test the unitarity of the Cabibbo-Kobayashi-Maskawa (CKM) quark-mixing matrix in the Standard Model [50, 51, 52].

The nuclei in stars or novae processes which are produced with unusual proton to neutron ratio are located far from the valley of β–stability and usually evolve to stable nuclei via β–decay.

1. Classifications and Selection Rules for β–decay

a. Classifications

β-decay is a type of weak radioactive decay where a β particle (β^-–decay involving an electron or β^+–decay involving a positron) and neutrinos are emitted, keeping mass number constant [53, 54].

In β^-–decay, the weak interaction converts a neutron (n^0) into a proton (p^+) while emitting an electron (e^-) and an anti-neutrino ($\bar{\nu}_e$):

$$n^0 \rightarrow p^+ + e^- + \bar{\nu}_e. \tag{2.12}$$

From the viewpoint of particle physics, this is due to the conversion of a down quark to an up quark by the virtual emission of a W^- boson which subsequently decays into an electron and an anti-neutrino.

In β^+–decay, energy is used to convert a proton into a neutron, a positron and a neutrino:

$$\text{Energy} + p^+ \rightarrow n^0 + e^+ + \nu_e. \tag{2.13}$$

Fundamentally, an up quark is converted into a down quark, emitting a virtual W^+ boson which then decays into a positron and a neutrino. β^+–decay needs energy due to the mass of the neutron being greater than the mass of the proton.

In all the cases where β^+–decay is allowed energetically, it is accompanied by the electron capture process, where an atomic electron is captured by a nucleus with the emission of a neutrino:

$$\text{Energy} + p^+ + e^- \rightarrow n^0 + \nu_e. \tag{2.14}$$

But if the energy difference between initial and final states is low, electron capture can occur without being accompanied by positron emission.

In summary, β-decay collectively refers to the three distinct processes discussed above. Examples are shown below:

$$^{137}_{55}\mathrm{Cs} \rightarrow {}^{137}_{56}\mathrm{Ba} + e^- + \bar{\nu}_e \qquad (\beta^- - decay), \tag{2.15}$$

$$^{23}_{13}\mathrm{Al} \rightarrow {}^{23}_{12}\mathrm{Mg} + e^+ + \nu_e \qquad (\beta^+ - decay), \tag{2.16}$$

$$^{22}_{11}\mathrm{Na} + e^- \rightarrow {}^{22}_{10}\mathrm{Ne} + \nu_e \qquad (EC - decay). \tag{2.17}$$

There is a special and interesting case named double β–decay found in 1986. In this process, the nucleus undergoes double β–decay where the charge of the nucleus changes by two units. In double β–decay, two neutrons in the nucleus are converted to protons, and two electrons and two electron neutrinos (anti-neutrinos) are emitted. It is also know as two neutrino double β–decay. It is among the rarest known kinds of radioactive decay. The following isotopes are capable of undergoing double β–decay, but have no other decay paths: ^{48}Ca, ^{76}Ge, ^{82}Se, ^{96}Zr, ^{100}Mo, ^{116}Cd, ^{134}Xe, ^{136}Xe, ^{128}Te, ^{130}Te, ^{150}Nd, and ^{160}Gd. The $\beta\beta\bar{\nu}\bar{\nu}$ decay has been observed. The neutrinoless double beta decay which is shown in Fig. 11 [55], however, has not been observed. Numerous experiments have been carried out and proposed to search for the neutrinoless double beta decay, as its discovery would indicate that neutrinos are indeed Majorana particles and would allow a calculation of neutrino mass which is a very interesting and important quantity.

b. Selection Rules

During the transition between the initial and final states in the β-decay process, angular momentum must be conserved. This leads to a restrictive set of selection rules [53, 54].

Both of the created particles (β particle and neutrino) are fermions, which have

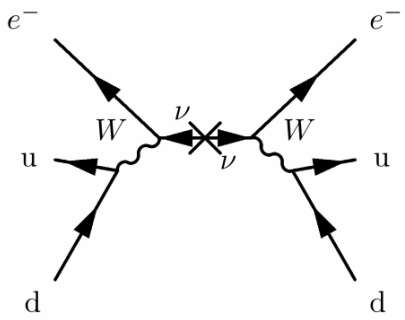

Fig. 11. The cartoon shows the neutrinoless double β–decay process.

an intrinsic spin, S=1/2. When the orbital angular momentum is zero ($\ell = 0$, named allowed approximation) during the emission of neutrino and β particle in the transition between initial and final states, we only need consider the intrinsic spins of the neutrino and β particle. For the anti-parallel (S=0) case of the β particle and neutrino, the total change in nuclear spin between initial and final states must be 0. i.e. $\triangle$J = 0. This is named Fermi decay. For the parallel (S=1) case of the β particle and neutrino, the total change in nuclear spin between initial and final states must be 0 or 1. i.e. $\triangle$J = 0,1. This is named Gamow-Teller decay. Both Fermi and Gamow-Teller decays obey the condition $\triangle\pi = (-1)^{\ell}$, where π is the parity of the system. At $\ell = 0$, the parities of the initial and final states remain the same. When the orbital angular momentum is not zero ($\ell \neq 0$), the decay is classified as forbidden. The forbidden decays occur with a much smaller probability than allowed decays shown above.

The bigger the value of ℓ, the higher the order of forbiddenness. i.e. the first, second, third, $\cdots$ forbidden decays are related to $\ell = 1, 2, 3, \cdots$ respectively. The higher the order of forbiddenness, the less the probability of undergoing each successive level of forbidden decay. i.e. it usually decreases by a factor of around 10^4. Both Fermi and Gamow-Teller type decays can happen during a forbidden decay. For example, when $\ell = 1$, it is the first forbidden decay. At S=0, i.e. Fermi type decay, it requires

Table I. The selection rules for allowed and forbidden β-decay transitions and associated $\log ft$ ranges.

Type of β-decay	$\triangle$J	$\triangle\pi$	$\log ft$
Super Allowed	0	No	2.9-3.7
Allowed	0,1	No	4.4-6.0
First Forbidden	0,1,2	Yes	6-10
Second Forbidden	1,2,3	No	10-18
Third Forbidden	2,3,4	Yes	17-22
Fourth Forbidden	3,4,5	No	22-24

$\triangle$J = 0,1. At S=1, i.e. Gamow-Teller type decay, it requires $\triangle$J = 0,1,2. The parity in both cases must change between initial and final states due to $\ell = 1$. The β-decay selection rules are shown in Table I. The data are quoted from Ref.[56, 57, 53].

2. Half Life, Branching Ratio and $\log ft$ of β-decay

a. Half Life

The half life is defined as the time needed for a radioactive specie to decay with the probability 0.5 and is related to the decay rate constant by [53, 54]

$$\mathrm{T}_{1/2} = \ln 2/\lambda, \tag{2.18}$$

where λ is the decay rate constant, and $\mathrm{T}_{1/2}$ is the half life. The decay constant λ is given by:

$$\lambda = \ln 2/\mathrm{T}_{1/2} = \int_0^{p_m} I(p)dp \approx \frac{64\pi^4 m_e^5 c^4 g^2 |\ M_{if}\ |^2}{h^7} f(Z, E_m), \tag{2.19}$$

$$f(Z, E_m) = \int_0^{p_m} F(Z, E)(\frac{(E_m - E)^2}{m_e c^2})^2 (\frac{p}{m_e c})^2 \frac{dp}{m_e c}, \tag{2.20}$$

$$F(Z, E) = \frac{2\pi Z c}{137\upsilon(e^{\frac{2\pi Z c}{137\upsilon}} - 1)} \qquad \text{For } (\beta^+ - decay), \tag{2.21}$$

$$F(Z, E) = \frac{2\pi Z c}{137\upsilon(1 - e^{-\frac{2\pi Z c}{137\upsilon}})} \qquad \text{For } (\beta^- - decay), \tag{2.22}$$

where F(Z,E) is the Fermi function, Z is the atomic number of the parent nucleus, E is the energy of the β particles. When Z is small, the Fermi function, F(Z,E), is taken as above form. When Z is big, the Fermi function is very complicated. υ is the speed of the β particles, E_m is the maximum energy of the β particles, p is the momentum of the β particles, p_m is the maximum momentum of the β particles, m is the mass of the electron, c is the speed of light, g is the β–decay strength constant, h is the Plank constant, and $\mid M_{if} \mid^2$ is the transition matrix elements.

b. Branching Ratio

In nuclear physics, a radioactive decay can proceed to different final states i. The branching ratio (b_β^i) for a decay is the ratio between the decay rates of individual decay modes and the total decay rate. These decay probabilities are called partial decay constants, λ_i, and their sum is the decay constant (λ) for the reaction. These can be written as following

$$\lambda_i = (b_\beta^i) \times \lambda, \tag{2.23}$$

where λ_i is the partial decay constant to state i, b_β^i is the branching ratio to the final state i, and λ is the total decay rate.

c. The logft Values

From Eqn. 2.23, the partial half-life to state i can be defined as

$$\mathrm{T}_{1/2}^{partial} = \ln 2/\lambda_i, \tag{2.24}$$

where $T_{1/2}^{partial}$ is the partial half-life.

From the partial half-life and the Fermi function, the comparative half-life, $fT_{1/2}^{partial}$ (usually simply written as ft when we calculate logft for the convenience), can be defined as [53, 54]

$$fT_{1/2}^{partial} = \frac{h^7 \ln 2}{64\pi^4 m_e^5 c^4 g^2 \mid M_{if} \mid^2}. \tag{2.25}$$

In a given β transition, the comparative half-life might be used to gauge the level of forbiddenness. However, this should not be considered absolute. logft value is frequently reported because the value of the comparative half-life (ft) can extend over many orders of magnitude. Table I shows the logft values that are associated with different types of β–decays.

In our experiments, we deduced half life, branching ratios and logft values for ^{23}Al β–decay.

3. The β–delayed γ Transition and $\beta - \gamma$ Coincidence

The daughter nucleus might be left in an excited state after a β–decay. Then one or more γ-rays will be emitted due to a change in either the charge or current distribution of the nucleus giving rise to an electric or a magnetic moment respectively when the excited state decays to the ground state. Therefore, γ–ray emission is classified as electric or magnetic in character. The angular momentum L$\geq$1 which is carried off by γ–rays from the excited nuclear state obeys the relation shown below.

$$\mid J_i - J_f \mid \leq L \leq J_i + J_f, \tag{2.26}$$

where J_i and J_f are the spins of the initial and final states respectively, and L is the multipolarity of the transition.

$\triangle\pi$ is the change in parity between initial and final states. It depends on the electric (E) or magnetic (M) character of the transition and the angular momentum shown below:

$$\triangle\pi(EL) = (-1)^L, \tag{2.27}$$

$$\triangle\pi(ML) = (-1)^{L+1}. \tag{2.28}$$

It is possible for a given γ transition that several multipole radiations may be emitted. First, the lowest multipole γ transition will dominate the decay. Second, the transitions might be of mixed type with magnetic and electric transitions. The transition rates of an electric or magnetic γ-ray transition could be obtained from the electric and magnetic transition probabilities contained information on the initial and final nuclear wave functions.

The $\beta - \gamma$ coincidence method is used to study the β–decay of ^{23}Al and ^{24}Al. From the discussion above, we know β–decay is often followed by γ transitions. So we can measure β signals and γ signals, then put them into pre-set electronic modules to do a $\beta - \gamma$ coincidence measurement.

CHAPTER III

EXPERIMENTAL SETUP AND PROCEDURES

The ^{23}Al β-decay experiments have been carried out at the K500 superconducting cyclotron of Texas A&M University, using the Momentum Achromat Recoil Spectrometer (MARS) [58, 59] and the fast tape-transport system. Our technique was similar to that used before and described in previous publications [51, 60]. Experimental setup and procedure details will be presented in this chapter.

A. The Momentum Achromat Recoil Spectrometer - MARS

The layout of MARS is shown in Fig. 12. MARS, which was commissioned in 1992, is very useful for a wide variety of nuclear physics studies with its excellent mass separation and unique optics design. It is good at producing radioactive beams that make a number of reaction and spectroscopy measurements of importance to nuclear astrophysics feasible. In the past fifteen years, many nuclear reaction studies have been successfully accomplished with MARS.

The specifications for MARS are listed in Table II. More details about MARS can be found in Tribble et al [58, 59] and Azhari et al [61].

^{23}Al was produced by the ^{1}H(^{24}Mg,^{23}Al)2n reaction. A H_2 cryogenic gas target with 2.5 mg/cm^2 thickness was located in a gas cell in the primary target chamber of MARS. A schematic drawing of the liquid-nitrogen-cooled MARS gas target unit is shown in Fig. 13. The gas cell is separated from the high vacuum of the beam line by two Havar foil windows with thickness of $12.5\,\mu m$. An automatic LN_2 filling system was attached to a dewar on top of the gas cell to keep the temperature in the gas cell around $77\,K$. The pressure of the target gas in the cell is monitored remotely in the data counting room in order to check for leaks in the Havar foil windows that could

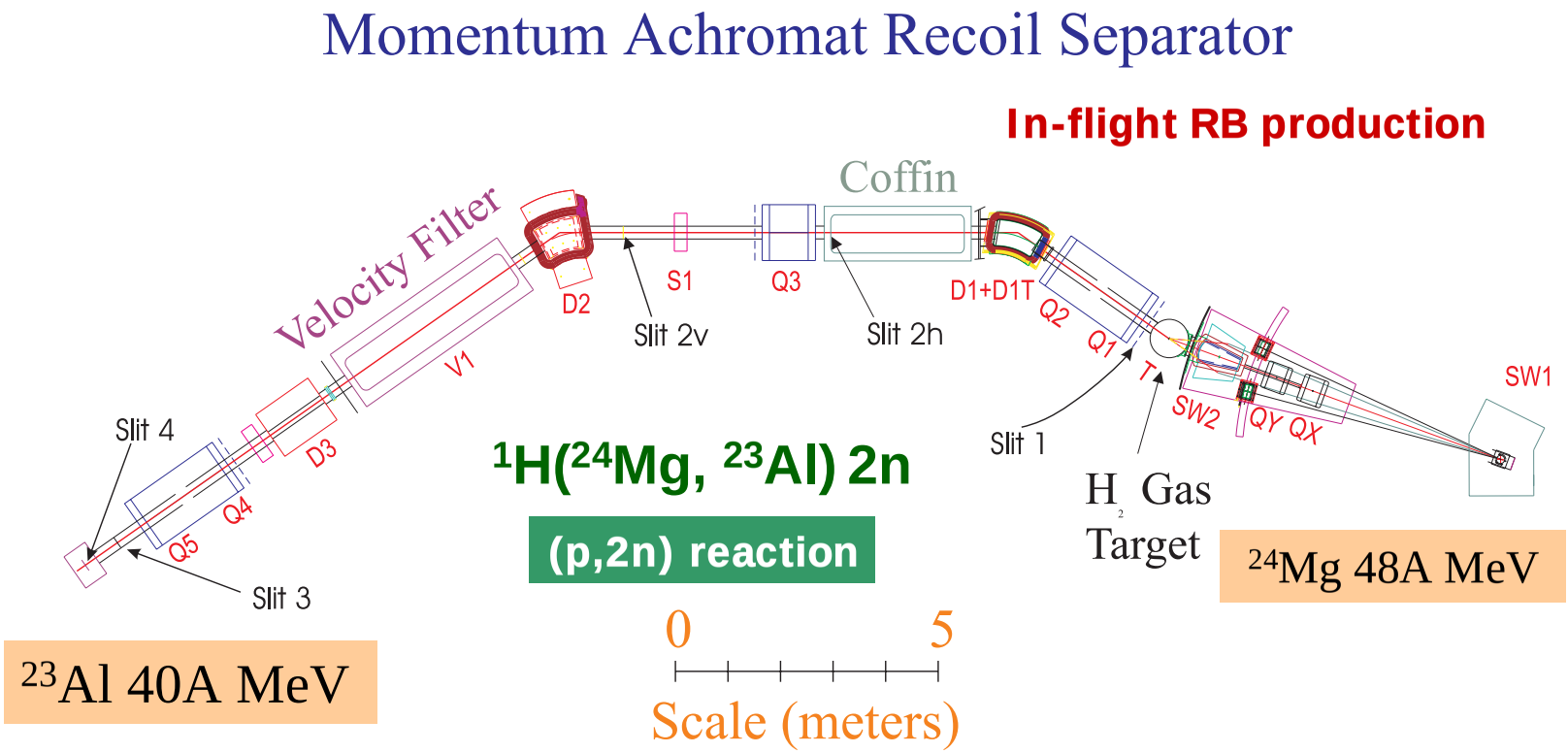

Fig. 12. Layout of the Momentum Achromat Recoil Spectrometer (MARS) at Texas A&M University.

Table II. Specifications for MARS

Overall length	19 m
Max. scattering angle[1]	30°
Max. solid angle	9 msr
Max. $B\rho$ of D1	$17.865\,m \cdot kG$
Max. $B\rho$ of D2	$17.865\,m \cdot kG$
Max. field of D3	6 kG
Max. bend angle of D3	25°
Max. electric field of the velocity filter	50 kV/cm
Max. magnetic field of the velocity filter	1 kG
Energy range with $2.0\,cm/\%$ for $\delta M/M$	$\pm 9\%$
Mass resolution [2]	1/300 (FWHM)
Path length dispersion	2 cm

[1]The angle between the axis of the primary beam and the reaction products.

[2]When $\Delta E = \pm 9\%, \Omega = 2\,msr$.

develop during ^{24}Mg beam irradiation. Beam intensities of $^{24}Mg^{10+}$ up to $\sim$200 nA were used in our experiments. In order to minimize the tunnel effect due to intense local heating in the gas, a magnetic steerer located below the cell was used. The gas cell is described in Ref. [62].

For our experiments, the MARS dipole D3 was set to bend particles by 4°. ^{23}Al selection in MARS is achieved with several pairs of slits, and the focus is realized with two quadrupole magnets situated after the last dipole. The four sets of slits are used to limit the angular spread and momentum spread of the reaction products at the final focal plane, and at the same time to get rid of the unwanted contaminants with different M/q values from what is required. In the ^{23}Al experiment, the momentum-selection slits in MARS were closed to $\pm 1.0\,cm$, which corresponds to $\sim \pm 1.3\%$ spread in energy. A beam 4.4 mm (full width at half maximum) diameter was obtained at the target chamber. At this point it contained around 85% ^{23}Al.

B. Production of ^{23}Al and ^{24}Al

In order to estimate the yields for ^{23}Al and ^{24}Al, a theoretical calculation of the excitation function for incident ^{24}Mg was done by using the PACE4 package in the LISE++ software [63]. The excitation functions for different reaction channels are shown in Fig. 14. From Fig. 14, we can see the maximum cross section region is between 45 MeV/A and 50 MeV/A. In 2005, we carried out experiments to produce ^{23}Al, beginning with production tests at two different ^{24}Mg beam energies, 45 and 48 MeV/A, respectively. At both energies ^{23}Al was produced and separated, but the latter was found more productive. Therefore, we produced ^{23}Al and studied its β-decay using a 48 MeV/A ^{24}Mg beam from the K500 cyclotron.

Tuning the ^{23}Al beam was done with a low-current primary beam. We inserted at

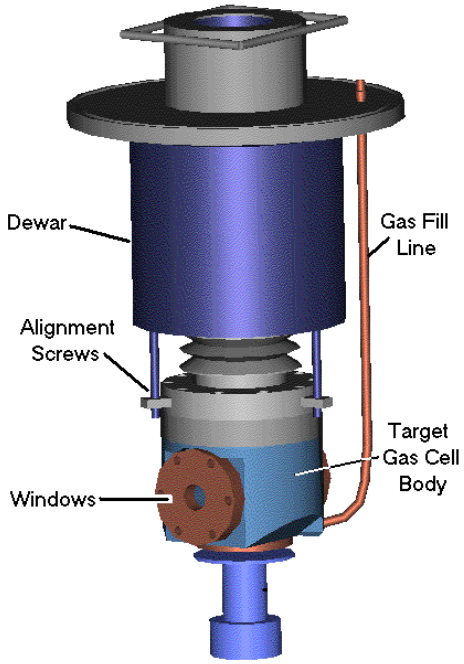

Fig. 13. The schematic drawing of the liquid-nitrogen-cooled gas target unit.

the focal plane of MARS a 5×5 cm silicon telescope consisting of a 16-strip position-sensitive detector (PSD) 300 μm thick, backed by a 1-mm-thick detector. This telescope was used first for the identification of secondary reaction products, then for the control of the selection and focus of the desired specie in the center of the beamline.

The MARS settings to get a ^{23}Al radioactive beam are listed in Table III. The data obtained at these magnets settings are shown in shown in Fig. 15, Fig. 16 and Fig.17.

For Fig. 15, the last pair of slits SL#4 up and down were open and a number of species are identified by their position (y) and energy deposited in the target detector. The line of N=Z-3 nuclei (including ^{23}Al and ^{21}Mg), of N=Z-2 nuclei (including ^{24}Al, ^{22}Mg, ^{20}Na, ...) and N=Z-1 nuclei are visible in the two-dimension plot $\triangle$E vs y. The ^{23}Al is in the middle of the detector (y$\approx$0). By closing the lower vertical slit

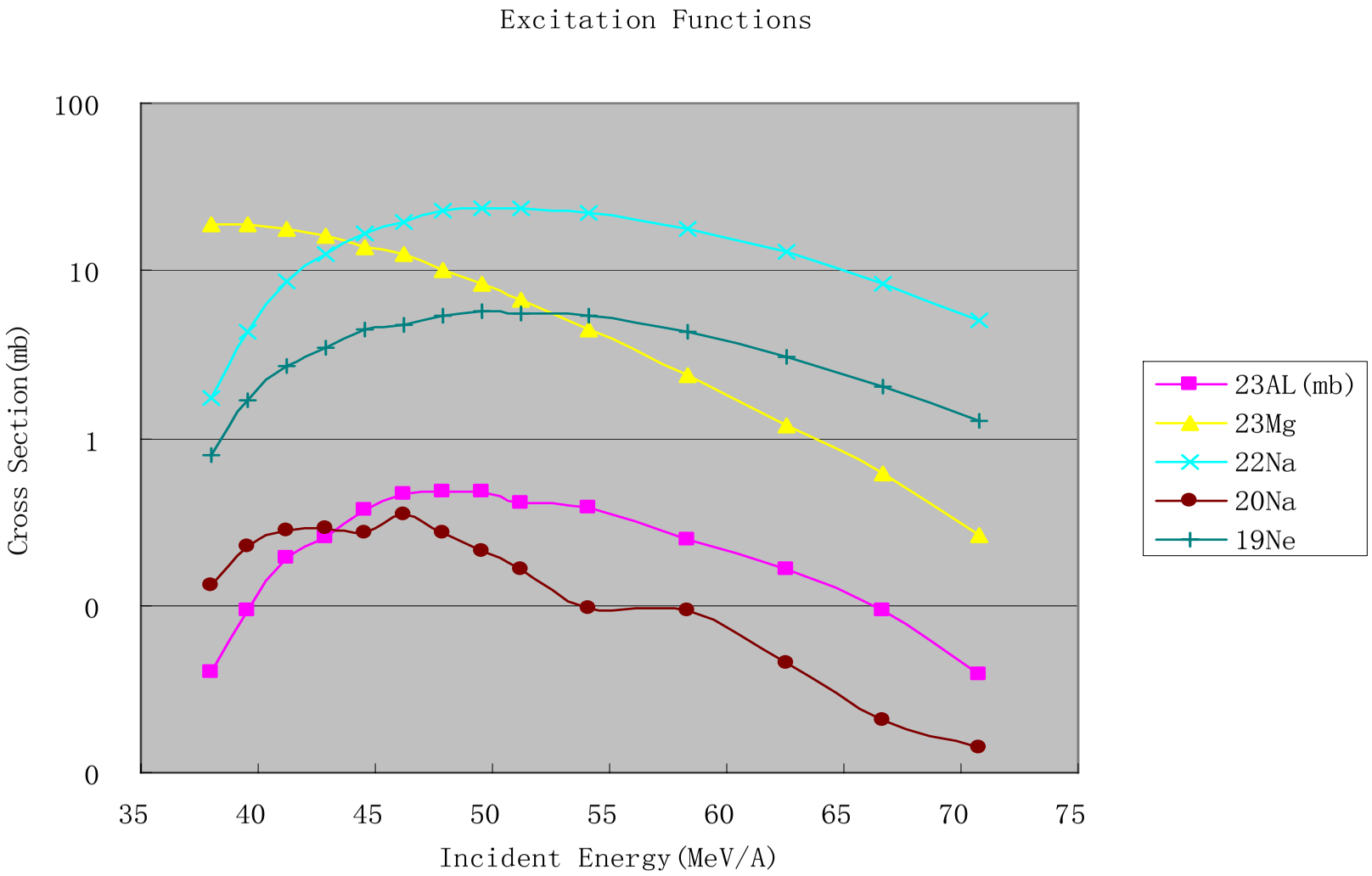

Fig. 14. The excitation functions for different reaction channels. The pink squares show ^{23}Al yields produced from the ^{1}H(^{24}Mg,^{23}Al)2n reaction. Theoretical cross sections are calculated by PACE

SL#4 to D ≈ -2 mm, most of unwanted species from the lower part are blocked (Fig. 16), with only ^{21}Mg and ^{14}O remaining as impurities. By closing the upper slit u ≈ 5.6 mm, we cut also to a minimum the impurities at lower Z still visible in Fig. 16, leaving a ∼ 85% pure ^{23}Al beam at the extraction slits in the MARS focal plane which is shown in Fig. 17. Those impurities are further cleaned with the attenuators as explained below.

After the tuning procedure, the PSD detector was dropped out of the way and the intensity of the primary beam was increased to its full strength. The secondary beam then passed through a 50-μm-thick Kapton foil window into air, then through a 0.3-mm-thick BC-104 plastic scintillator foil, which counted the ions, through a set of Al attenuators, and finally stopped in the 76-μm-thick aluminized Mylar tape of the tape-transport system. To ensure that the ^{23}Al ions all stopped within the tape, the momentum-selection slits in MARS were closed to ±1.0 cm, which corresponds to ∼ ±1.3% spread in energy. The thickness of the Al attenuators was then empirically adjusted so that ∼ 99% of the ^{23}Al ions were stopped in the tape. Since any impurities passing through MARS had different projected ranges from ^{23}Al, they were either blocked by Al attenuators or passed through the aluminized Mylar tape. This results in a purity of the collected ^{23}Al sample which was very close to 100%. With primary ^{24}Mg beam currents from the cyclotron of about 20 pnA, rates of about 4000 ^{23}Al nuclei per second were obtained with the MARS spectrometer.

The MARS settings to get the ^{24}Al radioactive beam are listed in Table IV. ^{24}Al β decay was used to do energy and efficiency calibration to HPGe γ detector. The data in the Silicon detector with the ^{24}Al settings are shown Fig. 18 and 25.

Table III. The MARS settings to get pure ^{23}Al radioactive nucleus

Primary beam	$^{24}Mg^{10+}$ at 48 Mev/u
Secondary beam	^{23}Al at 40.2 MeV/u
H_2 gas cell pressure	1.95 atm
BLD1	-569.9 A
Q1	-158.7 A
Q2	86.2 A
D12	710.0 A
D1T	25.10 A
Q3	52.2 A
Q4	-66.7 A
Q5	+92.8 A
Bv	775 A
Ev	±137 kV
D3	135.8 A
S2	18.0 A
Slit#1	L/R=±1.2 cm, U/D=±1.5 cm
Slit#2	L/R=±1.08 cm, U/D=open
Slit#3	L/R=±3 cm, U/D=±2.5 cm
Slit#4	L/R=±1.293 cm, Up=1.00 cm, down=-0.199 cm
Bend angle of D3	4°

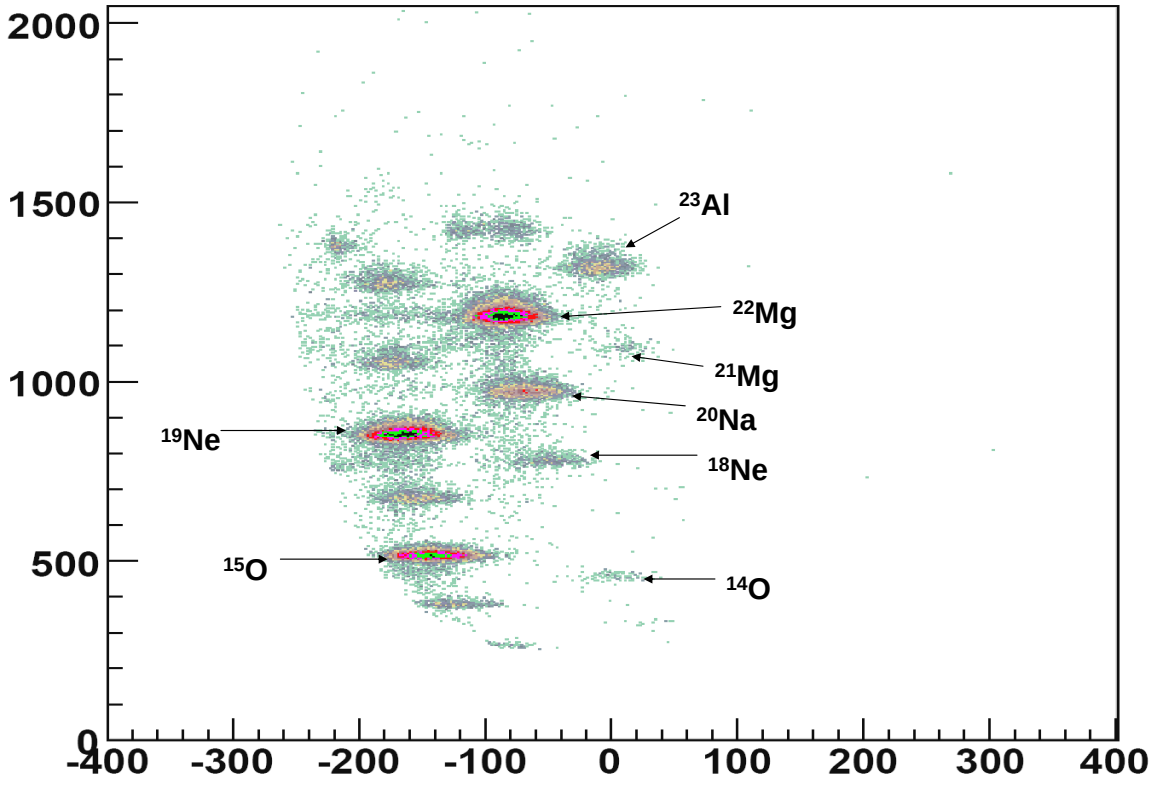

Fig. 15. △E vs Y position for ^{23}Al. Slits open and most nuclei pass and reach the MARS focal plane (target detector).

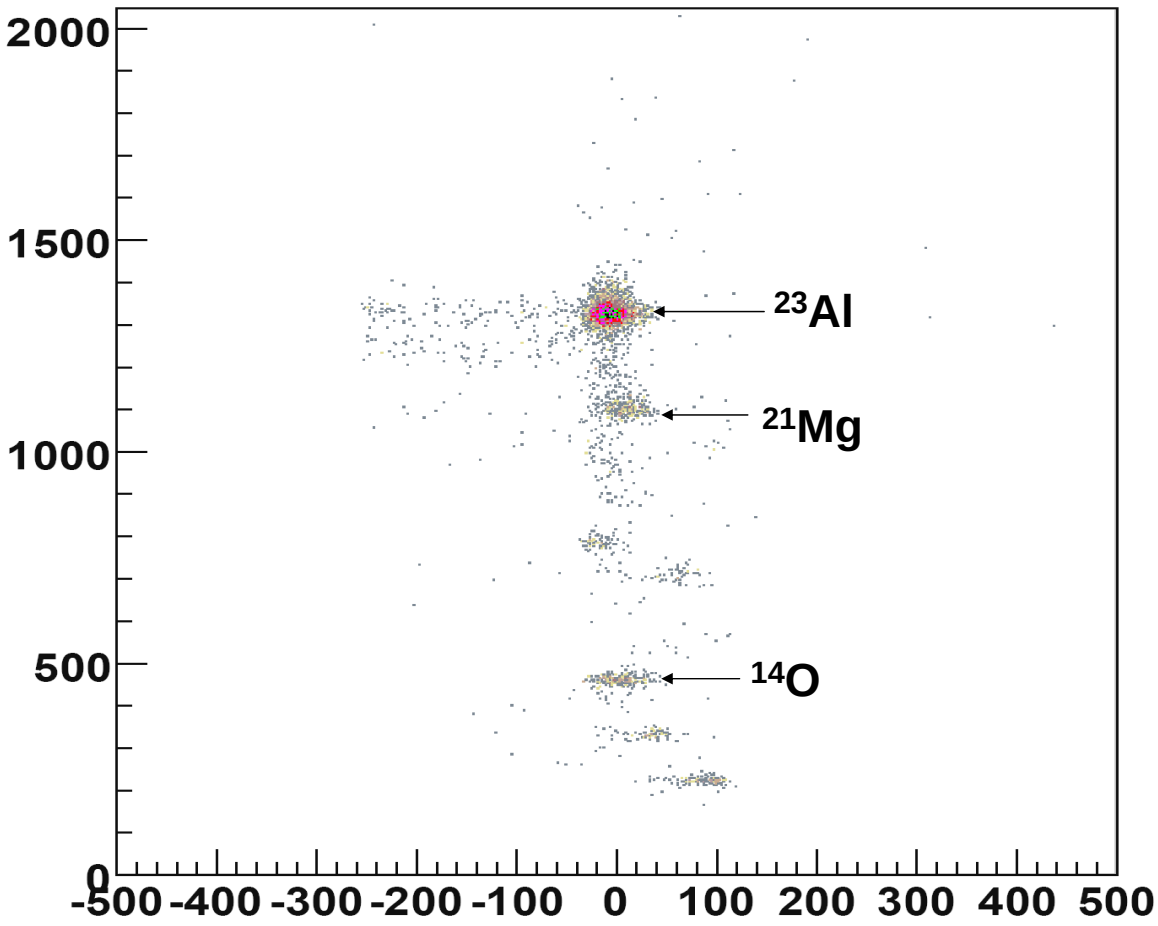

Fig. 16. △E vs Y position for ^{23}Al. Slit settings are listed at Table III. Most impurity nuclei are cut off and only a few reach the MARS focal plane (target detector). The most intense spot is ^{23}Al.

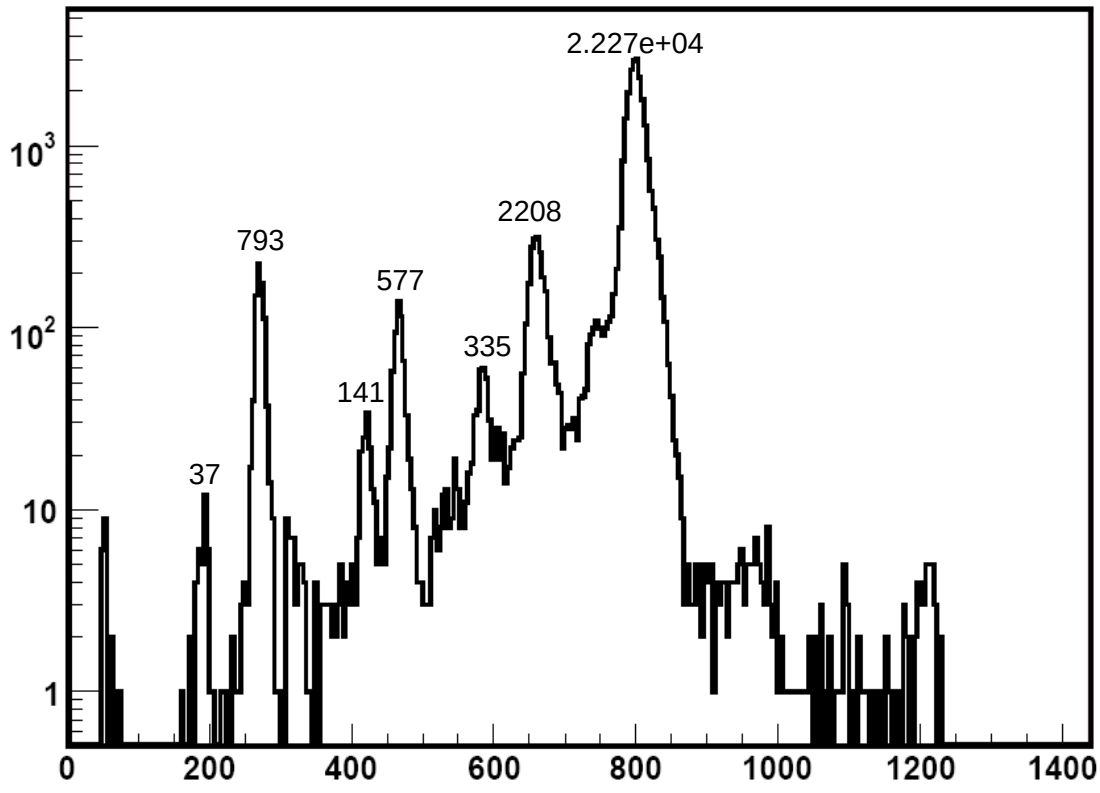

Fig. 17. ^{23}Al production and impurities in the $\triangle$E detector. The ^{23}Al is the strongest peak. Each peak area is marked near the top of the peak.

Table IV. The MARS settings to get pure ^{24}Al radioactive nucleus

Primary beam	$^{24}Mg^{10+}$ at 48 Mev/u
Secondary beam	^{24}Al at 41.8 Mev/u
H_2 gas cell pressure	1.95 atm
BLD1	-570.8 A
Q1	-170 A
Q2	94.6 A
D12	770 A
D1T	22.0 A
Q3	56.6 A
Q4	-73.1 A
Q5	+107.5 A
Bv	740 A
Ev	±137 kV
D3	146.5 A
S2	18.0 A
Slit#1	L/R=open , U/D=open
Slit#2	L/R=±1.50 cm , U/D=open
Slit#3	L/R=±3 cm, U/D=±2.5 cm
Slit#4	L/R=±1.20 cm, Up=0.32 cm, down=-0.26 cm
Bend angle of D3	4°

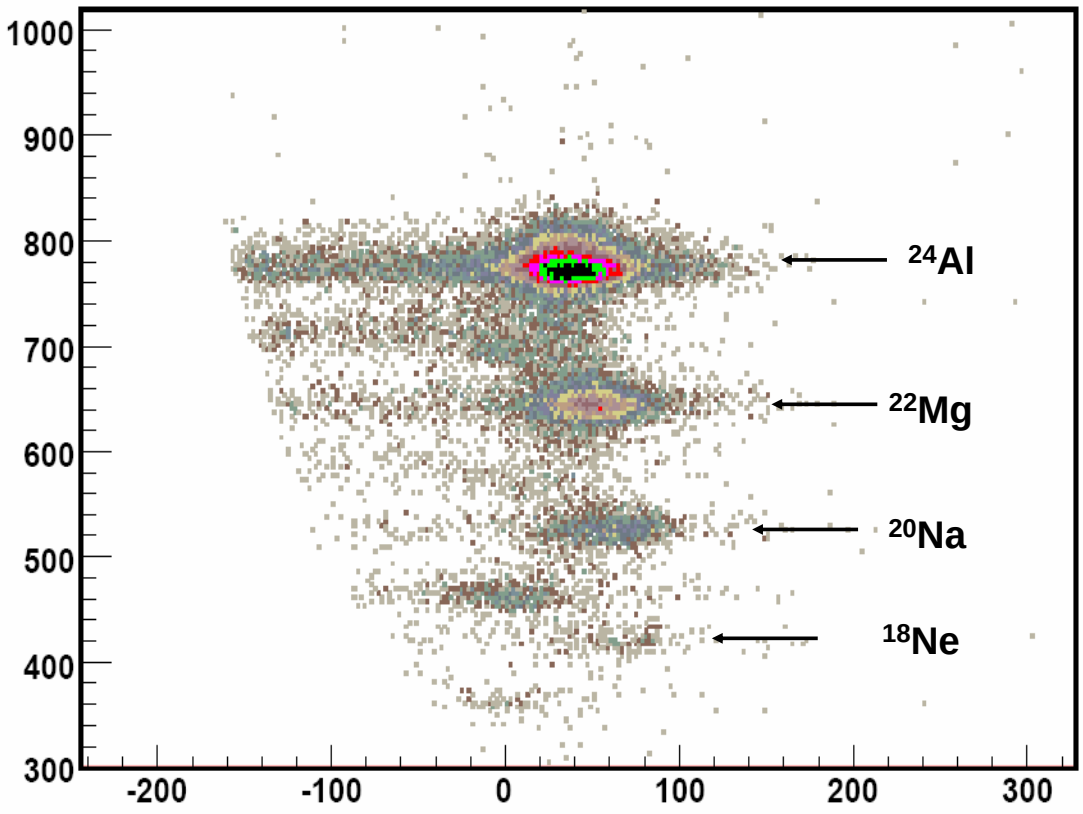

Fig. 18. △E vs Y position for ^{24}Al. Slit settings are listed at Table IV. Most impurity nuclei are cut off and only a few reach the MARS focal plane (target detector). The most intense spot is ^{24}Al.

C. Fast Tape-Transport System

The fast tape-transport system is used to collect radioactive nuclei like ^{23}Al, then deliver them to a detector station for experimental measurement. The experimental setup shown in Fig. 19 is a typical one for measuring β-γ coincidences [60, 51, 64] except that the HPGe detector was closer than usual.

The ^{23}Al beam comes out of the vacuum system by passing through a 50-μm-thick Kapton foil window, a 0.3-mm-thick BC-104 scintillator, a dummy tape and a stack of aluminum degraders (30.5 mils). A 75-μm-thick aluminized Mylar tape on the fast tape-transport system is used to collect ^{23}Al. Because the ranges of impurities in the beam are different from that of ^{23}Al, most impurities will pass through the aluminized Mylar tape. The thickness of Al degraders is empirically chosen to optimize the retention of ^{23}Al in the tape. Then a pure ^{23}Al sample will be collected on the aluminized Mylar tape. In our measurement, we collected ^{23}Al on the tape for about 1 second. Then we shifted the RF phase of one of the cyclotron dees to stop the ^{24}Mg beam. Following this we moved the ^{23}Al sample in approximately 180 ms with the tape transport system to a counting station 90 cm away which consists of a HPGe γ detector and a scintillator β detector. β singles and β-γ coincidence data were recorded for a predetermined counting period of 3.2 seconds in Run0905 and Run0906 and 2.0 seconds in Run1106, respectively. The cycle is precisely clock-controlled and is repeated continuously. The sample is positioned between the HPGe γ-ray detector and a 1-mm-thick BC404 plastic scintillator used to detect β particles. The BC404 plastic scintillator β detector is located 3 mm from the sample, while the HPGe is about 4.9 cm away. Time-tagged coincidence data was stored event by event in the computer.

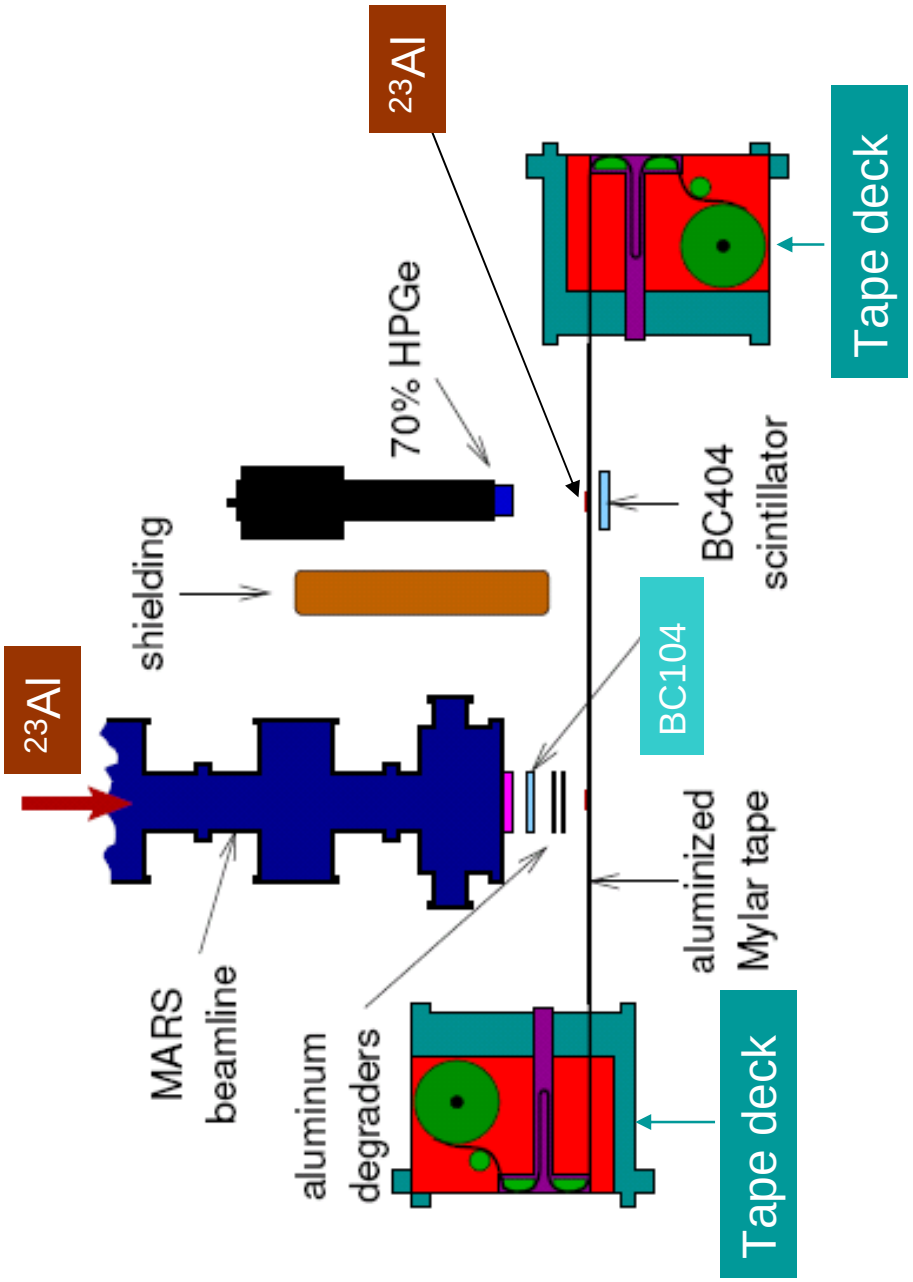

Fig. 19. The layout of fast tape-transport system.

D. HPGe, Scintillator and BGO Detectors System

The measurement itself was done with the beam from the cyclotron pulsed by the same system that controlled the tape-transport system. β singles were counted in a scaler, while β-γ coincidences were recorded event-by-event and stored on disk for off-line analysis. The data recorded for each coincident event included the energy of both detector signals, the time between them, and the time elapsed since the start of the counting period. More details for each detector are given below.

1. HPGe γ Detector

In the three runs we had, two high purity Germanium gamma-ray (GMX HPGe) detectors were used, one in each of the experiments, with other detectors. The HPGe detector with a well calibrated absolute efficiency (0.2% accuracy from 50 to 1400 keV) is called No.2 HPGe detector. Another HPGe with absolute efficiency determined less accurately is called No.3. In Fig. 20, the HPGe γ detector and the β detector used to measure β-γ coincidences are shown.

HPGe detectors are usually operated as fully depleted detectors under a working temperature of 77 K [65]. They can be allowed to warm to room temperature between uses. Energy resolution figures for HPGe detectors are normally specified at 5.9 keV (^{55}Fe), 122 keV (^{57}Co), 662 keV (^{137}Cs), or 1333 keV (^{60}Co). Representative FWHM values for commercially available systems with a small planar germanium detector are about 150-250 eV at 5.9 keV, increasing to 400-600 eV at 122 keV. For larger coaxial detectors, FWHM values are around 800-1200 eV at 122 keV, increasing to 1.7-2.3 keV at 1333 keV. Our HPGe No.2 is a GMX coaxial 280-cm^3 n-type 70% γ detector. It has energy resolution (FWHM) of 2.10 keV at 1333 keV (^{60}Co) and 800 eV at 5.9 keV (^{55}Fe). The detector was carefully calibrated for efficiency with relative and

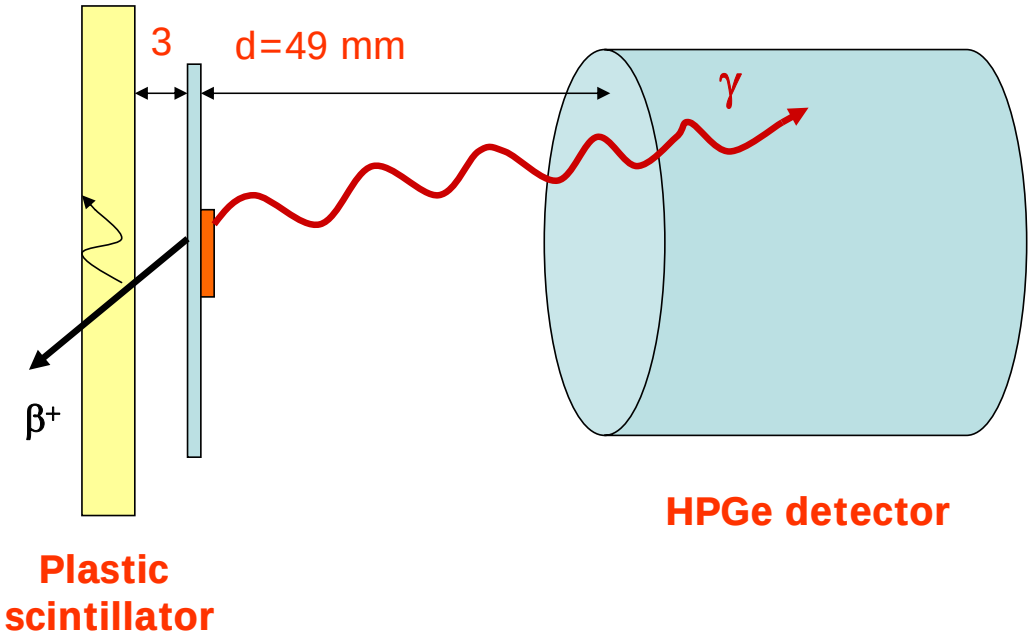

Fig. 20. The Scheme of β and γ detectors used to measure ^{23}Al decay.

absolute efficiency measurements combined with Monte Carlo calculations to meet the requirements in measuring precise β-branching ratios for superallowed decays. The absolute efficiency of HPGe γ-ray detector No.2 is known to 0.2% accuracy from 50 to 1400 keV and 0.4% accuracy for energies up to 3500 keV [66, 67, 68] when at d=15 cm from source. This detector was used in the runs of September 2005 and September 2006, and was positioned at d=4.9 cm from the tape.

During the experiment, we measured β-γ coincidences for ^{24}Al and ^{23}Al. The ^{24}Al β decay scheme is very well studied. It was used to do energy and efficiency calibrations of our detector system to high energies. Measurements of the ^{24}Al were made at d=4.9 cm and 15 cm.

HPGe No.3 was used to measure β-γ coincidences for ^{23}Al with a BGO shield in November 2006. The efficiency of this HPGe detector was calibrated to 1%. HPGe No.3, a coaxial 280-cm^3 n-type 70% γ detector, has similar parameters as above. Background in the high energy region of γ spectrum was reduced substantially. More details will be given in Chapter IV.

2. Scintillator Detector

The plastic scintillator detector is one of the most widely used detector types. The scintillator detector has many advantages, such as high efficiency, small energy loss of transmitted particles, fast time response, little sensitivity to radiation damage, and low cost. These properties allow the plastic scintillator to play a unique role in the field of radiation detectors [69, 70, 71, 72].

Heavy ions like ^{23}Al could easily pass through plastic scintillator foils without losing much energy. In our experiments, a 0.3-mm-thin disk of the BC-104 plastic scintillator was used as heavy-ion detector (transmission detector) and a 1 mm thick disk of the BC-404 plastic scintillator was used as β detector. The heavy ion ^{23}Al

events and the β singles were counted in the scalers. Figure 20 shows the 1-mm-thick BC-404 plastic scintillator β detector used in the experiment. It was positioned 3 mm away from the aluminized Mylar tape, and on the opposite side of the HPGe detector. The light induced by the positrons passing through the plastic scintillator was detected and amplified by a photomultiplier tube (PMT).

3. BGO Detector

In order to reduce the background in the high energy region of the spectrum, we added a Bismuth Germanate ($Bi_4Ge_3O_{12}$, BGO) Compton shield detector to the HPGe γ detector. The setup is shown in Fig. 21.

The BGO Compton shield was fully tested [73]. This is the first time it is used in an in-beam experiment. The β-coincident γ-spectrum with BGO veto will be discussed in the next chapter.

The BGO shield is made from crystals produced and put together by BICRON, and from crystals made initially for the GAMMASPHERE project [74]. The whole geometry design is that of the GAMMASPHERE shields. We designed the light collection solution and the attached electronics at Texas A&M University. We also designed the passive shield for the BGO to work with.

The general idea behind the operation of a Compton shield is that it wraps around a HPGe detector and detects with high efficiency secondary γ-rays that scatter out of the HPGe detector. Any signal from a γ-ray that is Compton scattered in the HPGe detector, rather than fully absorbed, will be rejected by an anticoincidence setup with signals in the Compton shield. Therefore, the detection efficiency of the Compton shield is important. Care must be taken to increase the detection efficiency of the Compton shield, to minimize the detection threshold in it (light collection and electronics), and to avoid being triggered by truly coincident gamma rays coming

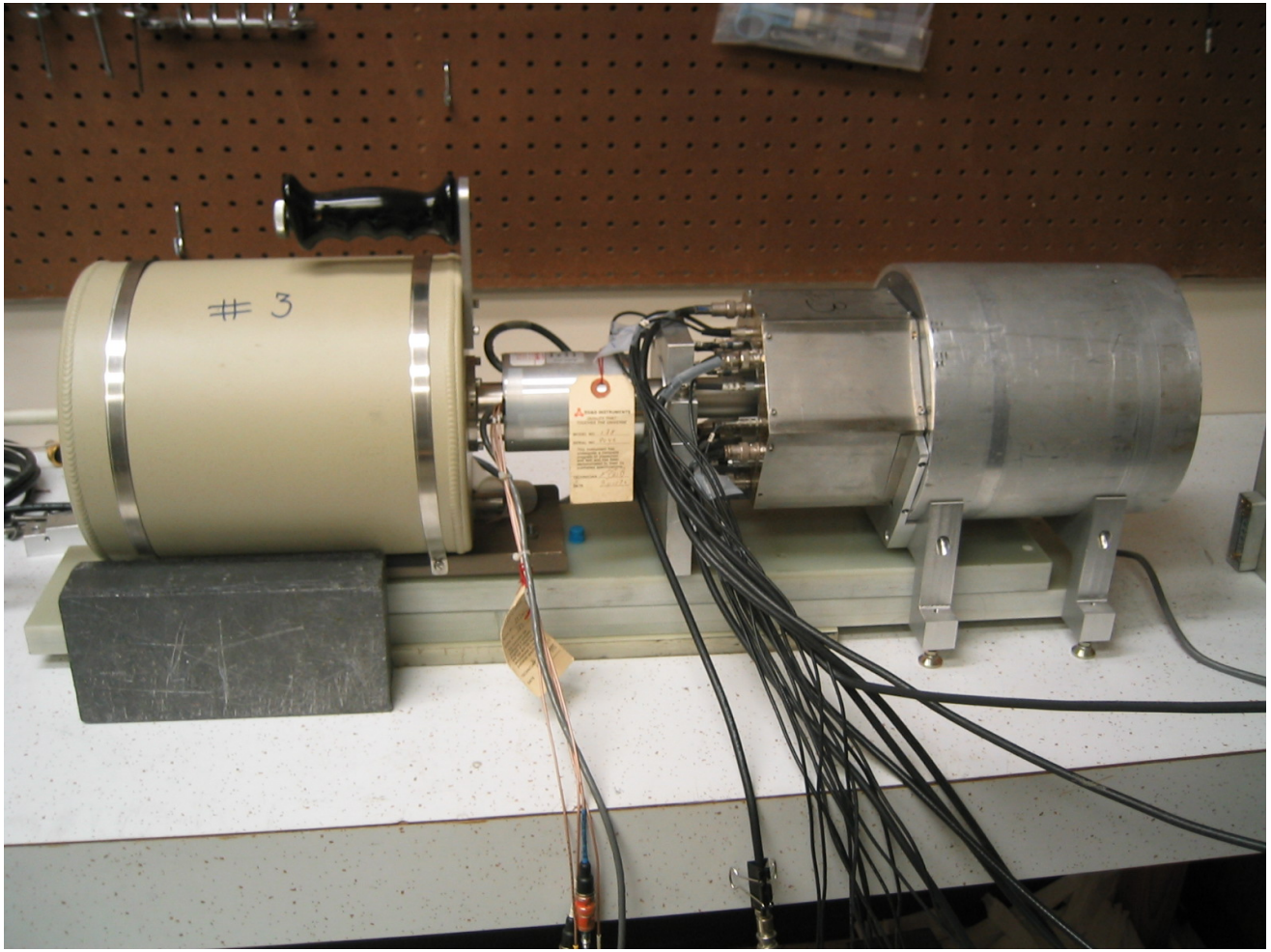

Fig. 21. The HPGe γ detector is inside the BGO Compton shield. This is the offline mount which is very close to the online setup.

directly from the source (by passive shielding).

The BGO Compton shield consists of 6 optically independent crystals. Each crystal has 2 Hamamatsu R1924 photomultiplier tubes which are in good optical contact on it. The tube bases are made in our lab, adapted after the Hamamatsu E2924-05 sockets. In the BGO Compton shield, both tubes on the same crystal have the same bias connector which applies negative voltage from a Fluke 412B source. The negative biased working voltage is between -1000 and -1200 V. The voltage applied can be slightly different on each tube and should be chosen so that the final gain is the same for each tube.

The signals are collected separately for each tube with the 12 Lemo connectors. The PMT signals are introduced in the Summing Amplifiers (SA) designed and built in the Cyclotron Institute of Texas A&M University. In details, each of the two signals from the PMT's seeing the same crystal is fed into the inputs of one channel of the Summing Amplifier. The summation of all 6 channels can be directly plugged into a Constant Fraction Discrimination (CFD), with the threshold adjustable at the desired value above the noise level. This signal gates, in anticoincidence, the energy signal from the HPGe detector inside the BGO shield. A standard scheme may be used: the delayed BGO CFD signal is put in a fast-slow coincidence scheme with the HPGe signals. A more elaborate scheme would take the amplitude of the BGO signal and the BGO-Ge timing signals and put them into an event-mode list for further off-line processing.

A source of ^{57}Co (122 keV γ line) was used to determine that the noise level of the BGO Compton shield which is less than 35 keV. The overall resolution found was around 150 keV for the 662 keV γ line in the BGO crystal. The linearity of the BGO's is good from about 100 to 2000 keV gamma rays.

The efficiency of the BGO Compton suppression in the HPGe γ detector is

determined as follows. The HPGe detector was inserted in the BGO Compton shield. The BGO shield itself is fixed into a lead shield, adjusted for the working height of the HPGe detectors, and designed to fit on the table built for use with the 70% HPGe detectors. On the front face of this lead-in-aluminum case shield there are two tungsten pieces, one plugged inside from behind, and one mounted with a set of screws on its face. These are the pieces that shield the BGO crystal from seeing the source directly. It was designed for a source 1 cm across, situated at about 4 cm in front of the face of the BGO crystal, and 11 cm in front of the HPGe crystal (not 25 cm as in the GAMMASPHERE design). The whole system is heavy (the Pb shield wrapping the BGO shield) and must be well aligned and remain stable before assembling it. With both ^{137}Cs and ^{57}Co sources at the very entrance of the BGO Compton shield, we found a reasonable Compton suppression for the 661.7 keV photopeak of the ^{137}Cs source in the HPGe detector. Measuring the HPGe spectrum with the shield inactive, then in anticoincidence with it, the continuum between 140 and 650 keV was reduced from 100k counts to about 26k counts (for an equal acquisition time of 236 seconds), that is 74% reduction, or a 3.85 reduction factor, while the photo peak was reduced only about 1.2%. The CFD threshold was set to be -290 mV, equivalent to about 37 keV. In the present geometry, the sources gave a large counting rate in the BGO detector. It is difficult to distinguish the signals very well from the system's noise. Therefore, we expect that we can set the threshold even lower, and get a better suppression factor. In the real measurements the BGO crystal should not see directly the primary gamma-ray source. The HPGe-BGO coincidence realized was optimized either: measured on a Timing-Amplitute-Convertor (TAC) it had a 28 ns FWHM, and it was the random coincidences that lead to the 1.2% rejection of good photopeak events in the HPGe detector reported above. The peak-to-total (P/T) parameter was changed from cca. P/T=0.27 with inactive BGO Compton shield to cca. P/T=0.47

with the active BGO Compton shield. If we neglected the lowest energy part up to 140 keV in the HPGe detector, and then the same parameters would read: P/T=0.34 becomes P/T=0.68.

In conclusion, the BGO Compton shield works the way they should: the crystals give good light response, the optical coupling crystal-phototubes is very good and the electronics to process the signals is appropriate and without additional noise. The peak-to-total ratio obtained is close to 0.5 at the 662 keV line of ^{137}Cs and an average of P/T=0.43 for the 1.17 and 1.33 MeV lines of ^{60}Co. One cannot get better results than this without the active plug at the back of the BGO shield (not available for our geometry).

E. Signal Processing and Data Acquisition System

The data acquisition circuits (DAC) are illustrated in Fig. 22. This DAC system was developed at the Cyclotron Institute of Texas A&M University [75]. It is a multi-parametric data acquisition system based on the KmaxNT software and CAMAC modules with FERA readout. The hardware of the DAC system includes analog-to-digital converters (ADC, QDC, TDC, and latching scalers), a FERA driver, two dual port FERA/CAMAC buffer memories, a controller with SCSI capability and a PC working in the WindowsNT operating system.

The experiment is designed to work in cycles. The basic principle is illustrated in Fig. 23. We started by implanting the radioactive beam in the tape. In the ^{23}Al experiment, this was done for a time interval of t_{beam} = 1 second. Then the beam was turned off and the collected activity was moved in the center of the counting station, situated about 90 cm away from the implantation position, where we then measured the β–decay for ^{23}Al. The location of the counting station was well shielded

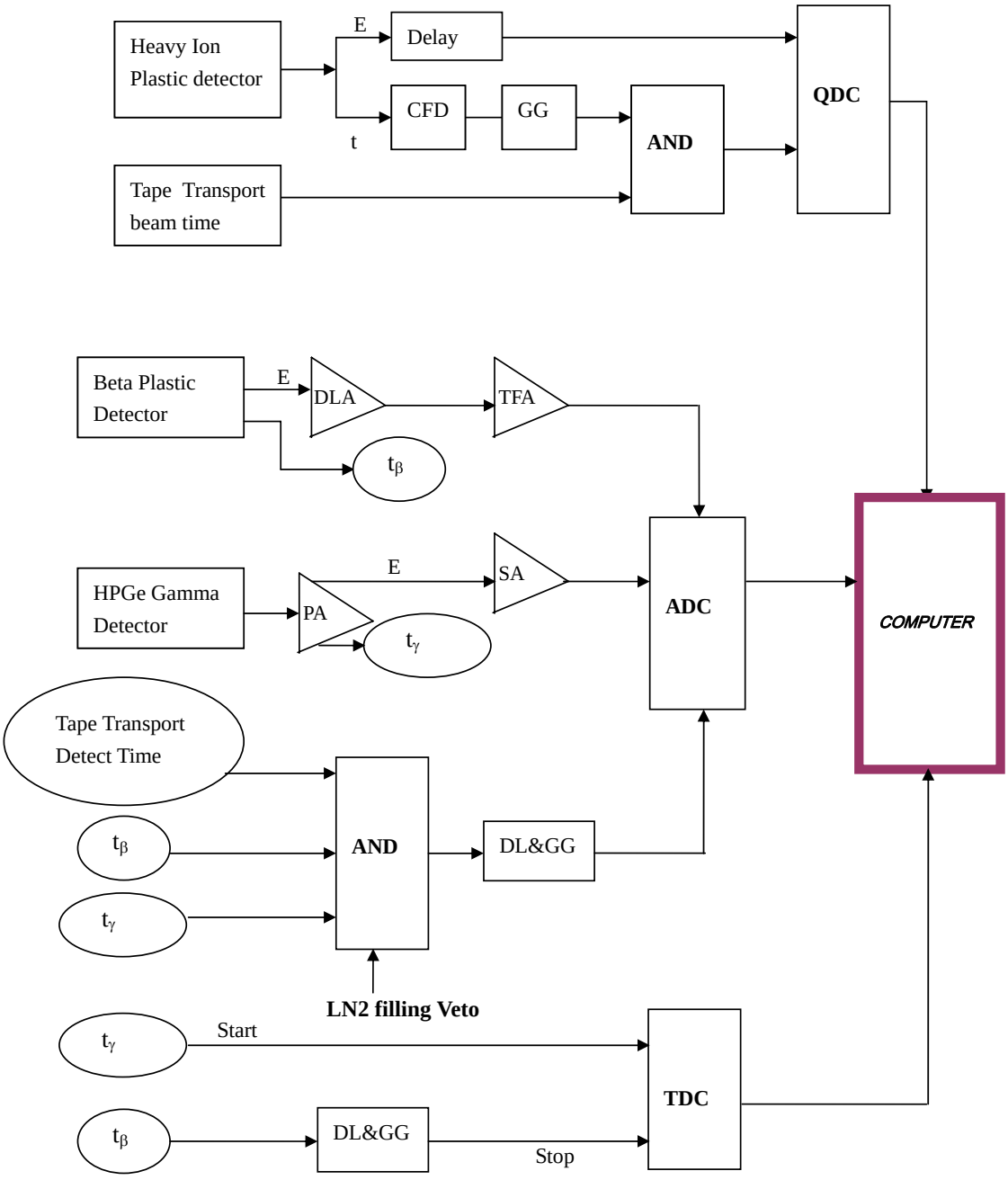

Fig. 22. The Schematic drawing of the Data Acquisition System.

to minimize the background interferences generated by the beam line. The counting station consisted of a 1.0-mm-thick disk of the plastic scintillator and a high volume HPGe detector (70%) (see Fig. 19 and Fig. 20). Using these two detectors, we collected off-beam β-γ coincidences and β singles for 3.2 seconds. Such (Beam on)-(Beam off Move)-(Detect) cycles were repeated until sufficient statistics had been accumulated. β-γ coincidences were recorded event by event. The full β-γ coincidence event contains the following information (E_γ, $\triangle E_\beta$, $t_{\beta-\gamma}$, t_{cycle}), where E_γ is the energy deposited in HPGe detector, $\triangle E_\beta$ is the energy deposited in the plastic scintillator, $t_{\beta-\gamma}$ is the time interval between the HPGe and plastic signals, and t_{cycle} is the time elapsed since the beginning of the cycle.

The measurement cycling was controlled by the tape-transport system which issues $beam(on/off)$ signal, *move* signal and *detect* signal. The $beam(on/off)$ signal is used as the beam pulsing as well. More details about signal flow from the detectors to the computer is discussed below.

First, when the beam was on, the ^{23}Al heavy ions passed through the 0.3-mm-thick plastic scintillator. The output signal from the PMT was split into two signals and was further proceeded as energy, $\triangle E$, and timing signals, t (see Fig. 22). Thus we measured the $\triangle E$ spectrum of the heavy ions in the plastic scintillator and scaled the number of heavy ions passing through. Besides that, we recorded the time stamp of the implantation, which allowed us to extract the beam time profile. The relevant information acquired during the beam-on was: $\triangle E_{HI}$ and t_{cycle}. We adjusted the aluminum degraders' thickness to ensure that the ^{23}Al was implanted in the center of the aluminized Mylar tape. This is shown in Fig. 24. The $\triangle E_{HI}$ was generated by the Charge-to-Digital Converter (QDC). It required a well defined charge integration window that should be as narrow as possible to minimize the integration over the background. This was achieved with a gate generator set in coincidence with the

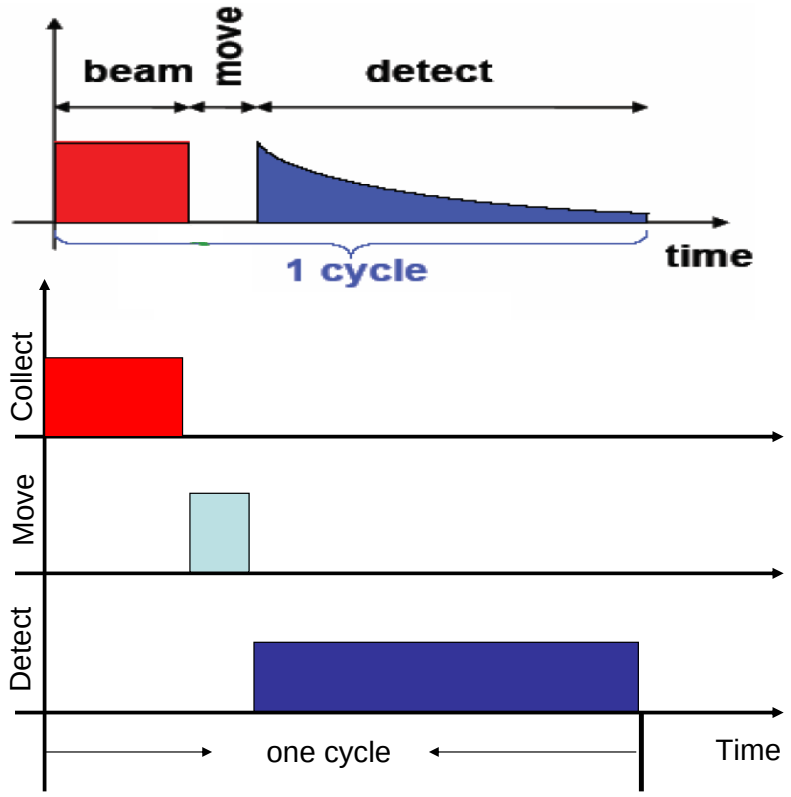

Fig. 23. Shown here is the collect-move-detect cycle for the ^{23}Al β-γ coincidences. In our measurement, we collected ^{23}Al on the tape for 1 second. Then we shifted the RF phase of one of the cyclotron dees to stop the ^{24}Mg beam. After these we moved the ^{23}Al sample in approximately 180 ms with the tape transport system to the counting station 90 cm away which consists of the HPGe γ detector and the scintillator β detector. The β singles and the β-γ coincidence data were recorded for a predetermined counting period of 3.2 seconds.

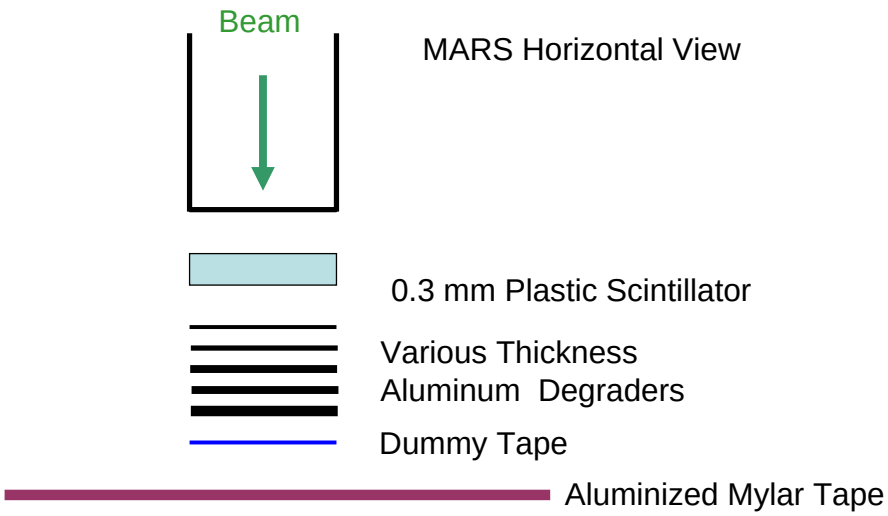

Fig. 24. The aluminum degraders' thickness was adjusted to ensure the ^{23}Al to be implanted in the center of the aluminized Mylar tape. Dummy tape is a small piece of aluminized Mylar tape.

beam − on signal issued by the tape-transport system (see the top part of Fig. 22).

Second, we turned off the beam after 1 second collecting time. The collected ^{23}Al samples were moved to the center of the counting station. The decay would be detected for a *detect-time* of 3.2 seconds. With this way, we measured the off-beam β-γ coincidences, β singles and β-γ timing (start by t_γ, stop by t_β delayed $\sim$1.4μs.). This process is shown in Fig. 22 and will be explained below.

The plastic scintillator β detector gave two signals, energy E_β and timing t_β. E_β first passed through a Delay Line Amplifier (DLA), and then went to a Timing Filter Amplifier (TFA). The output signal was sent to an Analog-to-Digital (ADC) module.

The Signals from the built-in Pre-Amplifier (PA) of the HPGe γ detector, energy E_γ and timing t_γ, were sent to different modules. E_γ was sent to a Spectroscopy Amplifier (SA), and then the output signal was sent to an ADC.

The coincidence was defined by the *AND* circuit that checks for the simultaneous presence of the t_β and t_γ signals (through properly delayed and adjusted gate signals)

with the additional request that the *detect* signal issued by the tape-transport system was present (see the lower part of Fig. 22).

The β-γ coincidence time was measured by the Time-to-Digital Converter (TDC). The start timing was issued by t_γ while the stop timing was issued by a corresponding delayed t_β. This arrangement ensured the lowest triggering rate in the TDC while the efficiency in the HPGe γ detector was significantly lower than that of the plastic scintillator since both the geometry and relative efficiency were higher for the plastic scintillator (All β particles hitting the plastic scintillator will generate a signal, meanwhile not all γ-rays reaching the HPGe γ detector will do the same, and the plastic scintillator is much closer to the tape than the HPGe γ detector).

In summary, the DAC system had three major signal processing parts.

Beam-on and collect : measure events($\triangle E_{HI}$, $Number_{HI}$, Beam time t_{beam}) for 1 second. The t_{beam} is an important parameter that is recorded by a FERA latching scaler which counts the clock-pulser by a very precise ($\sim 10^{-6}$ seconds) pulser synthesizer.

Move: Move ^{23}Al to the counting station in 0.18 second. No data acquisition.

Beam-off and detect: measure events(E_γ, E_β, $t_{\beta-\gamma}$, t_{cycle}) and β singles for 3.2 seconds.

This cycle was repeated until sufficient statistics had been accumulated.

CHAPTER IV

DATA ANALYSIS AND RESULTS

All experimental data were first carefully analyzed and cleaned with computer programs related to the KMaxNT analysis system. Further, the resulting γ spectra were analyzed using the software package Radware [76] in Linux environment. Radware is a software package for interactive graphical analysis of gamma-ray coincidence data. It was developed by David Radford of the Physics Division at Oak Ridge National Laboratory [77]. The data analysis procedures and results are detailed below.

A. Energy and Efficiency Calibration of the HPGe Detector

Our method for the determination of absolute branching ratios and absolute $\log ft$ values from β and $\beta-\gamma$ coincidence data of ^{23}Al implies a good knowledge of absolute efficiency of the HPGe γ detector. As said before, the absolute efficiency for this detector is known very well for E_γ <3.5 MeV and the distance to source d=15 cm. The efficiency was not known at all at larger γ–energies, and we chose ^{24}Al, with γ–rays up to 7.07 MeV and a relatively well known decay scheme, to extend the energy and the efficiency calibration for E_γ >3.5 MeV. This was an important step needed in the analysis of data for the β–decay of ^{23}Al.

As we mentioned in Chapter III, we produced a radioactive beam of ^{24}Al using the same 48 MeV/A $^{24}Mg^{10+}$ beam from the Texas A&M K500 superconductivity cyclotron to initiate the ^{1}H(^{24}Mg,^{24}Al)n reaction on a LN_2-cooled hydrogen gas target. The ejectiles entered the MARS spectrometer where the beam was stopped and the fully stripped reaction products were spatially separated from one another, leaving a $\sim$ 80% pure ^{24}Al beam at the extraction slits in the MARS focal plane (^{24}Al beam purity can be higher by setting slits to cut more beam while the ^{24}Al beam intensity

decreases). The quality of the ^{24}Al production data is shown in Figs. 25 and 26. This beam exited the vacuum system through a 50-μm-thick Kapton window, passed successively through a 0.3-mm-thick BC-104 scintillator and a stack of aluminum degraders, and finally stopped in the 75-μm-thick aluminized Mylar tape of the tape-transport system. Since the impurities remaining in the beam had different ranges from ^{24}Al, most were not collected on the tape. Residual collected impurities were found to be substantially less than 0.1% of the ^{24}Al content. The maximum intensity of ^{24}Al was 2x10^5 ions per second at a beam current of 110 nA. This rate was too large for our detectors and was reduced by beam attenuation with different amounts (a factor of 3 for the 150 mm measurement and a factor of 10 for the 49 mm measurement respectively. ie. around 2x10^4 ions per seconds) at the 2 distances we have measured: 49 mm (also for ^{23}Al) and 151 mm (standard distance for the efficiency calibration).

In the β-γ coincidence measurement, we collected ^{24}Al on the tape for 4.0 s, then interrupted the accelerator beam in a few μs by shifting off the resonance phase of one of the cyclotron dees, and triggered the tape-transport system to move the sample in 175 ms to a shielded counting station located 90 cm away. There, data were recorded for a predetermined counting period while the beam remained off. This cycle was clock controlled and was repeated continuously. For the β-γ coincidence measurement, each counting period was 4.0 s, during which the sample was positioned between the HPGe γ–ray detector and the 1-mm-thick BC404 plastic scintillator that was used to detect positron particles. The former was located 4.9 cm from the sample, while the latter was 3 mm away. Time-tagged coincidence (or singles) data were stored event by event. A second measurement was made with the HPGe detector at d=15 cm, the distance for which its efficiency was well known for E_γ <3.5 MeV [66, 67, 68]. The β-coincident γ-ray spectrum for ^{24}Al is shown in Fig. 26.

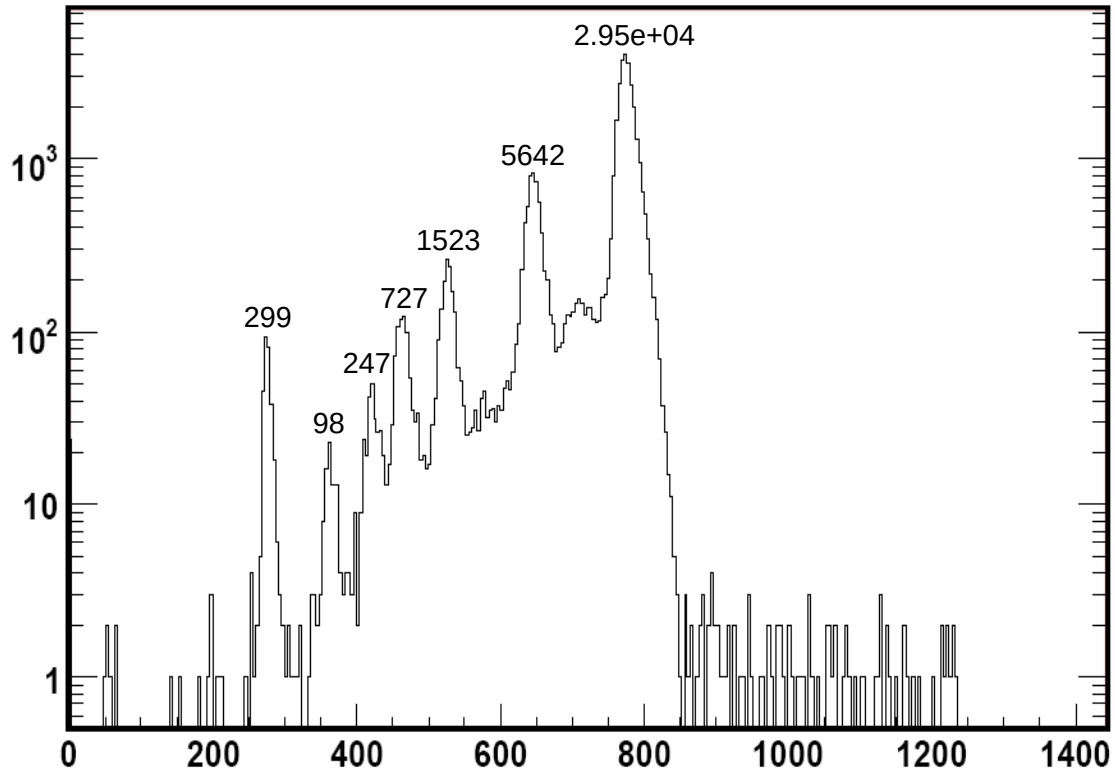

Fig. 25. ^{24}Al production and impurities in the $\triangle$E detector. The ^{24}Al is the strongest peak. Each peak area is marked near the top of the peak.

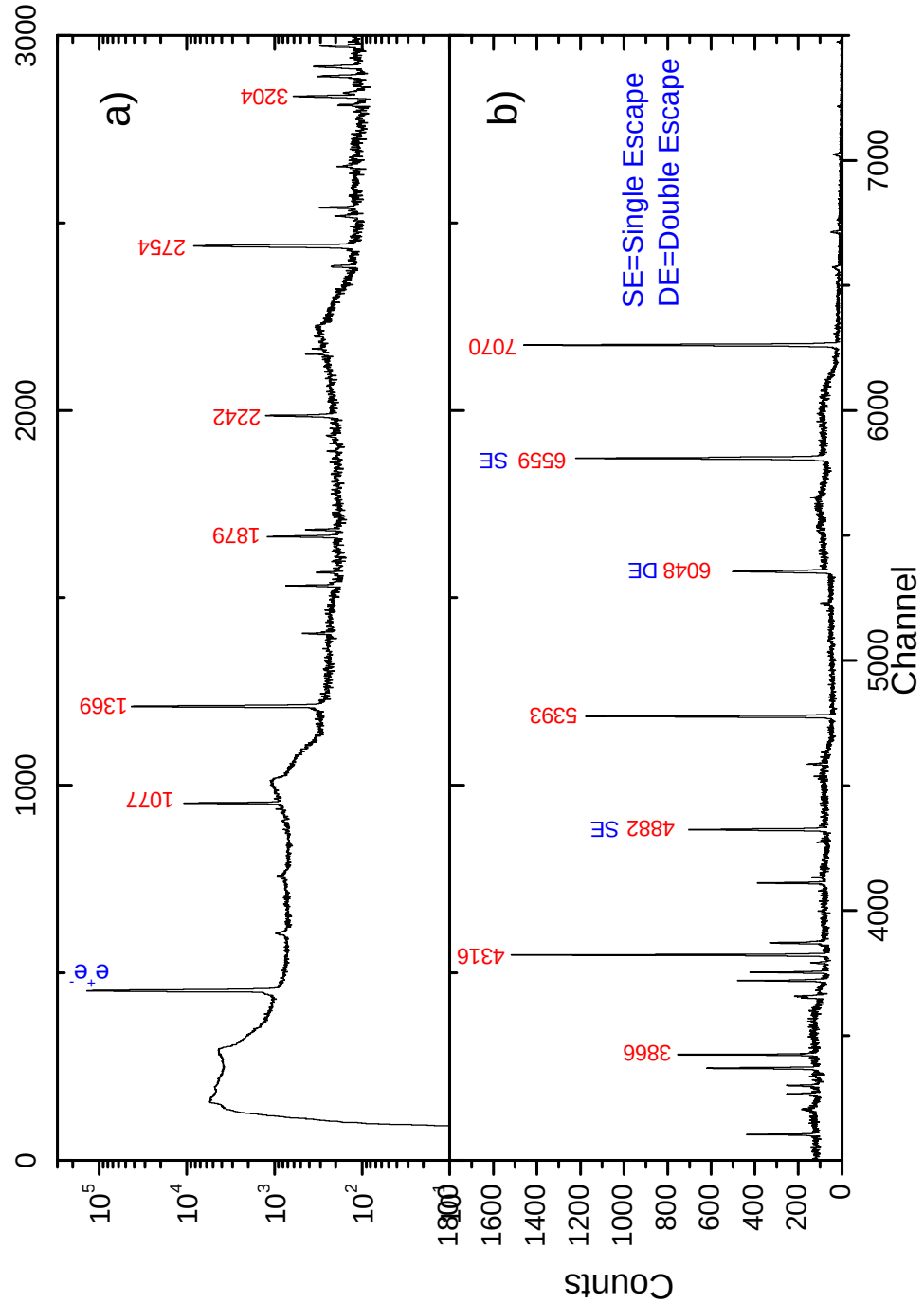

Fig. 26. The β-coincident γ-ray spectrum for ^{24}Al (Run0906). The ^{24}Al decay major γ transitions (can be found in next figure, ^{24}Al decay scheme) are labeled with red numbers in keV units. The SE and DE mean single escape and double escape γ–rays. Some of the unlabeled peaks are the weak SE and DE peaks. Some of the unlabeled peaks are the weak γ transitions of ^{24}Al.

1. Energy Calibration

Energy calibration of the HPGe γ detector is straightforward. There is no difference to do energy calibration between the experiments without BGO and the experiments with BGO. From Fig. 26, we select the well studied γ peaks with high intensity from low energy to high energy range. Then those γ peaks were precisely positioned in channel number and integrated for the position and the net peak areas by subtracting their background. Here the γ-analysis software package Radware is used to do γ peaks fitting. The γ peak areas are extracted from Gaussian fitting by tuning various parameters and subtracting the background carefully. It works very well for γ-spectra obtained in the the experiments with and without BGO. It is important to fit γ peaks properly to get precise peak positions and net peak areas which are needed in the further data analysis. The more details about fitting procedure will be discussed in the following subsection 4.1.a [78].

a. Fitting Procedure

The background settings play a big role during the fitting. Peak areas are obtained by integration that includes a background. The error associated with the Gaussian fit is taken as the error for the fitted area. It is important to physically explain the fit region first, and then proceed to fit using the tools and ingredients that the fitting program Radware offers. Usually, the X-ray sum peaks show up at the right side of peaks and some bump shapes from insufficient charge collection and Ge escape X-ray peaks show up on the left side of the peaks. The fitting procedure is explained below step by step.

Step I, before fitting, the γ spectrum can be roughly calibrated by a two point linear energy calibration. Then using the peak find command of Radware, the energies

of the main γ peaks are marked on the displayed spectrum.

Step II is to setup a fit window. The fit window is for us to see the details of the background and lower part of the peak. An example is given in Fig. 27. In the horizontal direction, a 200 channel window is normal. However by changing the size of horizontal window, taking larger windows, it is possible to see if the background is linear or curved, tilted or horizontal, etc. After understanding the background, I come back to the 200-channel window.

Step III is to setup the fit region. The fit region is usually taken to be 20 times the FWHM of the peak in channels. For example, if a peak has a FWHM=4 channel, then an 80 channel fit region will be taken on each side of the peak. Close lying peaks or somehow sudden modifications in the shape of the background may not allow such limits, so the fit regions could be shorter depending on practical situations.

Step IV is the background determination. The fit result depends mostly on the background settings. Fig. 28 shows a bad definition of a background level. The Radware program uses for background a second order polynomial function, A+B*ch+C*ch^2. One can see that the background level is higher on the left side than on the right side of the peak. Also this peak has a bump or a tail on the left side. Both of these are detection effects and must be taken explicitly into account by the program. However, the default fit command is not suitable for that. It takes a parabola shape background and finds the particular parabola that equalizes the areas under and above it (except for the Gaussian peak area).

Generally the initial γ–ray gives the HPGe detector a fraction of its energy in several steps. Eventually it may leave the detector or may be absorbed. Each time a γ–ray is totally absorbed in the detector it produces a count in the photo-peak. If not, depending on how much energy was deposited in detector, one count may be recorded anywhere between zero and the initial energy of the γ–ray. These counts

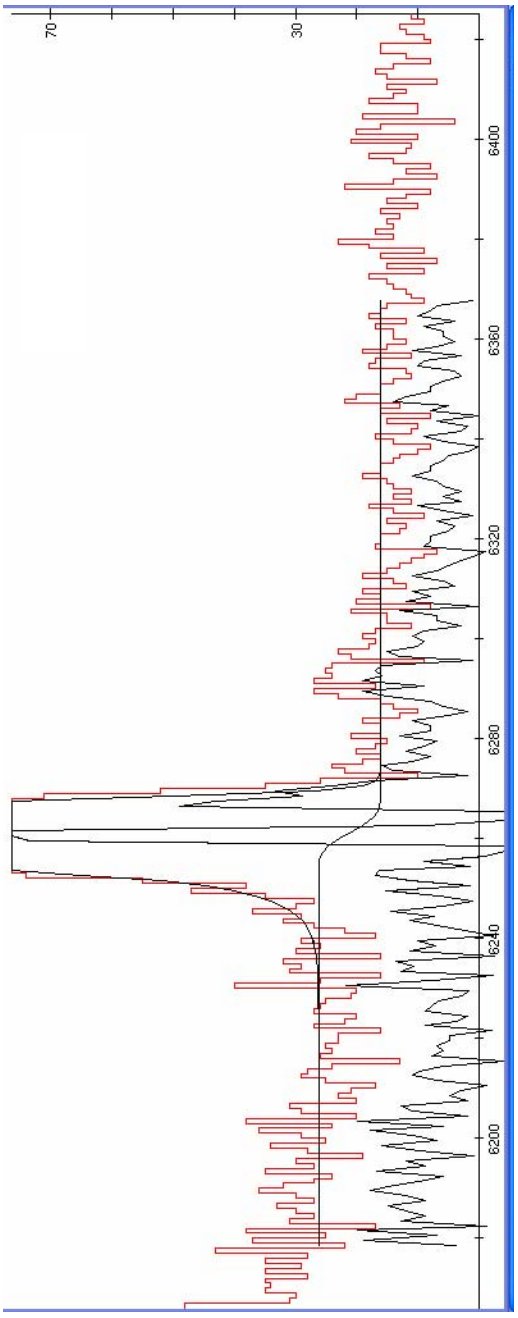

Fig. 27. Fit window display.

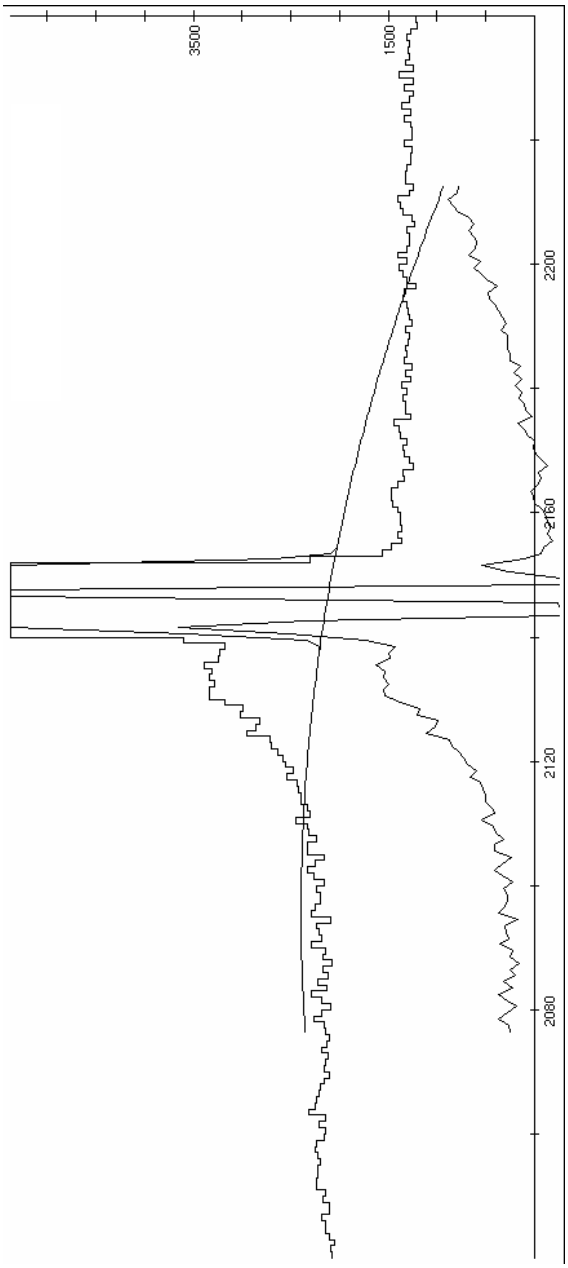

Fig. 28. Background setting display (Example of bad definition).

will thus be recorded on the left side of the photo-peak, producing higher background than on its right side. The Radware program has a built-in step function to take into account the above effect. By adjusting step function parameters, a proper step background can be obtained. Figure 27 shows a good step background setting.

Sometimes, there are some small tails on the right side of the peaks. Each γ–ray is recorded in some period of time, and only after this time the detector and electronics are able to deal with next γ–ray in a correct manner. If the next γ–ray hits the detector within this time, a pile-up happens, which means a part of the first γ–ray signal is added with the second γ–ray signal and a count of higher energy than the photo-peak is recorded. This generates the right hand side tail of the peak and must be counted with the peak, not with the background: the tail contains real valid counts which were just a bit displaced by the pile-up effect. Pile-up was important for the higher rate data.

Step V is to fit the peaks. The general goal of a fit is to minimize the ratio of ChiSquare over Degrees Of Freedom (Chisq/d.o.f) reported with the fitting results. However it is far more important to fit taking into consideration specific physical effects known with γ–ray detection in large volume HPGe detectors and minimize Chisq/d.o.f, than the latter alone.

The procedure essentially consisted in taking a constant background with a step function, and taking some neighboring "background-looking" regions with the photo-peak. The uncertainty that is reported with the determined area is underestimated because many parameters were fixed during the fit. But it is still a good error estimate.

^{24}Al β-decay has been very well studied and a β delayed γ transition scheme established [79, 80, 81, 82], as shown in Fig. 29. We can get γ transition energies from the literature. The plot of γ peak energy vs peak position in channel number is shown in Fig. 30 and fit with a third degree polynomial. The good quality of the

energy calibration is also shown in Fig. 30 (right panel). The error bar shown in Fig. 30 (right panel) is the full uncertainty including the peak fitting uncertainties and the uncertainties of γ transitions populated from the ^{24}Al excitation energy states. The energy calibration is used to calibrate the γ-spectrum from β-γ coincidences for ^{23}Al. This energy calibration results in an uncertainty in the energy of larger than 0.3 keV when it is applied to ^{23}Al γ–ray spectrum.

2. Efficiency Calibration

The absolute efficiency of the HPGe γ detector, positioned 15 cm from the collected sample, has been meticulously calibrated by Hardy, et al. [66, 67, 68], over a 6 year period by measurements with 13 individual sources from ten different radionuclides: ^{48}Cr, ^{60}Co, ^{88}Y, ^{108m}Ag, ^{109}Cd, ^{120m}Sb, ^{133}Ba, ^{134}Cs, ^{137}Cs and ^{180m}Hf. Two of the ^{60}Co sources were specially prepared by the Physikalisch-Technische Bundesanstalt [83] with activities certified to 0.06%. The details of the calibration procedures, which include both source measurements and Monte Carlo calculations, have been published [66, 67, 68]. The absolute efficiency of this detector is known to 0.2% in the energy range from 50 to 1400 keV, and 0.4% from 1400 keV to 3.5 MeV. It is probably also correct to 1.0% from 3.5 MeV to 4.8 MeV [68].

The absolute efficiency of the β^+ detector, which was located 3 mm from the collected samples of ^{24}Al and ^{23}Al, is not required for our measurement, but its dependence on energy is of importance. We have explored the efficiency of this detector via measurements with sources–^{90}Sr, ^{133}Ba, ^{137}Cs and ^{207}Bi and Monte Carlo calculations, and its dependence on β^+ energy is now well understood. In our experiments, the absolute efficiency of the β^+ detector is between 0.367 and 0.371 depending on the β^+ end-point energy (3.6 to 11.4 MeV in our case).

The γ–rays observed following the β–decay of ^{23}Al have a wide range of energies

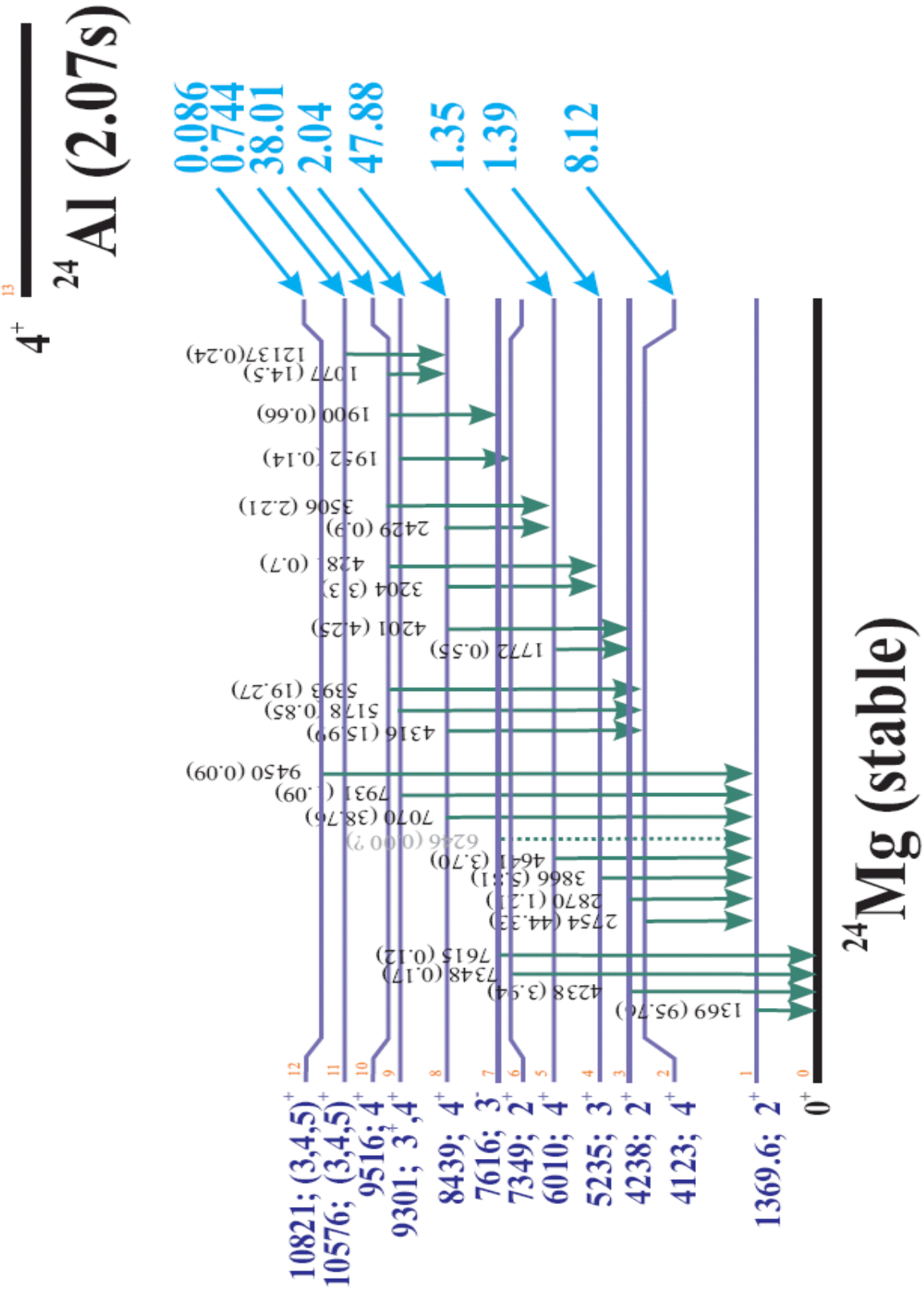

Fig. 29. ^{24}Al β-decay scheme.

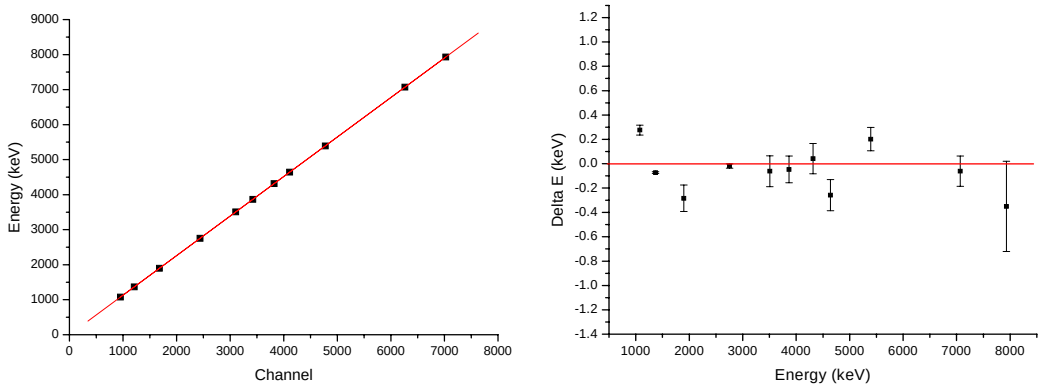

Fig. 30. Shown here are the ^{24}Al energy calibration curve and the quality of the energy calibration as determined by residuals following calibration. The error bars shown in the right panel are the full uncertainties including the peak fitting uncertainties and the uncertainties of γ transitions populated from the ^{24}Al excitation energy states. This energy calibration results in an uncertainty in the energy larger than 0.3 keV when it is applied to the ^{23}Al γ–ray spectrum.

extending up to 8 MeV. We thus required an efficiency calibration of the HPGe γ detector at these high energies, i.e. an extension of the HPGe efficiency up to 8 MeV with real experimental data without the dangers of extrapolation by Monte Carlo simulations only. For this purpose, we used the γ–rays from the known decay of ^{24}Al. From the ^{24}Al decay level scheme in Fig. 29, we can see that there are eight γ transitions feeding the energy level at 1369.6 keV. Since there is no β feeding of the level, the total number of 1369 keV γ–rays must be equal to the sum of all eight γ transitions populating the level at 1369 keV. This can be written as follows

$$\frac{A_{1369}}{\varepsilon_{1369}} = \frac{A_{2754}}{\varepsilon_{2754}} + \frac{A_{2870}}{\varepsilon_{2870}} + \frac{A_{3866}}{\varepsilon_{3866}} + \frac{A_{4641}}{\varepsilon_{4641}} + \frac{A_{6246}}{\varepsilon_{6246}} + \frac{A_{7070}}{\varepsilon_{7070}} + \frac{A_{7931}}{\varepsilon_{7931}} + \frac{A_{9450}}{\varepsilon_{9450}}. \quad (4.1)$$

Where A_{1369} is the peak area of the 1369 keV γ–ray, ε_{1369} is the γ–ray efficiency at the energy 1369 keV, etc. The integrals of the net peak areas of γ–rays after subtracting their background can be obtained from the β-γ coincidence spectrum of ^{24}Al. The γ–ray efficiency below energy 3500 keV is known. The γ–rays at the energies 2870

keV, 6246 keV, 7931 keV and 9450 keV are very weak. Their peak areas were very carefully evaluated. In order to get more precise efficiency calibrations, the peak areas should be obtained by considering the effect of summing [65, 84, 85, 86, 87, 88, 89], positron annihilation, internal conversion and β efficiency.

Substituting all known values of efficiencies and peak net areas into Eqn. 4.1, we get the efficiency for γ–rays 7070 keV at 49 mm distance away from the source sample, which is 0.192(6)%. The Monte Carlo simulation with CYLTRAN gives a value of 0.189%, which is in agreement with measurement. The efficiency calibration curve of the HPGe γ detector up to 8 MeV at 49 mm distance away from the source sample is shown in Fig. 31. By using the same procedure, we get the efficiency for the 7070 keV γ–rays at 151 mm distance away from the source sample, which is 0.0385(8)%. The Monte Carlo simulation with CYLTRAN gives a value of 0.0399%, which differs from measurement by 4(2)%. This discrepancy leads us to assign an uncertainty of 4% to our efficiencies at 151 mm up to 8 MeV.

The β-γ coincidence spectrum of ^{23}Al was measured at a distance of 49 mm away from the source. To account for the fact that the efficiency calibration for the whole energy range is tested experimentally at 151 mm and simply calculated at 49 mm, we add 2% uncertainty for the HPGe efficiency at 49 mm, leading to a 2.2% to 5.2% relative error depending upon the γ energies (2.2% for 0.4 MeV and 5.2% for 8.0 MeV). These are the uncertainties we will apply to the β-γ coincidence spectrum of ^{23}Al.

The efficiency calibration of the HPGe with BGO experiment was not attempted since it was complicated by various difficulties (geometry, electronics, etc). However, from the ratios of known peak areas measured with and without the BGO, we can still roughly determine the intensity of new γ peaks found in the Compton-suppressed spectrum.

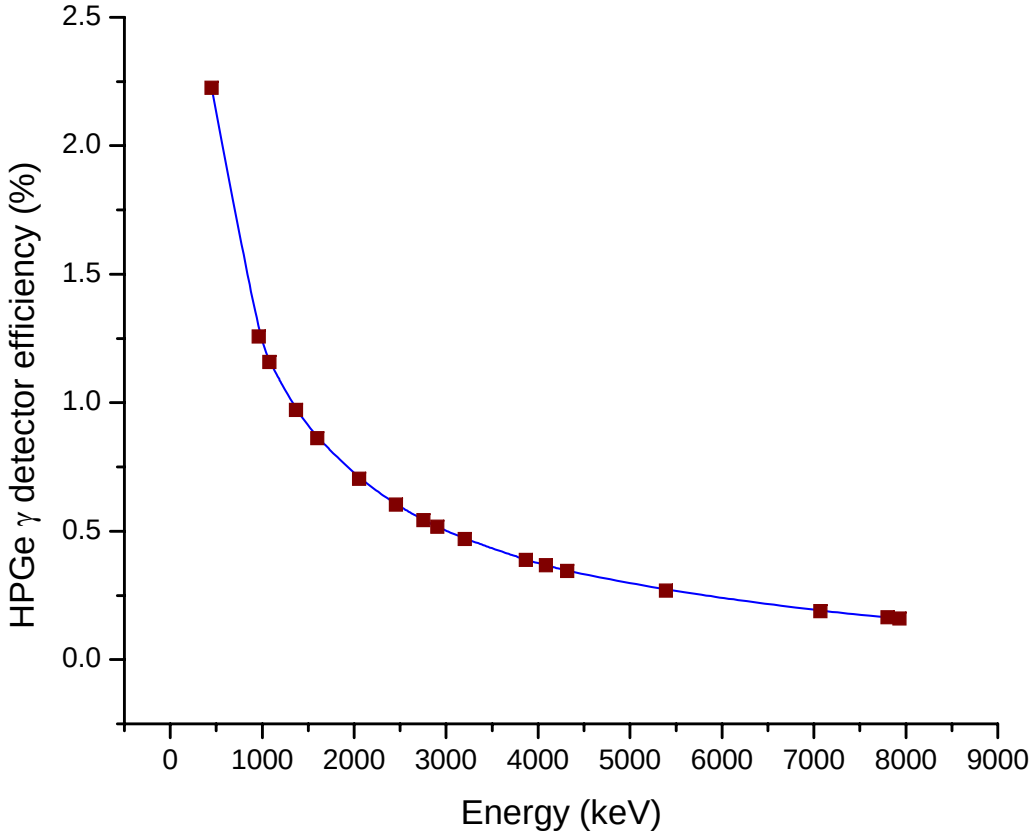

Fig. 31. The efficiency calibration curve of the HPGe γ detector at 49 mm away from the source sample for E_γ up to 8.0 MeV.

B. The β-decay Scheme of ^{23}Al

The γ–ray spectrum measured in coincidence with β's is presented in Fig. 32. The upper spectrum is shown in log scale over the energy range 0-4 MeV; below it, in linear scale, is the rest of the spectrum from 4 MeV to 9 MeV. Transitions to and from 15 distinct excited state levels in ^{23}Mg are observed. We clearly see γ–ray transitions depopulating the lowest lying states in ^{23}Mg: the $5/2^+$ state at $E_x = 450.7$ keV and the $7/2^+$ state at $E_x = 2051$ keV (corresponding γ-ray lines at $E_\gamma = 1599.5$ and 2050.8 keV). We also see a large number of γ-rays depopulating higher excited states up to $E_x = 7802.9(5)$ keV.

In total, twenty-five γ–ray peaks are identified as originating from the decay of ^{23}Al. To determine their absolute intensities, we first need an accurate knowledge of the absolute efficiency of our HPGe detector [see Section of the efficiency calibration]. We have calibrated the energy and efficiency of the γ detector up to 8 MeV as described above. Now with these efficiencies determined for the 49 mm source-to-detector distance used for ^{23}Al, we obtained absolute intensities for the observed γ–rays and constructed a decay scheme that includes 15 β–decay branches to states in ^{23}Mg, including the ground state, from those results.

To build the ^{23}Al β–decay scheme, we have used the standard spectroscopic criteria for data with no γ–γ coincidence. First, the true γ–rays were established by removing the single escape, double escape peaks, and the coincidence summing γ transitions. Second, I looked into the existing level scheme of ^{23}Mg daughter and fitted E_γ–rays in the known scheme (such as 450.7, 2050.8, 1599.5, 7352.3 and 7801.5 keV). Third, I found γ–rays decaying from the same level but feeding different final states, they should differ by known quantities (450.7 and 1599.5 keV). When 2 or 3 γ–rays lines come from same state, the state is confirmed and the excitation energy is

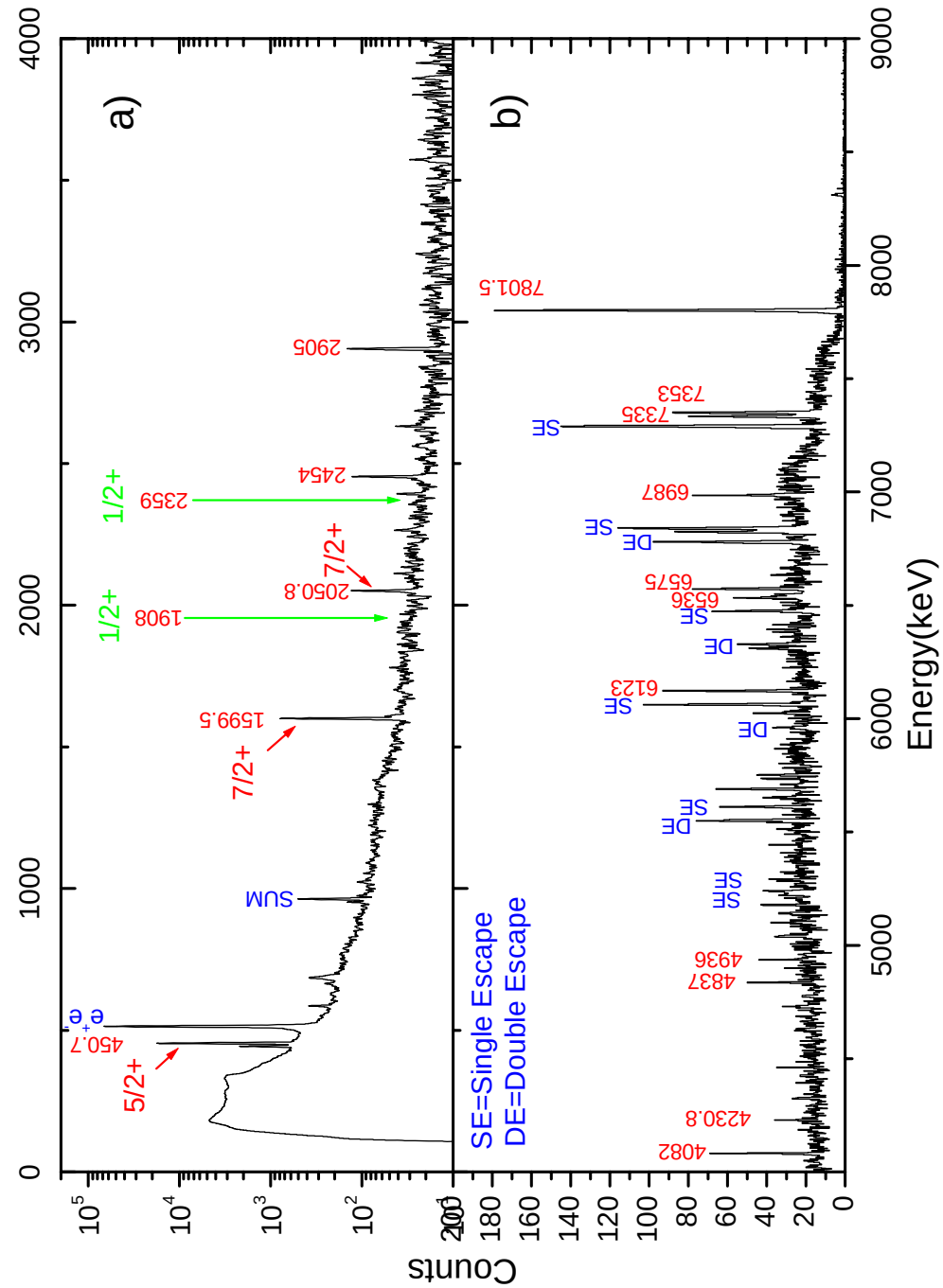

Fig. 32. The β-coincident γ-ray spectrum from ^{23}Al decay(RUN Sept 2006). (a) The energy range E_γ = 0-4 MeV (notice the log scale). (b) The energy range E_γ = 4-9 MeV (linear scale). SE and DE denote single-escape and double-escape, respectively.

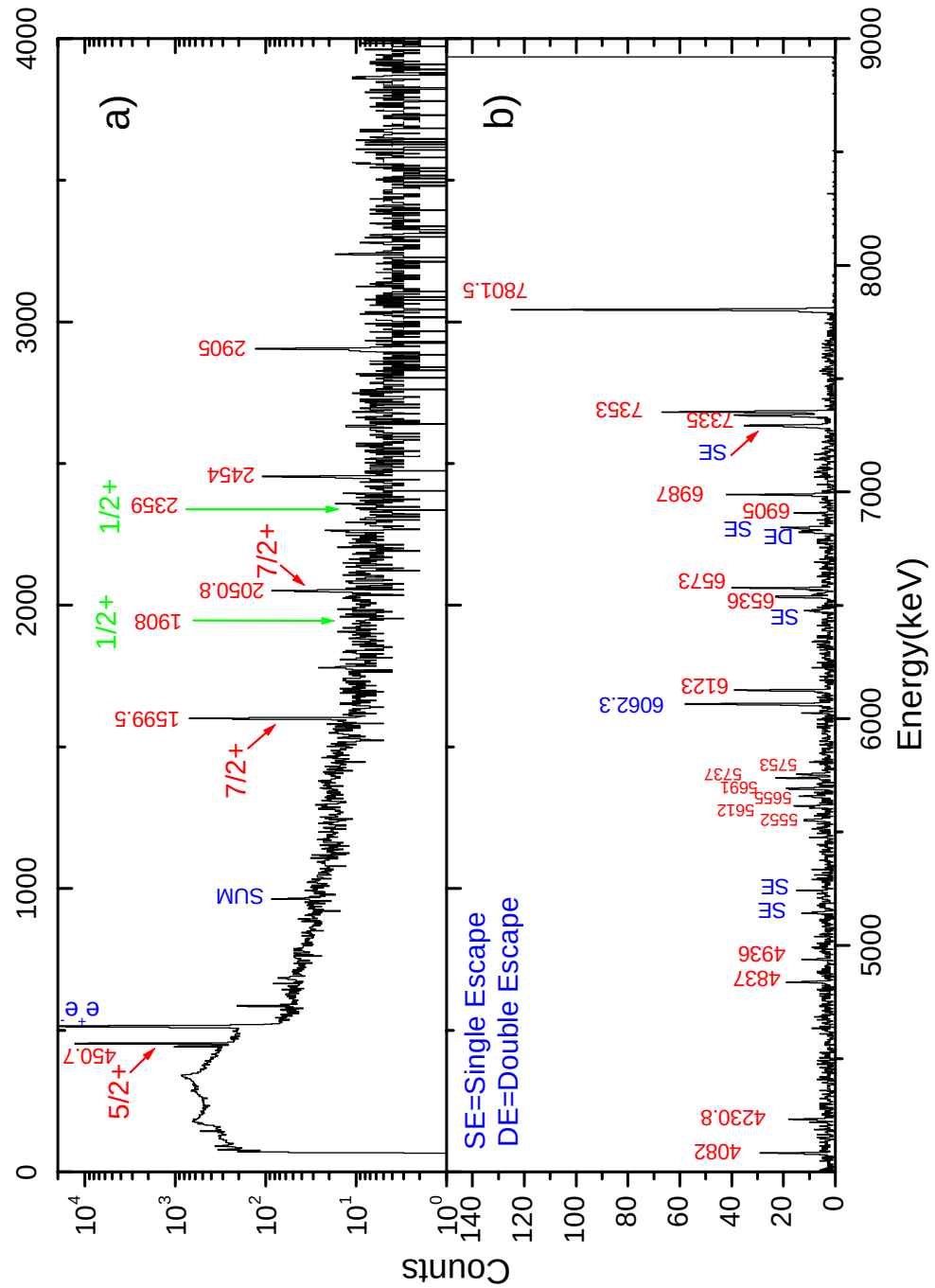

Fig. 33. The β-coincident γ-ray spectrum from ^{23}Al decay(RUN November 2006) with a BGO Compton shield. (a) The energy range E_γ = 0-4 MeV (notice the log scale). (b) The energy range E_γ = 4-9 MeV (linear scale). SE and DE denote single-escape and double-escape, respectively. Thye are much reduced here.

well determined (examples: 6063.3, 6575.1, 6987.4, 7787.2 and 7802.9 keV). Fourth, I identified the energy levels known from literatures with proper J^{π}, but less certain energies. Fifth, where none of the above could be used, we placed the γ–rays as feeding directly into the ground states (such as 3864.0 and 4083.1 keV). The ^{23}Al decay scheme will be finely tuned by considering all of the available information. Two new excited states, 4083 keV and 6063 keV, were determined.

The ^{23}Al β–decay scheme is shown in Fig. 34. The energies, intensities and decay scheme assignments of the observed γ–rays are listed in Table V. The summing effect correction and 511 keV correction are considered when the intensities were obtained.

Table V.: The energies, intensities and decay scheme assignments of the observed γ–rays normalized such that the flux into the ^{23}Mg first excited state 451 keV is 100.

E_γ(keV)	I_γ	E^*_i(keV)	E^*_f(keV)
450.7(4)	100	451	0
664.0(7)	0.17(4)	2715	2051
1599.5(4)	10.89(45)	2051	451
2050.8(5)	1.75(21)	2051	0
2263.8(7)	0.50(10)	2715	451
2453.8(7)	2.36(23)	2905	451
2904.8(5)	3.47(32)	2905	0
3863.7(7)	0.57(18)	3864	0
4082.3(6)	1.56(27)	4083	0
4836.7(7)	0.87(25)	5287	451
4935.9(7)	0.48(21)	6987	2051

Table V continued

E_γ(keV)	I_γ	E_i^*(keV)	E_f^*(keV)
5240.8(7)	0.68(26)	5691	451
5611.7(6)	1.45(38)	6063	451
5654.7(8)	1.27(41)	5655	0
5690.6(6)	2.46(41)	5691	0
5735.4(7)	1.53(36)	7787	2051
5751.7(7)	1.58(38)	7803	2051
6062.4(5)	3.10(74)	6063	0
6123.3(5)	4.78(63)	6575	451
6535.8(7)	2.96(64)	6987	451
6573.5(6)	3.65(58)	6575	0
6904.5(7)	1.49(37)	6905	0
6986.7(7)	3.89(79)	6987	0
7335.2(6)	6.63(87)	7787	451
7352.3(6)	8.43(97)	7803	451
7801.5(5)	20.9(18)	7803	0

It is interesting to note that we observe a 583 keV peak in our γ–ray spectrum, which is due to the decay of the first excited state of ^{22}Na. Since we took extra precautions to ensure that no ^{22}Mg impurity was present in our collected sample, we must conclude that this γ–ray signals the presence of β–delayed proton decay channels from ^{23}Al that populate the first excited state of ^{22}Na in addition to its ground state. Neither published study of delayed protons from ^{23}Al [12, 11, 13] attributed any of

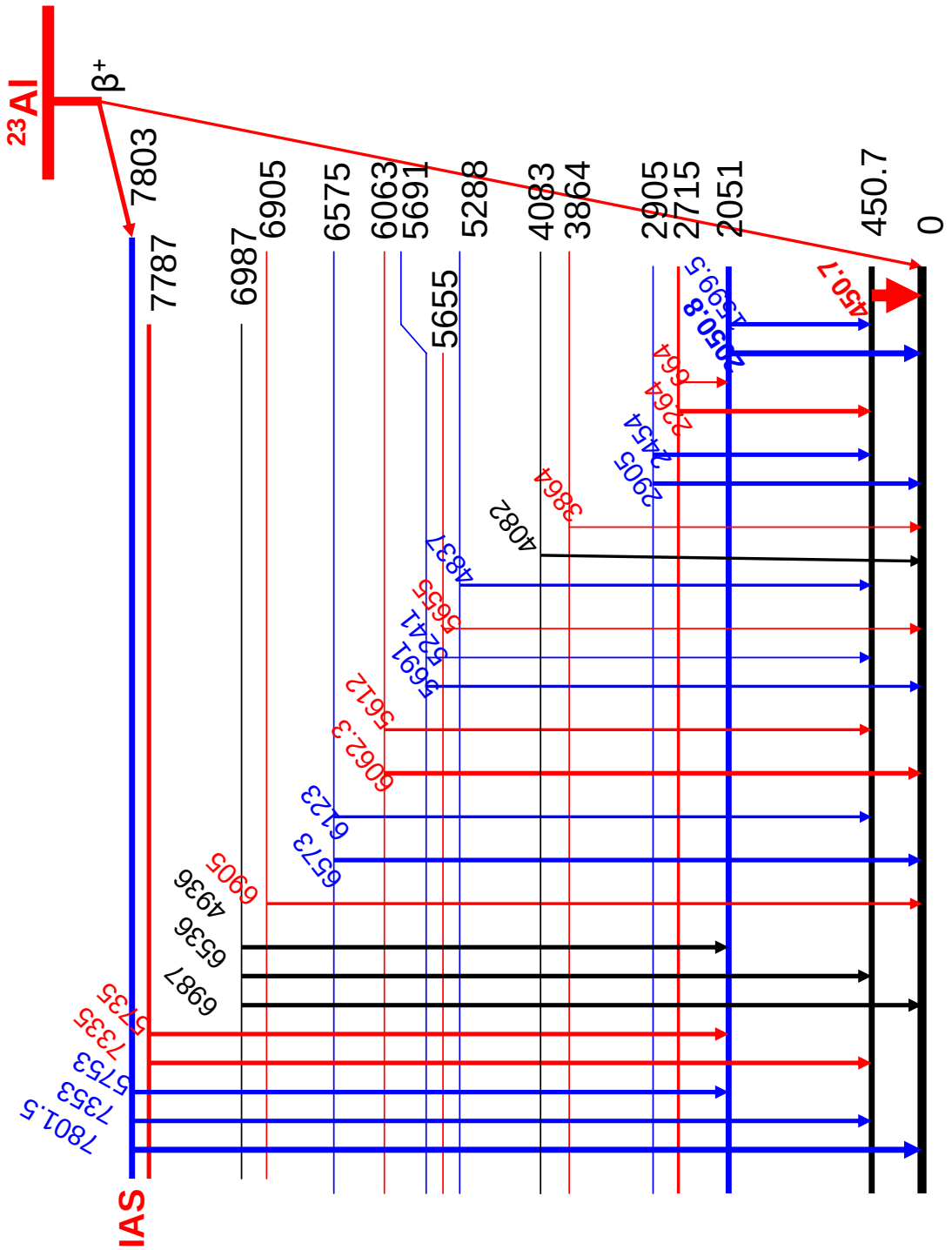

Fig. 34. ^{23}Al β–decay scheme after Nov. 2006 run data.

their peaks to an excited-state channel, but they did not eliminate the possibility either. In any case, we conclude from the measured intensity of our 583 keV γ–ray peak that the contribution of the β–delayed proton decay branch to the first state of ^{22}Na is about 0.25%. Its effect on the results of branching ratios and logft of the ^{23}Mg excited states is thus negligible.

It is also interesting to note that we observe a 6062.3 keV peak with strong intensity in Fig. 33, which shows the ^{23}Al γ–ray spectrum measured in coincidence with β's, including a BGO Compton shield on the HPGe γ detector. Comparing Fig. 33 with Fig. 32, we see that the background is significantly reduced in the higher energy region of the γ spectrum in Fig. 33. Single escape and double escape peaks are considerably reduced and some have been removed by the BGO Compton shield. Comparing the intensity of the 6062.3 keV γ–ray with that of the 6573 keV γ–ray in Fig. 33, we observe that the 6062.3 keV γ–ray is stronger. In all other cases, the intensity of a first escape peak is weaker than that of its parent peak. Thus the γ–ray 6062.3 keV peak is actually a sum of two peaks, one from the first escape of the γ–ray at 6573 keV, and other one from a real peak with an essentially identical energy of 6062 keV.

It is worth noting here that full consistency is observed when comparing the two experimental measurements with and without the BGO shield. Actually, more information is obtained in the higher γ energy region by the measurement with the BGO. The intensities of the γ–ray lines seen only with the BGO were obtained with an efficiency scaled to that of the experiments without the BGO.

It is important for the following analysis that we establish the contribution of room background both to the β-γ coincidence spectrum and to the β–detector singles rate. For this purpose we recorded data with the cyclotron beam on, but with a thick degrader inserted upstream from the tape. Everything was thus identical to a

normal measurement except that no ^{23}Al was implanted in the tape. The coincidence rate was observed to drop to 0. The β-singles rate was observed to drop to 0.04% of the rate observed when ^{23}Al was correctly implanted. Room background was thus negligible in our analysis.

C. The β-Branching Ratios

As mentioned in the β–decay theory part of Chapter II, a radioactive decay can proceed to different final states, i. The branching ratio b^i_β for a decay is the ratio between the decay rate to an individual state and the total decay rate. For our particular ^{23}Al β–decay, the β branching ratios b^i_β can be written as follows

$$b^i_\beta = K N^i_{\beta\gamma} / N_{\beta(^{23}Al)}, \tag{4.2}$$

$$N_\beta = N_{\beta(^{23}Al)} + N_{\beta(daughter)} + N_{\beta(impurity)}, \tag{4.3}$$

$$N_{\beta(^{23}Al)} = [\sum_{i=0}^{n} \varepsilon^i_\beta b^i_\beta] N_0, \tag{4.4}$$

$$\sum_{i=0}^{n} b^i_\beta = 1, \tag{4.5}$$

$$N^i_{\beta\gamma} = [\sum_{j<i} A_\gamma(E_{ij})/\varepsilon_\gamma(E_{ij})] - [\sum_{k>i} A_\gamma(E_{ki})/\varepsilon_\gamma(E_{ki})], \tag{4.6}$$

where K is a factor ($\sim$1) that accounts for small experimental corrections that will be enumerated in what follows, N_β is the total number of the positrons detected, $N^i_{\beta\gamma}$ is the number of the positrons populating directly level i, N_0 is the number of the β–decays, ε^i_β is the efficiency of the β detector for the transition to i which includes

the geometry (∼0.5) and the energy dependence (∼end-point energy and the types of β-spectra), b^i_β is the β branching ratio to the level i that is to be determined, $\varepsilon_\gamma(E_{ij})$ is the absolute γ–ray efficiency of the HPGe detector at E_{ij}, $A_\gamma(E_{ij})$ is the net area of the γ–ray peak at E_{ij}, $N_{\beta(^{23}Al)}$ is the β particles from the parent (^{23}Al), $N_{\beta(daughter)}$ is the β particles from the daughter (^{23}Mg) and $N_{\beta(impurity)}$ is the β particles from the impurities.

The ^{23}Al beam purity was better than 99% when it stops in the aluminized mylar tape after passing through a set of alumun degraders. From the gamma-ray spectrum we do not have any indication for impurities (except maybe for that of the 583 keV that is about 0.25%) and, therefore, take the $N_{\beta(impurity)}$ a neglible contribution. However, the $N_{\beta(daughter)}$ is considerable. ^{23}Mg is the daughter nucleus that β^+ decays to ^{23}Na. The ^{23}Mg decay scheme (simple and easy to analyze) can be obtained from NNDC [20], i.e. we know its half life (11.317 seconds), β branching ratios, γ transition intensities, etc. The ratio of $N_{\beta(^{23}Al)}$ and $N_{\beta(daughter)}$ was obtained from the known half lives of ^{23}Al and ^{23}Mg and the times for irradiation, transport and measurement: $N_{\beta(daughter)}/N_{\beta(^{23}Al)}$=0.297(20). The intensity of the γ transition at 440 keV belonging to the ^{23}Mg daughter nucleus β^+ decay to ^{23}Na was measured when measuring the ^{23}Al β–γ coincidence. From this transition, the $N_{\beta(daughter)}$ can also be obtained from the known ^{23}Mg decay scheme: 8.2(3)% branching. The values of $N_{\beta(daughter)}$ obtained from the two methods are consistent within the error bars which were brought by the uncertainties of the half life, the β efficiency and the branching ratio of the 440 γ line in ^{23}Mg.

Before determining the branching ratios from the experimental data, we eliminated those cycles in which the collected source was not positioned exactly between the β and γ detectors. Although the tape-transport system is quite consistent when placing the collected source within ±3 mm of the designated counting location, it

is a mechanical system, and occasionally larger deviations occur. For each cycle we recorded not only the total number of positrons detected but also the total number of heavy ions (most of them were ^{23}Al) which emerged from the MARS spectrometer, by using the scintillator located immediately in front of the aluminum degraders. The ratio of the former to the latter is a sensitive measure of how well the source is positioned with respect to the β detector. When analyzing the data, we rejected the results from any cycle with an anomalous (low) ratio. A cycle will be selected as a good cycle if the ratio of β over heavy ion is between 0.06 and 0.08. A cycle will be rejected as a bad cycle if the ratio of β over heavy ion is between 0.02 and 0.04. There are also some cycles not including any data because of no beam. For example, the ^{23}Al β-γ coincidence measurement (49 mm distance) in September 2006 has 1550 cycles data. There are 1180 good cycles, 325 bad cycles and 45 no beam cycles respectively. Then the rejected fraction is around 21%.

As discussed above, the absolute efficiency, ε_γ, of the HPGe detector at 15.1 cm is known to $\pm$0.2%. This, however, applies to a highly controlled situation in which the source-to-detector distance can be measured from micrometers to a small fraction of a millimeter. With the fast tape-transport delivery system, we can not ensure reproducibility at the same level of precision. Taking $\pm$0.5 mm as the actual uncertainty in position under our experimental conditions (the distance between the ^{23}Al source and HPGe is 49 mm), we add an uncertainty of $\sim$2% to the detector efficiency in quadrature with the basic $\sim$0.2% uncertainty.

It is important to evaluate K by taking into consideration small experimental corrections to achieve high precision on the branching ratios. In fact, K is a product of four separate corrections, $K1$, $K2$, $K3$ and $K4$ which is close to 1. We will deal with each one individually as in Ref. [90].

Random coincidences ($K1$). There is always a random coincidence contribution

to the $\beta - \gamma$ coincidence measurement. The correction factor here is taken to be between 0.995 to 1.0 which depends on the different transitions. Naturally, this correction accounts not only for random coincidences among ^{23}Al β's and γ-rays but also for random coincidences between ^{23}Al β particles and any γ-rays originating from room background.

Real-coincidence summing ($K2$). Since we are measuring a β^+ decay, positrons are annihilated, resulting in two 511 keV γ–rays. There is a significant probability that a γ–ray from ^{23}Mg decay and a 511 keV annihilation γ–ray will reach the γ detector simultaneously and be recorded as a single event. For example, we observe a 962 keV γ–ray which is the sum of 451 keV and 511 keV γ–rays. Any summing of this kind will reduce events in the 451 keV photopeak. The first step to account for the resultant loss is to obtain the area of the observed 962 keV (451 + 511) sum peak. Since losses from the 451 keV photopeak result not only from its summing with the 511 keV photopeak but also with the latter's Compton scattered radiation. In the second step, we multiply the sum-peak area by the known *total-to-peak* ratio for the HPGe detector at 511 keV(see Fig. 11 in Ref. [67]). Actually, the summing effect is relative to the specific γ transitions. It will affect the net areas of γ peaks. So the summing effect has been considered in the part when the γ transition peaks are being fitted and net areas are being subtracted during the data iteration processing. So the *real-coincidence summing* is simply taken to be 1 here, i.e. $K2 = 1.0$.

Dead time ($K3$). The β-γ coincidence measurement is performed by recording the β particles and the γ–rays simultaneously. During the counting, however, the dead time of the circuit for the β-γ coincidence, $N_{\beta\gamma}$, which is limited by the relatively slow electronics used for γ–ray counting, is much greater than that for simply scaled N_β. We determine the dead time associated with $N_{\beta\gamma}$ from the total rate in the HPGe detector during counting. This is done from the known processing time (32 μs) for

each coincident event. The shaping time is 4 μs. The scaler dead time per event is only 100 ns, but the total rate in the scaler is much higher than the HPGe rate; nevertheless the dead time associated with N_β turns out to be smaller by a factor of three than that associated with coincidence events. The overall correction factor is $K3 = 1.0018(1)$.

The β-detector response function ($K4$). The correction factor associated with the β-detector response function is given by

$$K_4^i = \varepsilon_{\beta_{total}}/\varepsilon_{\beta_i}, \tag{4.7}$$

where $\varepsilon_{\beta_{total}}$ is the total β efficiency, and ε_{β_i} is the efficiency at β energy $E_{\beta i}$.

If the detector response function is completely independent of energy, then this correction factor would be unity. In fact, the efficiency does change slightly with energy. This was discussed before in the section on the HPGe detector efficiency calibration.

Multiplying $K1$ through $K4$ we determine the correction factor in Eq. 4.2 to be between $0.9968(1)K_4^i$ and $1.0018(1)K_4^i$.

From β–singles and $\beta - \gamma$ coincidence experimental data, we derive the β–decay branching ratios by assuming detailed balance between the total feeding and the decay for each level. Because the density of states is relatively low in a light nucleus like ^{23}Mg, the effect of unobserved γ–rays on the branching ratios (the pandemonium effect [91, 92]) should be small enough to be absorbed within other uncertainties. The branching ratio values and other properties of the observed decay of ^{23}Al to final states in ^{23}Mg are listed in Table VI. The recoil energy correction was included when calculating the excited state energies. The spins and parities listed for the ground state and first three excited states were known previously [93]. Those for the rest of the states are deduced from our measurements by comparing to other experimental

results (NNDC) and by using the Gamow-Teller transition rules. We obtained the branching ratio for the direct population of the g.s. of ^{23}Mg, $\varepsilon^0_\beta b^0_\beta N_0$, using equation 4.4.

The error budget for the measured branching ratio of the observed decay of ^{23}Al to final states in ^{23}Mg is shown in Table VII.

D. Half Life of ^{23}Al

To extract accurate logft values, we need precise branching-ratios as well as an accurate half-life and mass for the parent nucleus, ^{23}Al.

The measurement of the half life of ^{23}Al was motivated by the poor precision of the currently accepted value, $t_{1/2}$=470(30) ms [93]. Since ^{23}Al decays by β–delayed proton emission as well as by β–delayed γ–rays, and both decays result in daughter nuclei that are themselves radioactive, a measurement of decay positrons with our standard proportional gas-counter [94, 95] may involve too many impurity activities to yield a reliable result for the half life for ^{23}Al. Instead, we measured off-beam β-γ coincidences as a function of time using our fast tape-transport system, and analyzed the time spectra of those γ–rays uniquely associated with ^{23}Al.

The β-γ coincidence data acquisition process was discussed in Chapter III. The collect-move-detect cycles were repeated until sufficient statistics were acquired. The control sequence is shown in Fig. 23.

In the off-line analysis, only the most intense γ–ray transitions in the ^{23}Al decay, γ–rays of 450.7 keV and 1599.5 keV, were selected to generate a net decay spectrum. In the time-spectrum associated with the peak of a given γ–ray, the net decay spectrum can be obtained by subtracting the corresponding background observed on either side of the γ peak. This process is shown in Fig. 35 by using the 450.7 keV

Table VI. The states in ^{23}Mg populated in the β–decay of ^{23}Al. The recoil energy correction was included when calculating the excited state energies. The last column gives the sources or reasons for the spin and parity assignment. NA means Not available, and * means a new state obtained from our experiment.

Previously known level	E_{level}(keV)	Branching Ratios(%)	Logft	T	J^π	Assignment from
0	0	36.16(113)	5.34(2)	1/2	$3/2^+$	NNDC
450.71(15)	450.7(4)	25.33(95)	5.40(1)	1/2	$5/2^+$	NNDC
2052.2(9)	2051.0(5)	3.90(15)	5.85(2)	1/2	$7/2^+$	NNDC
2359.0(14)	2359	<0.1	>7.4	1/2	$1/2^+$	NNDC
2908.1(20)	2905.0(5)	2.54(16)	5.83(3)	1/2	$(3,5/2)^+$	NNDC
3864(5)	3864.0(7)	0.25(8)	6.59(14)	1/2	$(3,5/2)^+$	NNDC
NA	4083.1(6)*	0.68(11)	6.34(13)	1/2	$(3,5,7/2)^+$	This Exp.
5287(6)	5288.2(7)	0.38(11)	5.97(13)	1/2	$(3,5/2)^+$	NNDC
5656(7)	5655.3(7)	0.56(18)	5.67(14)	1/2	$5/2^+$	NNDC
5691(8)	5691.4()	1.95(32)	5.10(7)	1/2	$(3/2 \text{ to } 7/2)^+$	This Exp.
NA	6063.3(5)*	2.45(27)	4.86(6)	1/2	$(3/2 \text{ to } 7/2)^+$	This Exp.
6568(8)	6575.1(6)	3.68(34)	4.48(4)	1/2	$5/2^+$	NNDC
6899(5)	6905.4(7)	0.55(16)	5.16(13)	1/2	$5/2^+$	NNDC
6984(5)	6987.4(7)	3.24(44)	4.36(6)	1/2	$5/2^+$	NNDC
7785.7(11)	7787.2(6)	3.95(37)	3.85(5)	1/2	$(7/2)^+$	Jenkins
7802.2(14)	7802.9(5)	13.69(72)	3.305(23)	3/2	$5/2^+$(IAS)	Perajarvi + This Exp.

Table VII. The error budget for the measured branching ratio of the observed decay of ^{23}Al to final states in ^{23}Mg.

Origin of Uncertainty	% Uncertainty
HPGe detector efficiency	2.2-5.2 (depends on gamma energy at 0.4-8.0 MeV)
Source-detector distance	2
Random coincidences	0.05
Dead time	0.02
β-detector efficiency vs energy	0.13

γ–ray as an example. Figure 36 shows the net decay spectrum consisting of a total of about 1.3x10^5 events in the sum of the 450.7 keV and 1599.5 keV γ peaks. While the selection of the ^{23}Al decay events by their γ–ray energies simplifies the analysis significantly, the very different dead-time corrections in the β, γ and β-γ coincidence channels require a detailed analysis, especially since the total decay-rates in the β and γ detectors are not proportional to the decay rate of ^{23}Al. This can be easily observed in Fig. 36, where the scaled-down total γ–rate (solid line) obviously contains contributions from decays with longer half-lives than that of ^{23}Al. The daughter nucleus ^{23}Mg ($T_{1/2}$=11.317 seconds) also undergoes β^+ decay to ^{23}Na. So β particles and γ transitions from both ^{23}Mg and ^{23}Al decay are recorded by the β and γ detectors. The corrections of the dead time need to consider these decay rate changes.

During data acquisition, the observed data rate is not equal to the real data rate due to the dead times of the electronics. It is shown below.

$$Rate_{observed} = (\varepsilon_{detector})(Rate_{real})(DeadTime_{corrections}), \tag{4.8}$$

where $\text{Rate}_{observed}$ is the observed data rate, $\varepsilon_{detector}$ is the efficiency of the detector,

Rate_{real} is the real data rate and $\text{DeadTime}_{corrections}$ is the dead time corrections.

For our experiments, the estimation for the real rate is shown below.

$$Rate_{real} = Events_{measured}/T_{active}, \tag{4.9}$$

$$Rate_{real} = (Rate_{measured})(\Delta T)/[\Delta T - (Rate_{measured})(\Delta T)(\delta T)], \tag{4.10}$$

$$Rate_{real} = Rate_{measured}/[1 - (Rate_{measured})(\delta T)], \tag{4.11}$$

where $\text{Events}_{measured}$ is the measured events within the time (T_{active}) when electronics is active, $\text{Rate}_{measured}$ is the measured rate of the detector, ΔT is the detect time and δT is the dead time.

The β-γ coincidence channel dead time is around 32 μs. The γ singles channel dead time is around 8 μs. The β single channel dead time is less than 1 μs. The average data rate of the β-γ coincidence is around 15 Hz.

Doing a linear fit to the net γ–ray decay curve shown in Fig. 36, the slope of the curve is obtained. The result of the half life deduced from the experimental coincidence data is $\text{T}_{1/2}(^{23}\text{Al}) = 447(4)$ ms [96]. This is consistent with the previously accepted value of 470(30) ms, but it is more accurate.

E. Mass of ^{23}Al

The mass of ^{23}Al can be deduced from the Isobaric Multiplet Mass Equation [97, 98]. An isobaric multiplet is made of $|\alpha,\text{T},\text{T}_z>$ states with the same isospin T but different isospin projection T_z=-T,...,T. These states belong to different nuclei. The isobaric-multiplet concept has been successfully applied in explaining the similar level

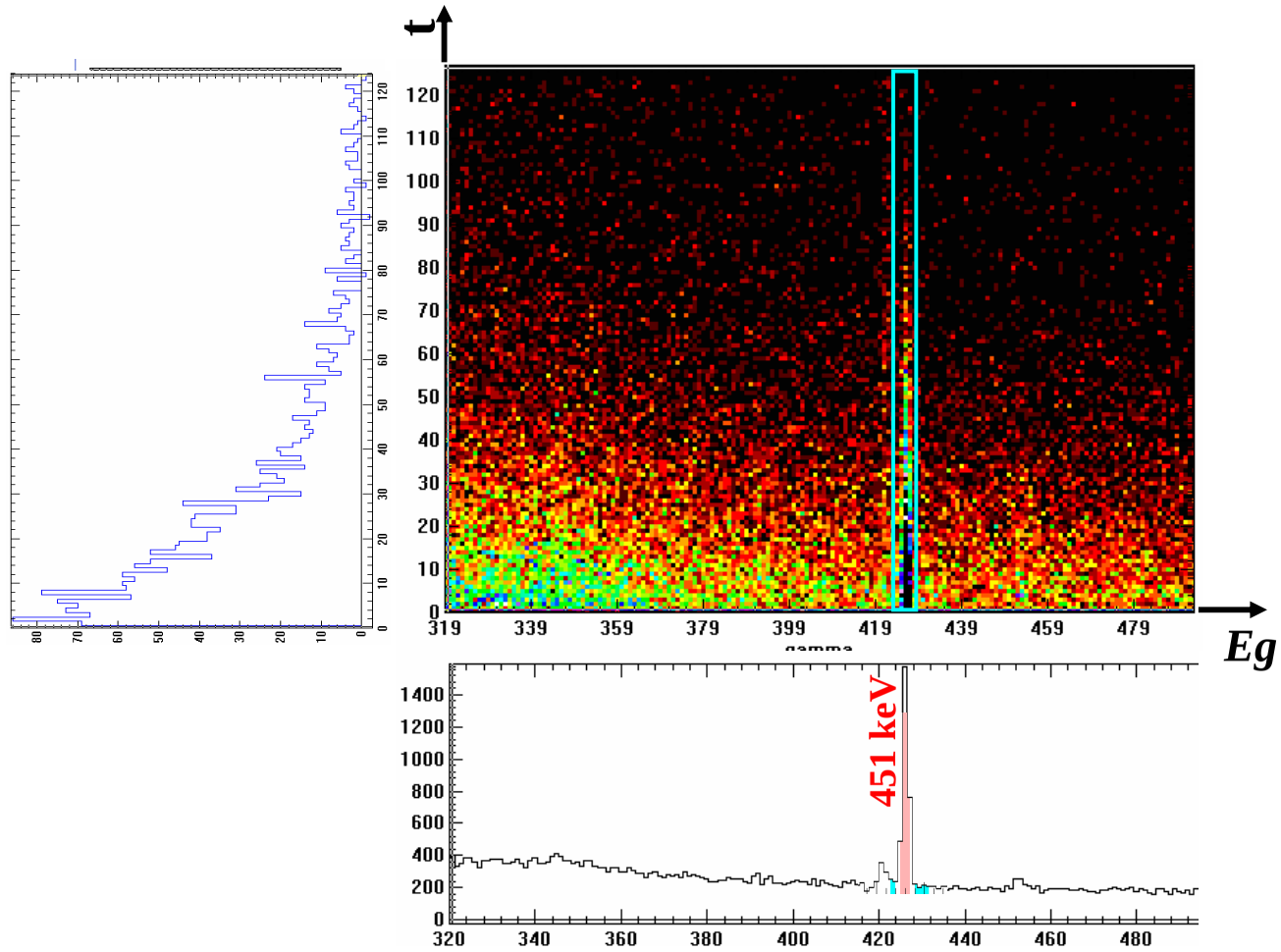

Fig. 35. The 450.7 keV γ–rays was selected to generate a net decay spectrum. In the time-spectrum associated with the peak 450.7 keV γ–ray, the net decay spectrum can be obtained by subtracting the corresponding background observed on either side of the γ peak from the data. The Highlighted area was projected to the left and down to generate two spectra which are counts vs decay time and counts vs γ energy, respectively.

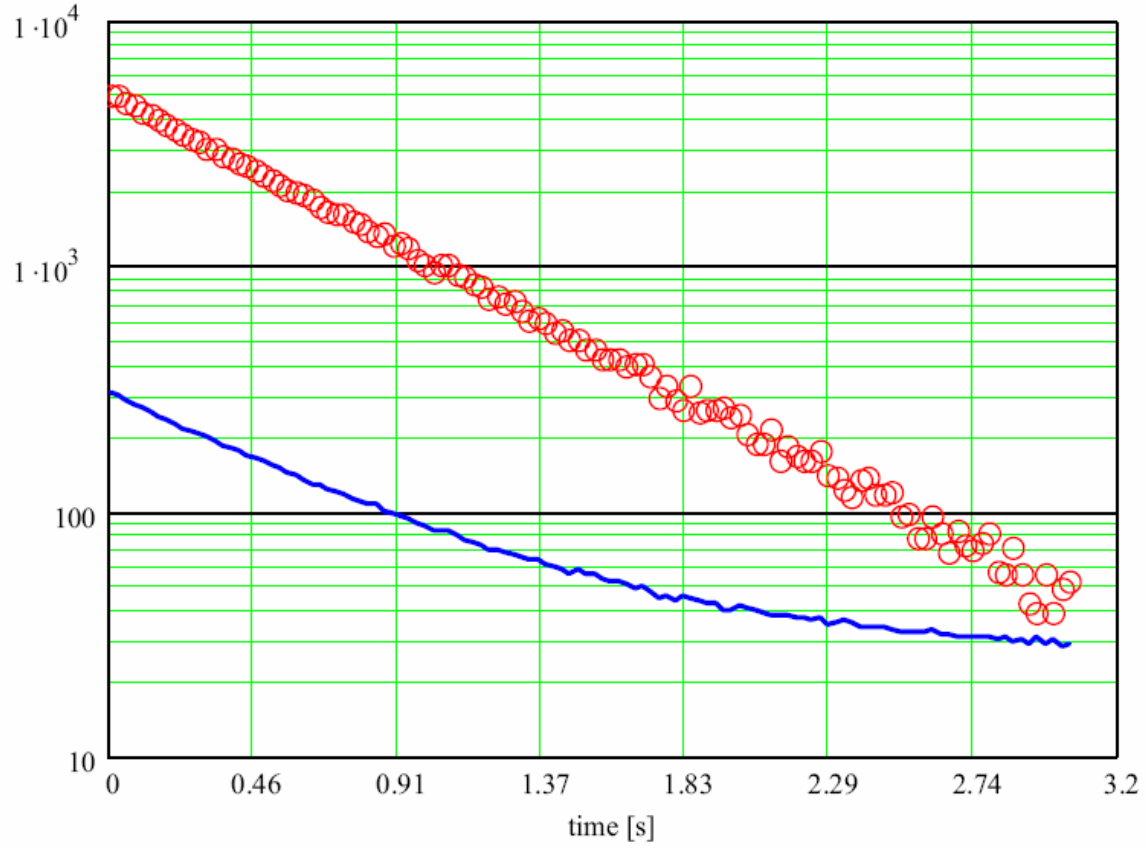

Fig. 36. Net versus total γ–spectra observed in the decay of ^{23}Al. Open circles represent the net decay spectrum of ^{23}Al as observed in $\beta - \gamma$ coincidences. Only the two most intense γ–rays (450.7 keV and 1599.5 keV) were selected to generate the net decay spectrum which contains about 1.3x10^5 events. The solid line represents a scaled-down total γ–spectrum containing contributions from ^{23}Al and its several descendents, all of which are radioactive and generate γ–rays.

structure of mirror nuclei and the existence of analog states. The difference in mass is coming from the difference between neutron and proton masses and from the Coulomb interaction. Using isospin formalism, it is possible to obtain an equation quadratic in T_Z. The equation relates the masses of members of an isobaric multiplet

$$ME(T, T_z) = a + bT_z + cT_z^2, \tag{4.12}$$

where ME is the mass excess of a member of isospin T multiplet, T_z=(N-Z)/2 is its isospin projection which ranges from -T to +T, and a, b and c are the IMME coefficients.

For A=23, T=3/2 isobars, isospin projections for ^{23}Al, ^{23}Mg, ^{23}Na, ^{23}Ne are $-3/2$, $-1/2$, 1/2 and 3/2 respectively. The ground state (g.s.) of $^{23}_{10}\mathrm{Ne}_{13}$ and its mirror nucleus $^{23}_{13}\mathrm{Al}_{10}$(g.s.) are members of this multiplet, as well as their IAS in the T_z=1/2 (^{23}Na) and T_z=$-1/2$ (^{23}Mg) nucleus. In the next section, the logft value for the 7802.9(5) keV state of ^{23}Mg clearly identifies it as the IAS of the ^{23}Al ground state. We know the mass excess of the ground state of ^{23}Ne (T_z=3/2) and its IAS in ^{23}Na from Table VIII [19, 20]. We have produced the lowest T=3/2 state in ^{23}Al with the $^1H(^{24}\mathrm{Mg},^{23}\mathrm{Al})2n$ reaction and identified its isobaric analog state (IAS) in ^{23}Mg through the logft=3.305 (23). Measuring the energies of the deexcitation γ rays, we obtain an excitation energy of 7802.9(5) keV for the IAS, after correcting for recoil.

Now we substitute the T_z for ^{23}Al, ^{23}Ne, ^{23}Na(IAS) and ^{23}Mg(IAS) with values from the literature [20] into Eqn. 4.12, and then four equations are obtained:

$$ME(3/2, -3/2, ^{23}\mathrm{Al}) = a - 3b/2 + 9c/4, \tag{4.13}$$

$$ME(3/2, -1/2, ^{23}\mathrm{Mg}) = a - b/2 + c/4, \tag{4.14}$$

$$ME(3/2, 1/2, ^{23}\mathrm{Na}) = a + b/2 + c/4, \tag{4.15}$$

$$ME(3/2, 3/2, ^{23}\mathrm{Ne}) = a + 3b/2 + 9c/4, \tag{4.16}$$

where ME(3/2, 3/2, ^{23}Al), ME(3/2, 3/2, ^{23}Mg), ME(3/2, 3/2, ^{23}Na) and ME(3/2, 3/2, ^{23}Ne) are the mass excesses of the states in ^{23}Al, ^{23}Mg*, ^{23}Na* and ^{23}Ne respectively. Then the following equation can be obtained.

$$ME(3/2, 3/2, ^{23}\mathrm{Al}) = 3[ME(3/2, 3/2, ^{23}\mathrm{Mg}) - ME(3/2, 3/2, ^{23}\mathrm{Na})] + ME(3/2, 3/2, ^{23}\mathrm{Ne}). \tag{4.17}$$

Substituting the mass excesses [19] of the nuclei ^{23}Mg, ^{23}Na and ^{23}Ne into Eqn. 4.17, then the mass excess of ^{23}Al is obtained. i.e. ME(^{23}Al)=6749.7(23) keV.

Using the existing mass excess of ^{23}Al (6770(19) keV) [19] and the present value (6749.7(23) keV), we obtain a weighted average: ME(^{23}Al)=6750.0(25) keV. Using this average value in the evaluation of the logft leads to changes smaller than the uncertainties in Table VIII.

For the electron capture (EC) decay, the Q value is defined

$$\mathrm{Q}_{EC} = \mathrm{M}_P - \mathrm{M}_D, \tag{4.18}$$

where M_P is the atomic mass of the parent nucleus and M_D is the atomic mass of the daughter nucleus.

From Eqn. 4.18, we get Q_{EC}=12223.8(28) keV. Our measured Q_{EC} value agrees with the value from the latest mass tables [19] Q_{EC}=12243(19) keV, within the errors, but is more precise. The new improved value does not have much affect on the logft values, but affects the astrophysical S-factor for the radiative capture (p,γ).

Table VIII. The data table for values of T_z, ME^*_{gs}, Excitation energy, $ME_{T=3/2}$ and error bars. A=23 and T=3/2.

Isobars	T_z	ME^*_{gs}(keV)	$E_{excitation}$(keV)	$ME_{T=3/2}$(keV)	error(keV)
^{23}Al	-3/2	6769.6(186)	0	6750.0	2.5
^{23}Mg	-1/2	-5473.8(13)	7802.9(5)	2329.2	0.5
^{23}Na	1/2	-9529.9(0)	7891.2(6)**	-1638.7	0.6
^{23}Ne	3/2	-5154.0(1)	0	-5154.0	0.1
		*:Reference[19]	**:Reference[20]		

F. The logft Values

We can now obtain accurate logft values for the γ transitions from the β-γ coincidence data for ^{23}Al by using branching ratio and half-life results from the present measurements, together with the updated Q_{EC} value described above (from the mass measurement part). These calculations have been carried out with the NNDC logft β-decay calculator [99]. The logft values are listed in Table VI.

An important result evident from Table VI is the logft value we obtain for the transition to the 7802.9(5) keV state. The result, logft=3.305(23), is in agreement with the value expected for a predominantly Fermi transition between T=3/2 analog states: viz., log$ft\leq$3.31. This positively identifies the state as being the isobaric analog of the ^{23}Al ground state. Although the state has been seen before [13] and correctly assumed to be the IAS, its logft value had never been measured. The logft values reported here are calculated using the Q_{EC} value resulting from the IMME for A = 23 isobars with the energy of the IAS found in the last section of this chapter (Q_{EC} = 12223.8(28) keV), which can also be found in Ref. [13]. Using the value from the latest mass tables [19], we have Q_{EC} = 12243(19) keV. The uncertainty in the

Q_{EC} leads to variations smaller than our statistical error bars in logft values.

In addition to the IAS, we also find another state populated (logft = 3.76) only 16 keV below it at 7787(2) keV. For this state, we find γ–decay branching to the ground/first excited (451 keV)/second-excited (2051 keV) states 100/45(5)/5.5(21) and 3.8(25)/100/20(5), respectively. These are consistent with the measured β–decay branches. A state at (roughly) this energy has been seen before [15, 18]. It was also observed to decay predominantly to the 451-keV level, and is assigned to be $(7/2^+)$ in Ref. [18]. Observation of its production in allowed β-decay now makes its positive parity unambiguous. This is the first time to observe both the IAS and this $(7/2)^+$ state resolved from one another in the same experiment.

G. The Spin and Parity for the ^{23}Al Ground State

If we assume the ground state spin and parity for ^{23}Al is either $5/2^+$ or $1/2^+$, then there are two β–decay patterns for ^{23}Al. This is shown in Fig. 37.

It can be clearly seen from the ^{23}Al β–decay scheme shown in Fig. 38 that the β–decay from ^{23}Al populates the $3/2^+$ ground state of ^{23}Mg as well as $5/2^+$ and $7/2^+$ excited states at 450.7 and 2051 keV, respectively, with logft values characteristic of allowed Gamow-Teller transitions. Furthermore we do not observe the direct population of the $1/2^+$ excited state at 2359 keV; the lower limit we set on its log ft value is 7.4, a value which does not absolutely rule out allowed decay but makes it most unlikely. Given the $\triangle$J = 0,1 ($\triangle\pi$ no) selection rules for allowed β–decays, the observed strong population of $3/2^+$, $5/2^+$, and $7/2^+$ final states is sufficient evidence in itself to restrict the ground-state spin of ^{23}Al to be $5/2^+$. The absence of any observed transition strength to a $1/2^+$ state simply adds confirmation to that conclusion. This spin is also consistent with the expected mirror symmetry between ^{23}Al (with T_z =

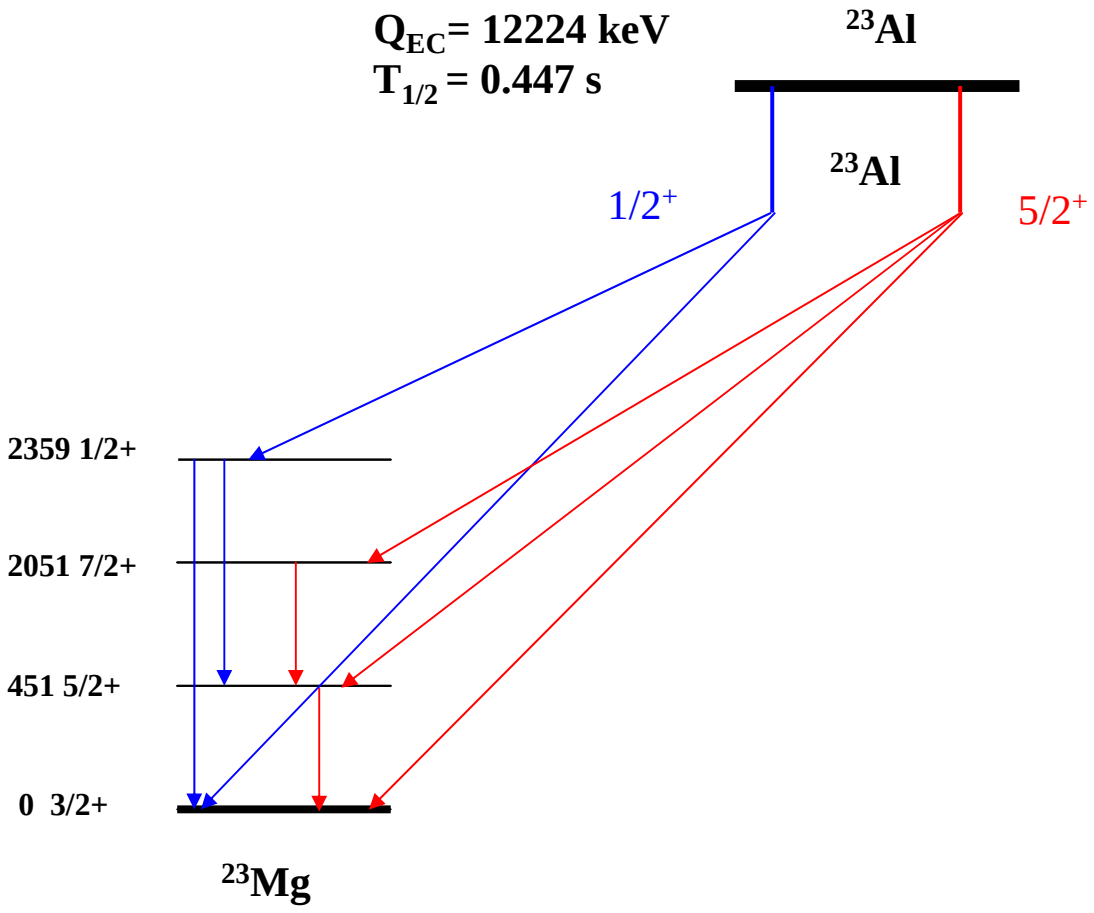

Fig. 37. Shown here are two β–decay patterns for ^{23}Al. Red lines represent decays with the the ground state spin and parity $5/2^+$ for ^{23}Al, corresponding to γ–ray lines at E_γ = 451, 1600 and 2051 keV. Blue lines represent decays with the the ground state spin and parity $1/2^+$ for ^{23}Al, corresponding to γ–ray lines at E_γ = 1908 and 2359 keV.

$-3/2$) and ^{23}Ne ($T_z = +3/2$), because the latter's ground state is already known to be $5/2^+$ [30]. Hence, the spin and parity of the ^{23}Al ground state is unambiguously determined to be $J^\pi = 5/2^+$. These results were published last year [100]. The ^{23}Al β-decay scheme is shown in Fig. 38.

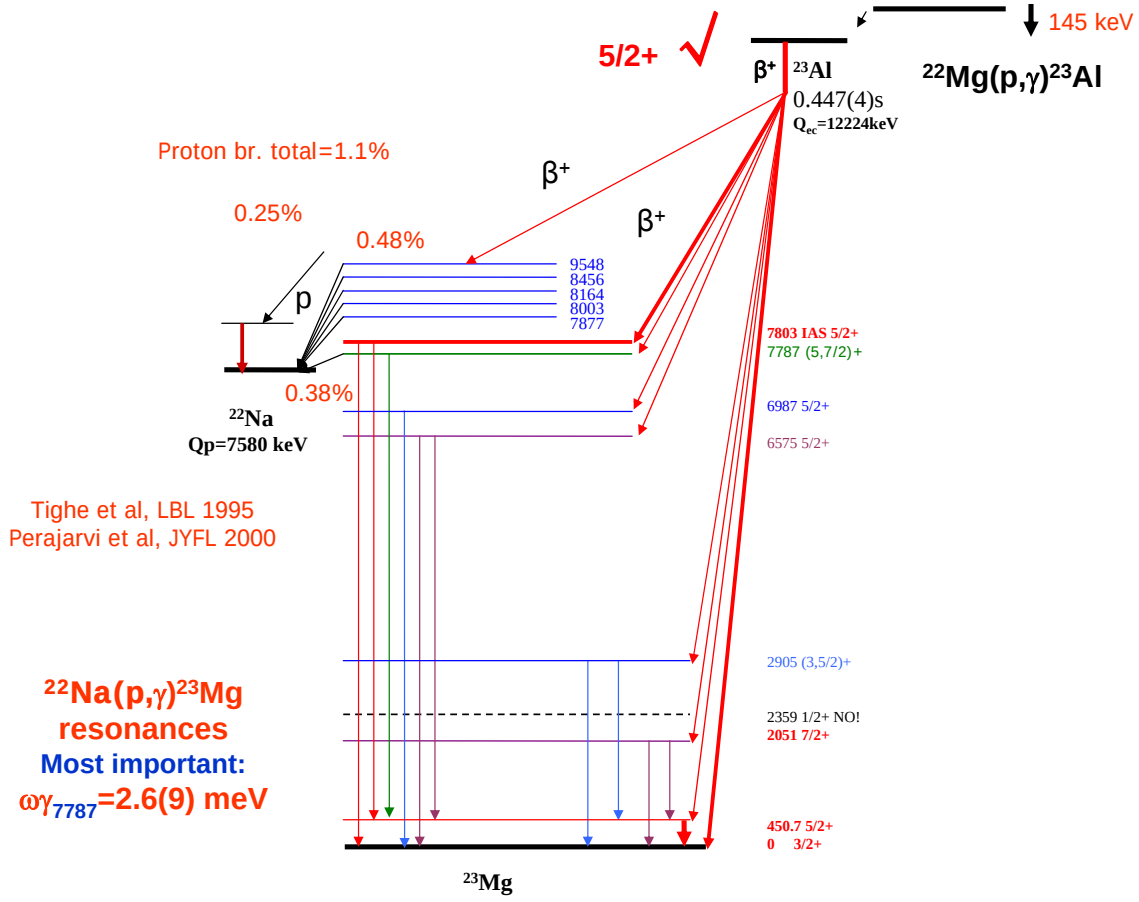

Fig. 38. β decay scheme of ^{23}Al including β–delayed proton decay information.

CHAPTER V

ASTROPHYSICAL CONSEQUENCES

The β–decay of the proton rich nucleus ^{23}Al has been studied for the first time with pure samples obtained by using the ^{1}H(^{24}Mg,^{23}Al)2n reaction and MARS, motivated by its nuclear astrophysics significance in the depletion of ^{22}Na. It is important for us to understand the processes that create and destroy ^{22}Na to diagnose classical nova outbursts. Explosions within a few kiloparsecs of the Sun may provide detectable γ–ray fluxes associated with ^{22}Na decay [101]. In the past 25 years, much effort has been spent on experimentally searching for this γ–ray signature of classical novae, including balloon-borne experiments [102], the OSSE and COMPTEL experiments on board the CGRO [5, 103], and the recently launched INTEGRAL mission [101]. The problem, however, is still unsolved. The astrophysical consequences of our ^{23}Al β–decay experiment will be discussed in this chapter.

A. The ^{22}Mg$(p,\gamma)^{23}$Al Reaction

From the astrophysical point of view, since ^{22}Mg plays a crucial role in the synthesis of ^{22}Na through its β-decay, its destruction by ^{22}Mg$(p,\gamma)^{23}$Al reaction must be considered.

Wiescher et al. [9, 104] calculated the contribution of the direct capture to the ground state for ^{22}Mg$(p,\gamma)^{23}$Al reaction. He also measured the first excited state in ^{23}Al, which is a resonance in capture, and calculated its strength by using the shell model and mirror symmetry. However, due to the very low Q value (0.142 (3) MeV), a rapid photodissociation of ^{23}Al prevents ^{22}Mg destruction in equilibrium production. Actually, there is another reaction channel, ^{22}Mg$(\beta^{+},\nu)^{22}$Na, which produces ^{22}Na. The favored reaction channel depends on the structure of ^{23}Al.

In ONe novae nucleosynthesis, the ground state spin and parity for ^{23}Al can make a significant difference to the amount of ^{22}Na that is left following explosive burning [25]. Assuming the ground state spin and parity of ^{23}Al were $1/2^+$ instead of $5/2^+$, and then calculating the astrophysical S-factor and stellar reaction rate for the ^{22}Mg(p,γ)^{23}Al reaction, we found an increase of 30-50 times, as shown in Fig. 2, over the current estimate, which assumes $5/2^+$, for the temperature range of ONe novae T_9=0.1-0.5. This increase would result in a significant depletion of ^{22}Mg before it β decays into ^{22}Na, which could explain the non-observation of the 1.275 MeV γ-ray from γ-ray emitter ^{22}Na in the hot NeNa cycle. Determining the ground state structure of ^{23}Al was necessary to better understand the ^{22}Na yield in ONe novae, and important for its implications to nuclear astrophysics. Our measurement, however, has shown this is not a case.

Our ^{23}Al $\beta-\gamma$ coincidence experiment allowed us to measure β branching ratios and to deduce logft values for γ transitions to the final states in ^{23}Mg, including the important isobaric analog state. We can determine unambigously the spin and parity of the ^{23}Al ground state to be $J^\pi = 5/2^+$. This excludes the large increases in the radiative proton capture cross section for the ^{22}Mg$(p,\gamma)^{23}$Al reaction at astrophysical energies, which were implied by the claims that the spin and parity is $J^\pi = 1/2^+$.

The level structures of ^{23}Al and ^{22}Mg are shown in Fig. 39. We can see the first excited state of ^{23}Al, lying at 386 keV above the proton threshold, located near the Gamow energy in typical Novae. It seems that the resonant capture reaction through the first excited state in ^{23}Al is overwhelming. Our new determination of the mass excess of ^{23}Al leads to a small increase of the proton separation energy, S_p = 142(3) keV (It was 123 keV [14, 27]). This combined with the position of the 1^{st} excited state from Caggiano [10], leads to a smaller resonance energy, E_{res} = 386(26) keV. This energy factor alone increases the resonance contribution by an order of magnitude for

$T_9 \simeq 0.3$-0.5.

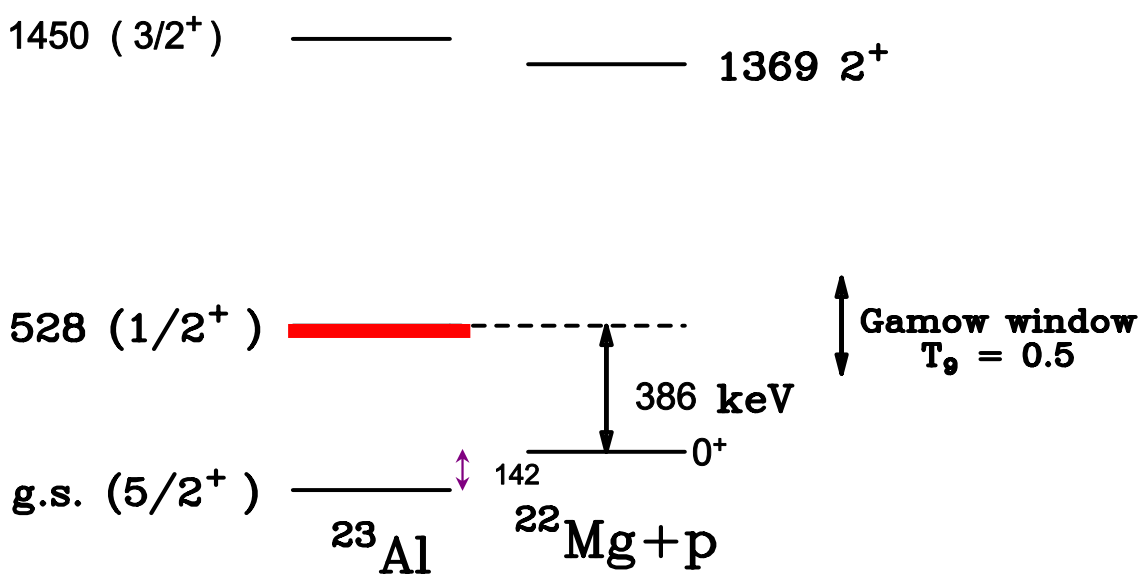

Fig. 39. The level structures of ^{23}Al and ^{22}Mg. Our new determination of the mass excess of ^{23}Al leads to an increase of the proton separation energy, $S_p = 142(3)$ keV (It was 123 keV), and then leads to a smaller resonance energy, $E_{res} = 386(26)$ keV.

We estimated the Γ_γ value ($6\text{x}10^{-7}$ eV) by using the single-particle wave functions for the E2 transition. This value agrees with the value published by a RIKEN group [105, 106, 107]. They determined the γ-ray width of its first excited state with the Coulomb dissociation of ^{23}Al. The Γ_γ value was used in the calculation of the resonant term shown in Fig. 2 for the capture reaction rate $^{22}\text{Mg}(p,\gamma)^{23}\text{Al}$.

B. The $^{22}\text{Na}(p,\gamma)^{23}\text{Mg}$ Reaction

The $^{22}\text{Na}(p,\gamma)^{23}\text{Mg}$ reaction is believed to play the most important role in the depletion of ^{22}Na in hot and dense astrophysical environments, such as super massive

stars, novae, and X-ray bursts. Reducing the uncertainty in the ^{22}Na$(p,\gamma)^{23}$Mg reaction rate may help to constrain nova models, improve the estimates on the amount of ^{22}Na synthesized during nova outbursts, and, therefore, dictate the distance at which a γ–ray flux from ^{22}Na may be detected. Several experimental approaches have been employed to obtain the astrophysical reaction rate for it [18, 14, 15, 16, 108]. It turns out that the largest contribution comes from the resonance capture. The key to evaluate the resonant part of this reaction rate is a detailed knowledge of properties such as the precise excitation energy, decay width, spin and parity of levels in the Gamow peak region.

In our experiment, the isobaric analog state and its neighbors in ^{23}Mg must play an important role in the radiative proton capture reaction ^{22}Na$(p,\gamma)^{23}$Mg in an astrophysical environment. The states above the proton binding energy in ^{23}Mg (S_p = 7580.3(14) keV [19]) become resonant in the capture process. With our more precise γ-ray energy determination and by using the proton binding energy above, we find the energy of the IAS resonance to be E_{res}(IAS) = 223(2) keV (energy in the center of the mass of the system). Unfortunately, we can not make a new determination of the strength for this resonance ($\omega\gamma$) from the presently available data without inferring values from calculations that involve unchecked assumptions. So the uncertainties must remain as large as in [27].

The 7787 keV state [E_{res} = 207(2) keV] is a key player in the ^{22}Na$(p,\gamma)^{23}$Mg reaction. We can now estimate its resonance strength based on the assumption that the proton peak observed by Tighe et al. [12] is predominantly due to the decay of this state. From this reference, we take the proton branching relative to higher energy proton peaks and then use the proton-to-γ–ray branching determined in Ref. [13], obtaining $\Gamma_p/\Gamma_\gamma = 0.08(2)$. From this result with our γ-ray branchings and the lifetime of the state, as recently measured in a GAMMASPHERE experiment [18], τ

= 10(3) fs, we derive the resonance strength as: $\omega\gamma = 2.6(9)$ meV. This value agrees with the one obtained from direct measurement, $\omega\gamma = 1.4(3)$ meV [15]. The latter experiment, however, was a difficult one involving a radioactive ^{22}Na target, and only the main γ–decay branch to the first excited state in ^{23}Mg was observed, an upper limit of 0.4 meV being set on each other possible γ-decay branches. The authors only included the single observed transition in their determination of $\omega\gamma$. Presumably to incorporate the possibility of other branches, the NACRE compilation [27] value, which was based on the same measurement, was $\omega\gamma = 1.8(7)$ meV, closer to what we find, and it was this value that was adopted in the nucleosynthesis calculation of Ref. [18].

Our newly determined strength for $E_{res} = 207$ keV shows it to be the resonance that contributes most to the reaction rate for the important temperature range for ONe novae, $T_9 = 0.1$-0.4. This value, though more reliable, is not significantly different from those used in the previous nucleosynthesis calculations, and it does not significantly change the reaction rates. The depletion of ^{22}Na via radiative proton capture, $^{22}\mathrm{Na}(p,\gamma)^{23}\mathrm{Mg}$, becomes about 40% larger and will further diminish the detectable distances for the 1.275 MeV γ line from ^{22}Na decay in space-based telescopes. The estimates of the maximum detectable distances depend not only on the reaction rates obtained from nuclear data, but also on the novae models adopted. It is beyond the scope of this dissertation to recalculate them. As our rates are slightly higher than those obtained in Ref. [18], we can only conclude that these new data will further reduce the detection distance below the limit of 0.6 kpc found in that work for the INTEGRAL spectrometer SPI. Clearly, the $^{22}\mathrm{Na}(p,\gamma)^{23}\mathrm{Mg}$ reaction is the major competition for the depletion of ^{22}Na.

CHAPTER VI

SUMMARY

We have measured for the first time the $\beta - \gamma$ coincidence for ^{23}Al and used them to establish the decay scheme, to determine for the first time the absolute branching ratios and logft values for the transitions to the final states in the daughter nucleus ^{23}Mg, including some with known spins and parities, to determine the half life, and to improve the mass of the ^{23}Al. We have unambiguously determined the spin and parity $J^{\pi} = 5/2^{+}$ for the ^{23}Al ground state.

First, a 48 MeV/A ^{24}Mg beam from the K500 cyclotron was used to bombard the hydrogen gas in the LN_2 cooled gas cell to produce the ^{23}Al radioactive beam via the ^{1}H(^{24}Mg,^{23}Al)2n reaction. With primary ^{24}Mg beam currents from the cyclotron of about 20 pnA, rates of about 4000 ^{23}Al nuclei per second with the energy of 40.3 MeV and ∼85% purity ^{23}Al were obtained at the focal plane of MARS. Aluminum degraders further purified the ^{23}Al samples to >99%.

Second, we have measured β and the γ–ray spectra in coincidence with β. Totally, twenty-five γ–ray peaks are identified as originating from the decay of ^{23}Al. With the well calibrated HPGe γ detector, we deduced the absolute intensities for the observed γ–rays and constructed a decay scheme that includes 16 β–decay branches to states in ^{23}Mg, including the ground state from those results. The ^{23}Al β–decay schemes are shown in Figs. 34 and 38. We also deduce the absolute branching ratios and logft values for the transitions to the final states in the daughter nucleus ^{23}Mg. The method was used before only in one case [90], and is for the first time used for a case with a complex decay scheme.

Third, the spin and parity for the ^{23}Al ground state was obtained based on the β–decay selection rules and the absolute logft values. This $5/2^{+}$ result is in agreement

with that of its mirror nucleus ^{23}Ne and contradicts the earlier suggestion of $J^{\pi} = 1/2^{+}$, which is based on the reaction cross section measurements [21] and relativistic mean field calculations [22, 23, 24]. Moreover, it also sheds serious doubt on the claim that ^{23}Al is a proton-halo nucleus. The large centrifugal barrier for a $d_{5/2}$ orbital and the already large Coulomb barrier should easily contain the wave function of the last proton inside the nuclear potential well, in spite of its low binding energy. This higher spin for the ^{23}Al ground state also has the consequence that the direct component of the reaction rate for the radiative proton capture on ^{22}Mg is not very large. It decreases the possibility of a simple explanation for the non-observation of the 1.275 MeV line from ^{22}Na decay in spectra taken by space-based γ–ray telescopes. There is no evidence that its precursor, ^{22}Mg, can be depleted in ONe novae explosions by the reaction $^{22}\mathrm{Mg}(p,\gamma)^{23}\mathrm{Al}$.

A RIKEN group [109] reported measuring the magnetic moment of ^{23}Al and finding its value to be consistent with the normal shell model prediction for $J^{\pi} = 5/2^{+}$. It should be noted that assignments of spin-parities from magnetic moments are model dependent, while those from β–decay systematics are considered definitive [110]. Fortunately, in this case, both methods give the same result. The question about the ground-state spin-parity of ^{23}Al is settled.

Fourth, the half life of ^{23}Al (447(4) ms) [96] was obtained from the $\beta - \gamma$ coincidence measurement. It is consistent with the previously accepted value of 470(30) ms [93], but it is more accurate. The method is the first time used here.

Fifth, we have also found two states in ^{23}Mg with small ft values at 7802.9(5) and 7787.2(6) keV and identified them to be the isobaric analog states of the ^{23}Al ground state from $\log ft = 3.305(23)$ and a $J^{\pi} = (7/2)^{+}$ state, which likely dominates the proton-decay spectrum. Both are resonances contributing to the depletion reaction, $^{22}\mathrm{Na}(p,\gamma)^{23}\mathrm{Mg}$. For the latter resonance at $E_{res} = 207(2)$ keV, we deduce, using

our results and results from four other experiments, find its resonance strength to be $\omega\gamma = 2.6(9)$ meV, making it the dominant contributor to the reaction rate at the temperatures of explosive H burning in ONe novae.

Sixth, the mass excess of ^{23}Al can be deduced from the Isobaric Multiplet Mass Equation [97, 98]. We get Q_{EC}=12223.8(28) keV. This leads to a small increase of the proton separation energy, S_p = 142(3) keV (It was 123 keV). Combined with the position of the ^{23}Al 1^{st} excited state from Reference [10], it gives a smaller resonance energy, E_{res} = 386(26) keV. This energy factor alone increases the resonance contribution on the ^{22}Mg$(p,\gamma)^{23}$Al reaction by an order of magnitude for $T_9 \simeq$ 0.3-0.5.

Seventh, the BGO Compton shield was for the first time used in-beam. It has been successfully working in the $\beta - \gamma$ coincidence measurement of ^{23}Al decay. As we expected before the experiment, the background at higher energy region of ^{23}Al $\beta - \gamma$ coincidence spectrum is significantly reduced.

Finally, to further improve our knowledge on the ^{22}Na$(p,\gamma)^{23}$Mg reaction rate, it is desirable to have a high-resolution remeasurement of the β–delayed proton decay of these ^{23}Mg states. This experiment has been successfully carried out recently (May 2007) at the Cyclotron Institute of the Texas A&M University using a new method where ^{23}Al was implanted in the middle of a thin silicon strip detector [111]. The beam was on for 1 second to do the implantation, and then the beam was turned off for 1 second and the β–delayed proton decay was measured with the thin silicon detector in coincidence with the β particles measured in a thick silicon detector placed behind for 1 second. The experimental data is under analysis.

The experimental study on the radioactive nucleus ^{23}Al was successful. The experimental setup and method could be used to study the nuclei, such as ^{27}P and ^{31}Cl, with similar properties and similar importance in explosive hydrogen burning in the stars.

REFERENCES

[1] C. Rolfs and W. Rodney, *Cauldrons in the Cosmos* (The University of Chicago Press, Chicago, Illinois, 1988).

[2] J. Jose, A. Coc, and M. Hernanz, Astrophys. J. **520**, 347 (1999).

[3] S. Starrfield, J. Truran, M. Wiescher, and W. Sparks, Mon. Not. R. Astron. Soc. **296**, 502 (1998).

[4] S. Wanajo, M. Hashimoto, and K. Homono, Astrophys. J. **523**, 409 (1999).

[5] A. F. Iyudin, K. Bennett, H. Bloemen, R. Diehl, W. Hermsen, G. G. Lichti, D. Morris, J. Ryan, V. Schonfelder, H. Steinle, A. Strong, M. Varendorff, and C. Winkler, Astron. Astrophys. **300**, 422 (1995).

[6] R. Diehl, Nucl. Phys. A **718**, 52c (2003).

[7] M. Arnould and W. Beelen, Astron. Astrophys. **33**, 215 (1974).

[8] M. Arnould and H. Norgaard, Astron. Astrophys. **64**, 195 (1978).

[9] M. Wiescher, J. Gorres, B. Sherrill, M. Mohar, J. S. Winfield, and B. A. Brown, Nucl. Phys. A **484**, 90 (1988).

[10] J. A. Caggiano, D. Bazin, W. Benenson, B. Davids, R. Ibbotson, H. Scheit, B. M. Sherrill, M. Steiner, J. Yurkon, A. F. Zeller, B. Blank, M. Chartier, J. Greene, J. A. Nolen, A. H. Wuosmaa, M. Bhattacharya, A. Garcia, and M. Wiescher, Phys. Rev. C **64**, 025802 (2001).

[11] R. A. Gough, R. G. Sextro, and J. Cerny, Phys. Rev. Lett. **28**, 510 (1972).

[12] R. J. Tighe, J. C. Batchelder, D. M. Moltz, T. J. Ognibene, M. W. Rowe, J. Cerny, and B. A. Brown, Phys. Rev. C **52**, R2298 (1995).

[13] K. Perajarvi, T. Siiskonen, A. Honkanen, P. Dendooven, A. Jokinen, P. O. Lipas, M. Oinonen, H. Penttila, and J. Aysto, Phys. Lett. B **492**, 1 (2000).

[14] S. Seuthe, C. Rolfs, U. Schroder, W. H. Schulte, E. Somorjai, H. P. Trautvetter, F. B. Waanders, R. W. Kavanaghh, H. Ravn, M. Arnould, and G. Paulus, Nucl. Phys. A **514**, 471 (1990).

[15] F. Stegmuller, C. Rolfs, S. Schmidt, W. H. Schulte, H. P. Trautvetter, and R. Kavanagh, Nucl. Phys. A **601**, 168 (1996).

[16] S. Schmidt, C. Rolfs, W. H. Schulte, H. P. Trautvetter, R. W. Kavanagh, C. Hategan, S. Faber, B. D. Valnion, , and G. Graw, Nucl. Phys. A **591**, 227 (1995).

[17] S. Kubono, T. Kajino, and S. Kato, Nucl. Phys. A **588**, 305c (1995).

[18] D. G. Jenkins, C. J. Lister, R. V. F. Janssens, T. L. Khoo, E. F. Moore, K. E. Rehm, B. Truett, A. H. Wuosmaa, M. Freer, B. R. Fulton, and J. Jose, Physical Review Letters **92**, 031101 (2004).

[19] G. Audi, A. H.Wapstra, and C. Thibault, Nucl. Phys. A **729**, 337 (2003).

[20] http://www.nndc.bnl.gov. National Nuclear Data Center, BNL. Accessed May 2007.

[21] X. Z. Cai, H. Y. Zhang, W. Q. Shen, Z. Z. Ren, J. Feng, D. Q. Fang, Z. Y. Zhu, W. Z. Jiang, Y. G. Ma, C. Zhong, W. L. Zhan, Z. Y. Guo, G. Q. Xiao, J. S. Wang, Y. T. Zhu, J. C. Wang, J. X. Li, M. Wang, J. F. Wang, Z. J. Ning, Q. J. Wang, and Z. Q. Chen, Phys. Rev. C **65**, 024610 (2002).

[22] Z. Hu-Yong, S. Wen-Qing, R. Zhong-Zhou, M. Yu-Gang, C. Xiang-Zhou, Z. Chen, W. Yi-Bin, and C. Jin-Gen, Chin. Phys. Lett. **19**, 1599 (2002).

[23] Z. Hu-Yong, S. Wen-Qing, R. Zhong-Zhou, M. Yu-Gang, C. Xiang-Zhou, Z. Chen, W. Yi-Bin, and C. Jin-Gen, Chin. Phys. Lett. **20**, 46 (2003).

[24] H. Y. Zhang, W. Q. Shen, Z. Z. Ren, Y. G. Ma, J. G. Chen, X. Z. Cai, C. Zhong, X. F. Zhou, Y. B. Wei, G. L. Ma, and K. Wang, Nucl. Phys. A **722**, 518c (2003).

[25] L. Trache, F. Carstoiu, C. A. Gagliardi, and R. E. Tribble, Eur. Phys. J. **A27, Suppl. 1**, 237 (2006).

[26] D. C. Black, Geochim. Cosmochim. Acta **36**, 347 (1972).

[27] C. Angulo, M. Arnould, M. Rayet, P. Descouvemont, D. Baye, C. Leclercq-Willain, A. Coc, S. Barhoumi, P. Aguer, C. Rolfs, R. Kunz, J. W. Hammer, A. Mayer, T. Paradellis, S. Kossionides, C. Chronidou, K. Spyrou, S. Degl'Innocenti, G. Fiorentini, B. Ricci, S. Zavatarelli, C. Providencia, H. Wolters, J. Soares, C. Grama, J. Rahighi, A. Shotter, and M. L. Rachti, Nucl. Phys. A **656**, 3 (1999).

[28] M. Wiescher, Nucl. Phys. A **751**, 285c (2005).

[29] A. Aprahamian, K. Langanke, and M. Wiescher, Prog. Part. Nucl. Phys. **54**, 535 (2005).

[30] H. A. Bethe and C. L. Critchfield, Phys. Rev. **54**, 248 and 862 (1938).

[31] The Sudbury Neutrino Observatory (SNO) publications and theses. http://www.sno.phy.queensu.ca/sno/publications.html. Accessed May 2007.

[32] H. A. Bethe, Phys. Rev. **55**, 103 and 434 (1939).

[33] C. F. V. Weizsacker, Phys. Z. **38**, 176 (1937).

[34] C. F. V. Weizsacker, Phys. Z. **39**, 633 (1938).

[35] W. P. Tan, private communications. Dept. of Physics, University of Notre Dame. May 2007.

[36] J. C. Wheeler, *Cosmic Catastrophes* (Cambridge University Press, Cambridge, United Kingdom, 2000).

[37] http://chandra.harvard.edu/photo/2005/sn87a/index.html. X-ray plot was obtained by NASA/CXC/PSU/S.Park & D.Burrows. Optical plot was obtained by NASA/STScI/CfA/P.Challis. Accessed May 2007.

[38] The picture was obtained from this website. http://cognitivedistortion.com/. Accessed May 2007.

[39] C. Rolfs, W. S. Rodney, M. H. Shapiro, and H. Winkler, Nucl. Phys. A **241**, 460 (1975).

[40] W. H. Hietzke, Ph.D. thesis, California State University, Los Angeles, California, 1975.

[41] H. L. Berg, W. H. Hietzke, C. Rolfs, and H. Winkler, Nucl. Phys. A **276**, 168 (1977).

[42] J. J. Smit, M. A. Meyer, J. P. L. Reinecke, and D. Reitmann, Nucl. Phys. A **318**, 111 (1979).

[43] J. Goerres, C. Rolfs, P. Schmalbrock, H. P. Trautvetter, and J. Keinonen, Nucl. Phys. A **385**, 57 (1982).

[44] J. Goerres, H. W. Becker, L. Buchmann, C. Rolfs, P. Schmalbrock, H. P. Trautvetter, and A. Vlieks, Nucl. Phys. A **408**, 372 (1983).

[45] J. Zyskind, M. Rios, and C. Rolfs, Astrophysical J. (Lett.) **243**, L53 (1981).

[46] D. D. Clayton and F. Hoyle, Astrophys. J. **187**, L101 (1974).

[47] M. Mukherjee, A. Kellerbauer, D. Beck, K. Blaum, G. Bollen, F. Carrel, P. Delahaye, J. Dilling, S. George, C. Guenaut, F. Herfurth, A. Herlert, H.-J. Kluge, U. Koster, D. Lunney, S. Schwarz, L. Schweikhard, and C. Yazidjian, Physical Review Letters **93**, 150801 (2004).

[48] T. D. Lee and C. N. Yang, Phys. Rev. **104**, 254 (1956).

[49] C. S. Wu, E. Ambler, R. W. Hayward, D. D. Hoppes, and R. P. Hudson, Phys. Rev. **105**, 1413 (1957).

[50] J. C. Hardy and I. S. Towner, Phys. Rev. Lett. **88**, 252501 (2002).

[51] J. C. Hardy, V. E. Iacob, M. Sanchez-Vega, R. G. Neilson, A. Azhari, C. A. Gagliardi, V. E. Mayes, X. Tang, L. Trache, and R. E. Tribble, Phys. Rev. Lett. **91**, 082501 (2003).

[52] J. C. Hardy and I. S. Towner, Phys. Rev. C **71**, 055501 (2005).

[53] X. Lu, *Nuclear Physics*, 2nd ed. (The Atomic Energy Press, Beijing, China, 2000).

[54] K. Heyde, *Basic Ideas and Concepts in Nuclear Physics* (The Institute of Physics Publishing, London, UK, 1994).

[55] Double beta decay. http://en.wikipedia.org/wiki/Double_beta_decay. Accessed May 2007.

[56] K. S. Krane, *Introductory Nuclear Physics* (John Wiley & Sons, Inc., New York, 1988).

[57] S. S. M. Wong, *Introductory Nuclear Physics* (John Wiley & Sons, Inc., New York, 1998).

[58] R. E. Tribble, R. H. Burch, and C. A. Gagliardi, Nucl. Instr. and Meth. A **285**, 441 (1989).

[59] R. E. Tribble, C. A. Gagliardi, and W. Liu, Nucl. Instr. and Meth. B **56/57**, 956 (1991).

[60] R. E. Tribble, A. Azhari, C. A. Gagliardi, J. C. Hardy, A. Mukhamedzhanov, X. Tang, L. Trache, and S. J. Yennello, Nucl. Phys. A **701**, 278c (2002).

[61] A. Azhari, V. Burjan, F. Carstoiu, C. A. Gagliardi, V. Kroha, A. M. Mukhamedzhanov, F. M. Nunes, X. Tang, L. Trache, and R. E. Tribble, Phys. Rev. C **63**, 055803 (2001).

[62] J. F. Brinkley, , A. Azhari, B. Olsen, X. Tang, L. Trache, and R. E. Tribble, in *The Progress in Research 2002-2003*, edited by Y. W. Lui and R. E. Tribble (Cyclotron Institute, Texas A&M University, College Station, Texas, 2003), pp. V–9.

[63] http://dnr080.jinr.ru/lise/lise.html. The program LISE++ is used to calculate the transmission and yields of fragments produced and collected in a spectrometer. Accessed May 2005.

[64] V. E. Iacob and J. C. Hardy, in *The Progress in Research 1999-2000*, edited by Y. W. Lui and J. B. Natowitz (Cyclotron Institute, Texas A&M University, College Station, Texas, 2000), p. Section 5.

[65] G. F. Knoll, *Radiation Detection and Measurement*, 3rd ed. (John Wiley & Sons, Inc., New York, NY, USA, 2000).

[66] J. C. Hardy, V. E. Iacob, M. Sanchez-Vega, R. T. Effinger, P. Lipnik, V. E. Mayes, D. K. Willis, and R. G. Helmer, Int. J. Appl. Radiat. Isotop. **56**, 65 (2002).

[67] R. G. Helmer, J. C. Hardy, V. E. Iacob, M. Sanchez-Vega, R. G. Neilson, and J. Nelson, Nucl. Instr. and Meth. A **511**, 360 (2003).

[68] R. G. Helmer, N. Nica, , J. C. Hardy, and V. E. Iacob, Int. J. Appl. Radiat. Isotop. **60**, 173 (2004).

[69] Y. Zhao, W. Zhan, and Z. Guo, Nucl. Instr. and Meth. A **355**, 464 (1995).

[70] M. L. Muga, D. J. Burnsed, W. E. Steeger, and H. E. Taylor, Nucl. Instr. and Meth. **83**, 135 (1970).

[71] M. L. Muga, Nucl. Instr. and Meth. **95**, 349 (1971).

[72] M. L. Muga and G. Griffith, Nucl. Instr. and Meth. **109**, 289 (1973).

[73] L. Trache, private communications. Cyclotron Institute, Texas A&M University. May 2006.

[74] I.-Y. LEE, Nucl. Phys. A **520**, 641 (1990).

[75] V. E. Iacob, R. Burch, J. C. Hardy, P. Lipnik, and L. Trache, in *The 11th IEEE NPSS Real Time Conference Proceedings*, edited by S. C. Schaller (The IEEE and The IEEE Nuclear and Plasma Science Society, Santa Fe, New Mexico, 1999), p. 153.

[76] D. C. Radford, Nucl. Instr. and Meth. A **361**, 306 (1995).

[77] http://radware.phy.ornl.gov/rw/frames/. RadWare is a software package for interactive graphical analysis of gamma-ray coincidence data. It can be download from its homepage. Accessed May 2005.

[78] J. C. Hardy, N. Nica, V.E. Iacob and L. Trache, private communications. Cyclotron Institute, Texas A&M University. September 2006.

[79] C. Detraz, Nucl. Phys. A **188**, 513 (1972).

[80] J. Honkanen, M. Kortelahti, J. Aysto, K. Eskola, and A. Hautojarvi, Physica Scripta. **19**, 239 (1979).

[81] E. K. Warburton, C. J. Lister, D. E. Alburger, and J. W. Olness, Phys. Rev. C **23**, 1242 (1981).

[82] E. G. Adelberger, P. B. Fernandez, C. A. Gossett, J. L. Osborne, and V. J. Zeps, Phys. Rev. Lett. **55**, 2129 (1985).

[83] E. Schonfeld, H. Janssen, R. Klein, J. C. Hardy, V. E. Iacob, M. Sanchez-Vega, H. C. Griffin, and M. A. Luddington, Int. J. Appl. Radiat. Isotop. **56**, 215 (2002).

[84] M. Blaauw and S. J. Gelsema, Nucl. Instr. and Meth. A **422**, 417 (1999).

[85] M. Blaauw, Nucl. Instr. and Meth. A **332**, 493 (1993).

[86] T. M. Semkow, G. Mehmood, P. P. Parekh, and M. Virgil, Nucl. Instr. and Meth. A **290**, 437 (1990).

[87] M. Blaauw and S. J. Gelsema, Nucl. Instr. and Meth. A **505**, 311 (2003).

[88] P. D. Felice, P. Angelini, A. Fazio, and R. Biagini, Applied Radiation and Isotopes. **52**, 745 (2000).

[89] S. J. Gelsema, Ph.D. thesis, Delft University of Technology, Mekelweg 15, 2629 JB Delft, The Netherlands, 2001.

[90] V. E. Iacob, J. C. Hardy, C. A. Gagliardi, J. Goodwin, N. Nica, H. I. Park, G. Tabacaru, L. Trache, R. E. Tribble, Y. Zhai, and I. S. Towner, Physical Review C (Nuclear Physics) **74**, 015501 (2006).

[91] J. C. Hardy, L. C. Carraz, B. Jonson, , and P. G. Hansen, Phys. Lett. B **71**, 307 (1977).

[92] J. C. Hardy and I. S. Towner, Phys. Rev. Lett. **88**, 252501 (2002).

[93] P. M. Endt, Nucl. Phys. A **521**, 1 (1990).

[94] V. E. Iacob, J. C. Hardy, C. A. Gagliardi, V. E. Mayes, N. Nica, G. Tabacaru, L. Trache, and R. E. Tribble, in *The Progress in Research 2005-2006*, edited by Y. W. Lui and R. E. Tribble (Cyclotron Institute, Texas A&M University, College Station, Texas, 2006), pp. I–31.

[95] V. E. Iacob, Y. Zhai, T. Al-Abdullah, C. Fu, J. C. Hardy, N. Nica, H. I. Park, G. Tabacaru, L. Trache, and R. E. Tribble, in *The Progress in Research 2005-2006*, edited by Y. W. Lui and R. E. Tribble (Cyclotron Institute, Texas A&M University, College Station, Texas, 2006), pp. I–11.

[96] Y. Zhai, V. E. Iacob, L. Trache, J. C. Hardy, N. Nica, C. Fu, T. Al-Abdullah, H. I. Park, G. Tabacaru, and R. E. Tribble, Phys. Rev. C **to be submitted**, (2007).

[97] in *The Proceedings of the Robert A. Welch Conferences on Chemical Research* (Robert Welch Foundation, Houston, Texas, USA, 1957), Vol. 1.

[98] S. Weinberg and S. B. Treiman, Phys. Rev. **116**, 465 (1958).

[99] http://www.nndc.bnl.gov/logft/. National Nuclear Data Center, logft β-decay calculator. Accessed May 2007.

[100] V. E. Iacob, Y. Zhai, T. Al-Abdullah, C. Fu, J. C. Hardy, N. Nica, H. I. Park, G. Tabacaru, L. Trache, and R. E. Tribble, Physical Review C (Nuclear Physics) **74**, 045810 (2006).

[101] M. Hernanz, in *In Classical Nova Explosions*, edited by M. Hernanz and J. Jose (AIP, New York, USA, 2002).

[102] M. Leventhal, C. MacCallum, and A. Watts, Astrophys. J. **216**, 491 (1977).

[103] M. D. Leising, Astron. Astrophys. Suppl. Ser. **97**, 299 (1993).

[104] M. Wiescher, J. Gorres, F.-K. Thielemann, and H. Ritter, Astron. Astrophys. **160**, 56 (1986).

[105] T. Gomi, T. Motobayashi, K. Yoneda, S. Kanno, N. Aoi, Y. Ando, H. Baba, K. Demichi, Z. Fulop, U. Futakami, H. Hasegawa, Y. Higurashi, K. Ieki, N. Imai, N. Iwasa, H. Iwasaki, T. Kubo, S. Kubono, M. Kunibu, Y. U. Matsuyama, S. Michimasa, T. Minemura, H. Murakami, T. Nakamura, A. Saito, H. Sakurai, M. Serata, S. Shimoura, T. Sugimoto, E. Takeshita, S. Takeuchi, K. Ue, K. Yamada, Y. Yanagisawa, A. Yoshida, and M. Ishihara, Nucl. Phys. A **718**, 508c (2003).

[106] T. Gomi, T. Motobayashi, Y. Ando, N. Aoi, H. Baba, K. Demichi, Z. Elekes, N. Fukuda, Z. Fulop, U. Futakami, H. Hasegawa, Y. Higurashi, K. Ieki, N.

Imai, M. Ishihara, K. Ishikawa, N. Iwasa, H. Iwasaki, S. Kanno, Y. Kondo, T. Kubo, S. Kubono, M. Kunibu, K. Kurita, Y. U. Matsuyama, S. Michimasa, T. Minemura, M. Miura, H. Murakami, T. Nakamura, M. Notani, S. Ota, A. Saito, H. Sakurai, M. Serata, S. Shimoura, T. Sugimoto, E. Takeshita, S. Takeuchi, Y. Togano, K. Ue, K. Yamada, Y. Yanagisawa, K. Yoneda, and A. Yoshida, Nucl. Phys. A **734**, Suppl. 1, E77 (2004).

[107] T. Gomi, T. Motobayashi, Y. Ando, N. Aoi, H. Baba, K. Demichi, Z. Elekes, N. Fukuda, Z. Fulop, U. Futakami, H. Hasegawa, Y. Higurashi, K. Ieki, N. Imai, M. Ishihara, K. Ishikawa, N. Iwasa, H. Iwasaki, S. Kanno, Y. Kondo, T. Kubo, S. Kubono, M. Kunibu, K. Kurita, Y. Matsuyama, S. Michimasa, T. Minemura, M. Miura, H. Murakami, T. Nakamura, M. Notani, S. Ota, A. Saito, H. Sakurai, M. Serata, S. Shimoura, T. Sugimoto, E. Takeshita, S. Takeuchi, Y. Togano, K. Ue, K. Yamada, Y. Yanagisawa, and K. Yoneda, Nucl. Phys. A **758**, 761c (2005).

[108] S. Kubono, C. C. Yun, R. N. Boyd, L. R. Buchmann, Y. Fuchi, M. Hosaka, N. Ikeda, C. L. Jiang, I. Katayama, H. Kawashima, H. Miyatake, T. Niizeki, T. Nomura, A. Odahara, M. Ohura, H. Ohnuma, H. Orihara, C. Rolfs, T. Shimoda, Y. Tajima, M. H. Tanaka, and H. Toyokawa, Z. Phys. **348**, 59 (1994).

[109] A. Ozawa, K. Matsuta, T. Nagatomo, M. Mihara, K. Yamada, T. Yamaguchi, T. Ohtsubo, S. Momota, T. Izumikawa, T. Sumikama, Y. Nakashima, H. Fujiwara, S. Kumashiro, R. Matsumiya, M. Ota, D. Shinojima, H. Tanaka, T. Yasuno, S. Nakajima, T. Suzuki, K. Yoshida, K. Muranaka, T. Maemura, A. Chiba, Y. Utsuno, M. Fukuda, K. Tanaka, I. Tanihata, Y. Nojiri, T. Minamisono, J. R. Alonso, G. F. Krebs, and T. J. M. Symons, Physical Review C (Nuclear Physics) **74**, 021301 (2006).

[110] http://www.nndc.bnl.gov/nds/NDSPolicies.pdf. Nuclear Data Sheets, General Policies, each issue and pp. iv-ix. Accessed May 2007.

[111] L. Trache, T. Al-Abdullah, A. Banu, C. Fu, V. Golovko, J. Hardy, V. Iacob, H. Park, G. Tabacaru, R. Tribble, Y. Zhai, J. Aysto, A. Saastamoinen, M. A. Bentley, D. Jenkins, T. Davinson, , and P. J. Woods, in *The Progress in Research 2006-2007*, edited by Y. W. Lui and R. E. Tribble (Cyclotron Institute, Texas A&M University, College Station, Texas, 2007), pp. I–29.

VITA

Yongjun Zhai obtained his B.S. degree in Physics and M.S. degree (graduated summa cum laude) in Nuclear Physics from Peking University, Beijing, P.R. China in 1998. He also obtained a M.S. degree in Applied Physics(Synchrotron Radiation Physics) from the Louisiana State University, Baton Rouge, Louisiana in 2002. Then he joined the Cyclotron Institute and the Physics Department of Texas A&M University (TAMU), College Station, Texas as a Ph.D. candidate in 2002. He was awarded the Robert A. Welch Foundation Graduate Assistant Research fellowship to do research in the Cyclotron Institute at TAMU(2002-2007). He obtained his Ph.D. in Nuclear Physics in 2007. He can be reached at Robert Tribble c/o Yongjun Zhai, Cyclotron Institute, Texas A&M University, College Station, Texas 77843.